Fakultät für Medizin

II. Medizinische Klinik und Poliklinik

PET/CT imaging to monitor safety and efficacy of oncolytic VSV therapy

Kim Agnes Bentrup

Vollständiger Abdruck der von der Fakultät für Medizin der Technischen Universität München zur Erlangung des akademischen Grades eines

Doctor of Philosophy (Ph.D.)

genehmigten Dissertation.

Vorsitzender: Univ.-Prof. Dr. Dr. St. Engelhardt

Betreuer der Dissertation: Priv.-Doz. Dr. O. Ebert

Prüfer der Dissertation:

1. apl. Prof. Dr. S. Ziegler

2. Priv.-Doz. Dr. P. S. Holm

Die Dissertation wurde am 17.12.2013 bei der Fakultät für Medizin der Technischen Universität München eingereicht und durch die Fakultät für Medizin am 08.05.2014 angenommen.

TABLE OF CONTENTS

INDEX OF FIGURES

INDEX OF TABLES

ABBREVIATIONS

°C	centigrade
^{124}I	iodine-124 isotope
^{125}I	iodine-125 isotope
^{18}F	fluor-18 isotope
^{18}F-FET	O-(2-[18F]fluoroethyl)-l-tyrosine
^{18}F-FHBG	(9-(4-[18F]-fluoro-3-[hydroxymethyl]butyl)guanine
Ab	antibody
abs.	absolute (100%)
Amp	Ampicillin
APS	ammonium persulphate
ATCC	American Type Culture Collection
BHK-21	baby hamster kidney cell line
bp	base pair
Bq	Becquerel
BSA	bovine serum albumin
CNS	central nervous system
CPE	cytopathic effect
CPE	cytopathic effect
CT	Computed Tomography
D-MEM	Dulbecco´s Modified Eagle´s Medium
DAPI	4',6-diamidino-2-phenylindole
ddH_2O	double distilled water
DMSO	dimethyl-sulfoxide
DNA	dexoyribonucleic acid
ds	double stranded
E. coli	*Escherichia coli*
EDTA	ethylenediaminetetraacetic acid
FCS	fetal calf serum

FDG	fluorodeoxyglucose
FLT	fluorothymidine
fwd	forward
G	glycoprotein
G-MEM	Glasgow Minimal Essential Medium
GFP	green fluorescent protein
h	hour(s)
HCC	hepatocellular carcinoma
HCV	hepatitis C virus
HE	hematoxylin and eosin stain
HIER	heat-induced epitope retrieval
HRP	horseradish peroxidase
HSV1	herpes simplex virus-1
i.p.	intraperitoneal
i.v	intravenious
IFN	interferon
Kb	kilobase
KBq	Kilobecquerel
$KClO_4$	potassium perchlorade
kDa	kilodalton
L	large polymerase protein
LB	*Luria Bertani*
M	molar
M	matrix protein
MBq	Megabecquerel
MeOH	Methanol
mg	milligram
min	minute(s)
mL	Milliliter
mm	millimeter
mM	millimolar
MOI	multiplicity of infection
MRI	magnet resonance imaging

mRNA	messenger RNA
MRI	magnet resonance imaging
MRT	magnet resonance tomography
MW	molecular weight
N	normal
N	nucleoprotein
NaOH	sodium hydroxide solution
NDV	Newcastle disease virus
NH_4Cl	ammonium chloride
NIS	sodium iodide symporter
nt	nucleotide
OD	optical density
OV	oncolytiv virus
P	phosphoprotein
p.i.	post infection
PBS	phosphate buffered saline
PBS-T	PBS Tween-20
PCR	polymerase chain reaction
PET	positron emission tomography
pfu	plaque forming units
PI	propidium iodide
pM	picomolar
rev	reverse
RNA	ribonucleic acid
rNIS	rat NIS
rpm	revolutions per minute
RT	room temperature
RT-PCR	reverse transcriptase PCR
rVSV	recombinant VSV
s	second(s)
SD	standard deviation
SDS	sodium dodecyl sulphate
SDS-PAGE	sodiumdodecyl polyacrylamide gel electrophoresis

SEM	standard error of the mean
SPECT	single-photon emission computed tomography
sr39tk	semi-random39 thymidine kinase (mutant version of tk)
ss	single stranded
sub	below
TAE	tris-acetate-EDTA
$TCID_{50}$	tissue culture infective dose 50
TE	TRIS-EDTA
TEMED	N,N,N',N'-Tetramethylethylenediamine
tk	thymidine kinase
U	unit(s)
UV	ultraviolet
v/v	volume per volume
VSV	vesicular stomatitis virus
w/o	without
w/v	weight per volume
wt	wild-type
α	anti
µg	microgram
µM	micromolar

1 INTRODUCTION

1.1 Hepatocellular Carcinoma

Hepatocellular carcinoma (HCC) is the most common primary liver cancer and the third leading cause of cancer-related death worldwide [1-3]. For 2008, 748,000 new cases and 695,000 deaths due to this malignancy were estimated [4]. Most of the cases occur in developing countries (approximately 85%), due to a high distribution of chronic hepatitis B virus (HBV) and hepatitis C virus (HCV) infections in these areas, which are major risk factors for HCC [5, 6]. Nevertheless, HCC is a globally spread malignant disease, showing rising incidence also in the USA, tripling between 1975 and 2005 [7].

A reason for the high mortality rate is that curative treatments are limited to liver resection or liver transplantation. Additionally, only a very low percentage of the patients are eligible for these treatments, based on the stage of the disease and the lesions inside the liver upon diagnosis [8]. Unfortunately, the small group of patients which receives these treatments shows a high rate of recurrence with 70% to 80% at five years [9-11].

Most patients are diagnosed with HCC at an advanced and therefore unresectable stage at the time of detection and, consequently, are only eligible for palliative management. The two main treatment options for these patients are transarterial chemoembolization (TACE) [12] or multikinase inhibitor Sorafenib treatment, which is to date the only approved systemic therapy for HCC [13, 14]. Nevertheless, patients with advanced disease still have to face a poor prognosis since the responses to these established therapies are usually

very minimal [13, 15, 16].

Therefore, HCC remains a major health problem and novel treatment options, especially for patients at advanced stages, are urgently needed.

1.2 Oncolytic virotherapy

1.2.1 Oncolytic viruses as cancer therapeutics

Oncolytic viruses (OV) have the ability to selectively propagate in cancerous cells, causing extensive damage to them, while healthy cells remain mainly unaffected as schematically depicted in Figure 1.

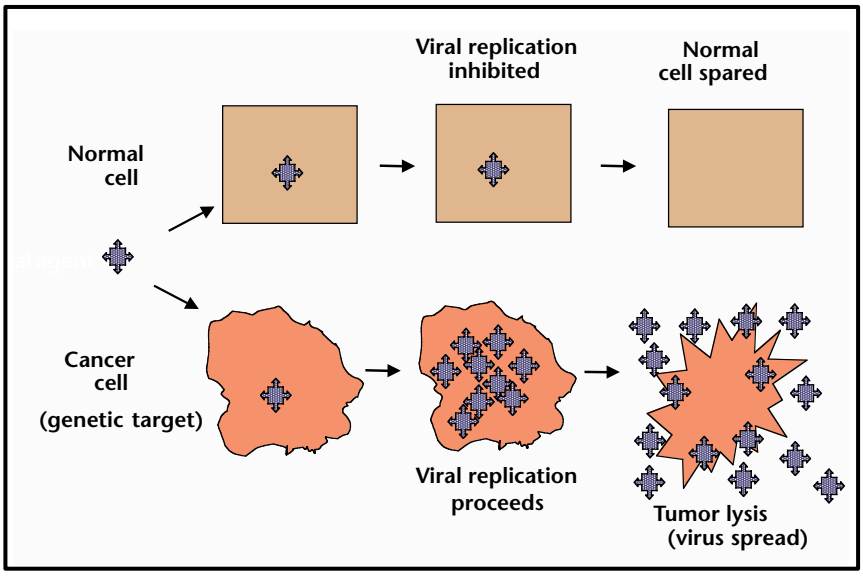

Figure 1. Principle of oncolysis through tumor-selective replication (from [17]).

Comparison of the fate of normal (rectangular) and cancerous cells upon OV infection. Soon after infection the virus starts to replicate in tumor cells and cause lysis, while this process is inhibited in healthy cells.

The group of oncolytic viruses comprises several viral families. Their oncophilic behaviour is mostly based on defects in the anti-viral defense of cancerous cells, which accumulate through changes in cellular biology during the

transformation from the normal into the malignant cell status [17]. This phenomenom explains, why different viruses exhibit different tumor selectivities; or expressed more accurately, why different tumors have varying susceptibilities to different OV therapies. However, this only partially explains the tumor specificity of OVs. The resistence of healthy versus cancerous cells against OV destruction has various reasons and underlying mechanisms, which have are not fully elucidated yet. Regardless of the mechanism, the fundamental differences between healthy and transformed cells can be exploited for targeting of OVs to tumor cells, as in Figure 2 [18, 19].

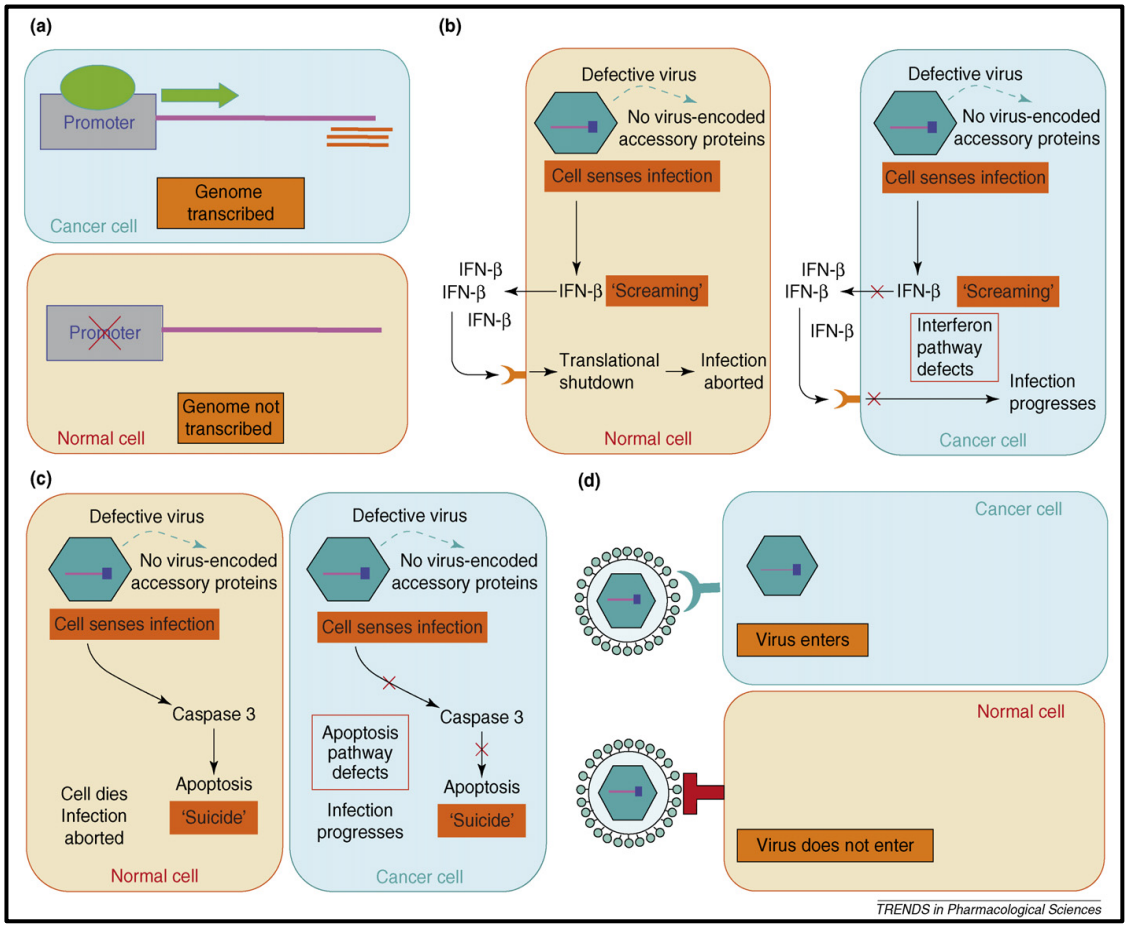

Figure 2. Different mechanisms for tumor selectivity by OVs (from [19]).

(a) Transcriptional targeting by placing essential viral genes under the control of tumor-specific promoters. (b) Translational targeting via interferon (IFN) release by healthy cells. IFN interferes with viral replication which inhibits the production of virus progeny. This defense mechanism is impaired in cancerous cells, which therefore permit progeny production. (c) Pro-apoptotic

targeting by translation of pro-apoptotic proteins through viral replication. Tumor cells are not susceptible to this signalling and do survive long enough for hosting viral progeny generation. (d) Transductional targeting through cell surface receptors, which enable viral entry and are exclusively or more abundantly expressed on transformed cells than on normal cells.

The history of OVs is a very long one, since the first beneficial effects on tumor sizes of cancer patients with viral infections have been reported from the middle of the 19th century [20-23]. Nevertheless, it took almost another 100 years, until the 1950's, for OVs to be considered as cancer therapeutics. During the past 15 years, OVs have been increasingly the focus of anti-cancer research, as the annual numbers of publications clearly indicate as shown in Figure 3 [24, 25].

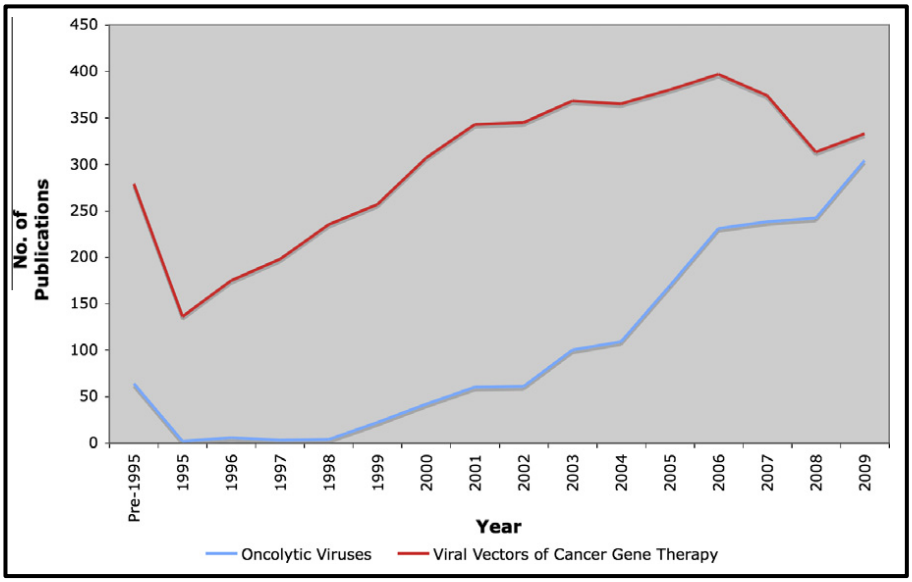

Figure 3. Number of publications in the field

Annual publications in the field of oncolytic virotheraphy (blue) and viral vectors of cancer gene therapy (red). "Pre-1995" indicates total number of publications in this area before 1995 (from [24]).

Being in the focus of research all over the world, oncolytic virotherapy has undergone several stages of development as illustrated in Figure 4. The first strategies of improvement aimed at the specificity and the oncolytic effect of the

viral vectors itself by manipulation of the genomes. Early attempts in the 90's were based on transcriptional and translational targeting [26-28]. After some years new ideas entered this field of research, and improvements in specificity were achieved by transductional targeting, microRNA targeting or gene shuffling [29-31].

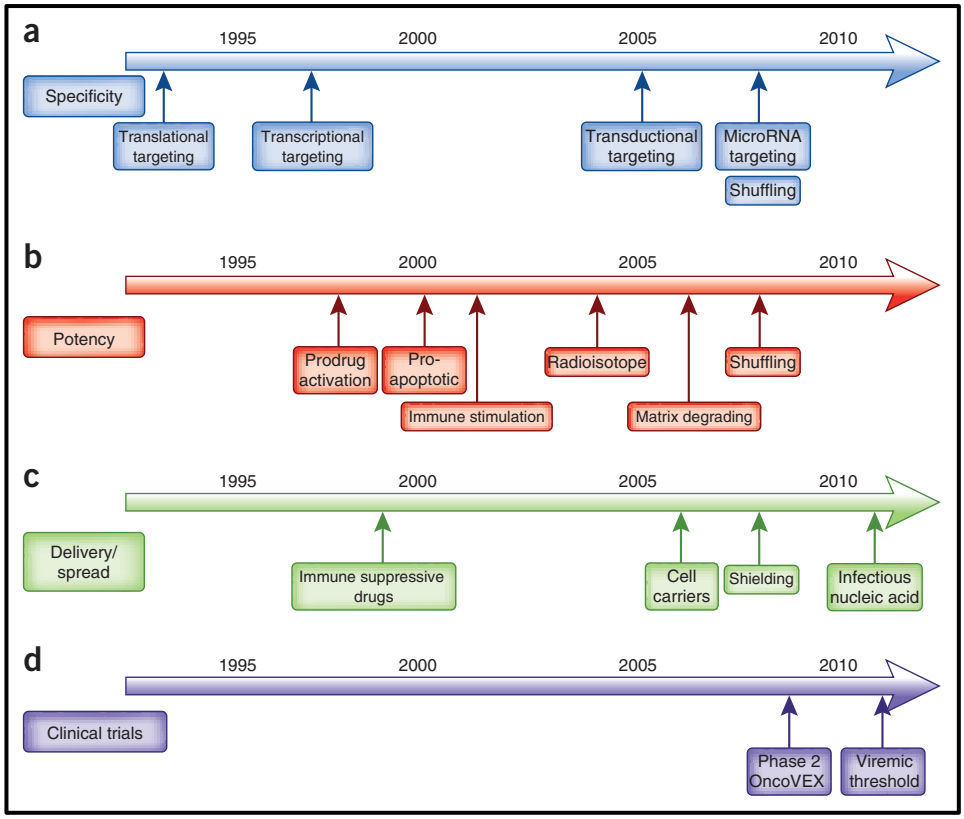

Figure 4. Timeline of brakethroughs in oncolytic virotherapy (from [32]).

Shown is the development of oncolytic virotherapy from 1990 to 2011. Research areas are divided into vector specificity (a), oncolytic potency (b), delivery and spread of the viruses (c) and clinical trials in the field (d).

Another area of research on OVs has been the enhancement of the OV potency. This has been accomplished primarily via combination therapies and prodrug activation [33], introduction of pro-apoptotic genes [34], immune stimulation [35], combination with radiotherapy [36] or the use of matrix-degrading proteins [37].

A third major area in the field of OV development involves the improvement in

the delivery and the viral spread after application. In this respect, significant breakthroughs have been achieved through the application of immune suppressive drugs [38]. In recent years, the focus has evolved into two main branches of viral delivery by shielding, either performed by loading viruses on carrier cells [39] or by polymer-shielding [40].

However, the intelligent design of various and diverse strategies over the years has succeeded in the establishment of very specific OV therapeutics for different cancers. Consequently, all these improvements in oncolytic virotherapy have helped to successfully introduce OVs into the clinic. The first clinical trials with OVs were done only at the beginning of this century, but the numbers soon increased significantly, so that to date, almost every family of the OV group has already been or is currently on its way to be tested in patients [32, 41-44].
Even though most prejudices concerning OVs and concerns about safety and feasibility have been ruled out, there is still a long way to go and the full potential of OV therapy has yet to be realized.

1.2.2 Vesicular Stomatitis Viruses

A very promising representative in the group of OVs is the vesicular stomatitis virus (VSV). VSV is a member of the *Mononegavirales* order and the *Rhabdoviridae* family. The enveloped virus has a bullet shaped structure. Two major VSV serotypes are endemic in most of Central and South America: VSV Indiana (VSV_{IN}) and VSV New Jersey (VSV_{NJ}). VSV is an arthropod-borne animal-virus and has several natural hosts, which include cattle, horses, pigs and a range of other mammals. There is almost no pre-existing immunity in

humans, which provides the first benefit of VSV as a therapeutic. In general, VSV infections in humans are mostly asymptomatic or show transient mild flu-like characteristics [45].

The VSV genome consists of 11 kb negative-sense, single-stranded RNA and encodes for five distinct proteins as schematically depicted in Figure 5.

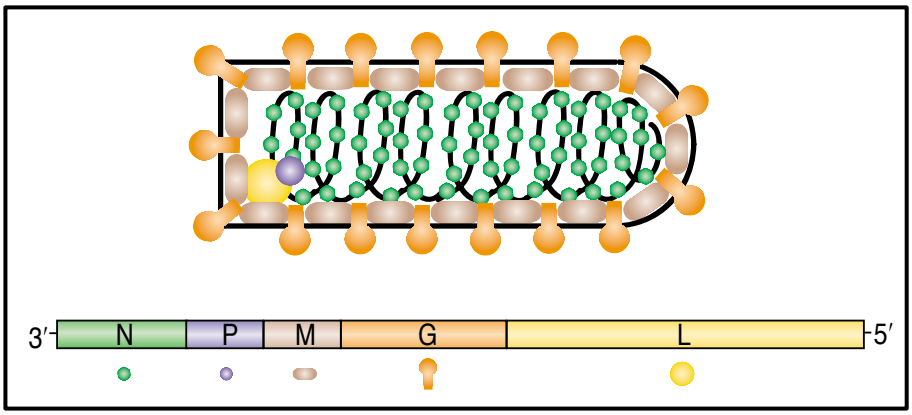

Figure 5. Schematic structure of the vesicular stomatitis virus (VSV) particle and genome (from [46]).

The VSV genome consists of five genes encoding for five proteins: the nucleoprotein (N), the phosphoprotein (P), the matrix protein (M), the glycoprotein (G) and the large polymerase protein (P). These proteins are assembled into the bullet shaped VSV virion.

Viral mRNA transcription decreases from the 3´ to the 5´ end due to the high fall-off rate of the viral polymerase. This causes decreasing expression levels of subsequent genes: N>P>M>G>L [47]. Nevertheless, the replication of VSV is very rapid and efficient, and assembly of progeny virions occurs 2 – 3 h after infection [48, 49].

VSV mRNA translation is accomplished by the host machinery and depends on robust mRNA translation [50]. VSV-infected cells preferentially translate the viral mRNA over the host mRNA, though the mechanism underlying this fact is not fully understood so far [45, 51].

The envelope of the VSV virion is made up of the matrix protein, creating a phospholipid bilayer, which is interspersed with the glycoprotein, responsible for receptor binding and cell entry of the virus [52]. The LDL receptor family was only recently identified as the cell-surface receptor VSV binds to in the process of cell entry. This explains the broad range of infectivity of VSV virions, since this receptor family shows an almost ubiquitous expression [53].

Usually, the cellular response to VSV infection involves the induction of type I interferon (IFN) expression [54, 55], which, subsequently, causes an upregulation of IFN-stimulated genes (ISGs). Several representatives of the ISGs have been reported to inhibit VSV replication directly [56-61]. These mechanisms largely explain the oncotropism of VSV, since transformed cells often have various defects in the type I IFN response [62-67], allowing VSV to use their cell machinery without any limitation.

Despite all of these convincing natural properties, VSV also shows one severe disadvantage: its neurotropism. As a member of the *Rhabdoviridae* family VSV has the ability to cross the blood brain barrier and wt VSV has been shown to infect the central nervous system (CNS) followed by encephalitis [51]. Hence, extensive research has been done in order to improve the VSV vector with the aim of enhancing its favorable oncotropism, while, simultaneously, reducing its undesirable neurotropism to guarantee safety of VSV treatment without attenuating its oncolytic potency [68, 69].

In conclusion, even though many of VSV's properties have been improved, there are still challenges remaining and hurdles, which need to be overcome. Nevertheless, VSV has been demonstrated as a highly effective therapeutic against various kinds of cancer, showing high future clinical potential [32, 45, 46, 62, 70-72].

1.2.3 VSV for HCC treatment

The efficacy of VSV for the treatment of HCC was reported first in 2003 by Ebert et al. [73]. In this very first study, rVSV-GFP was used to demonstrate a significant survival benefit in HCC-bearing rats compared to buffer treated ones as shown in Figure 6.

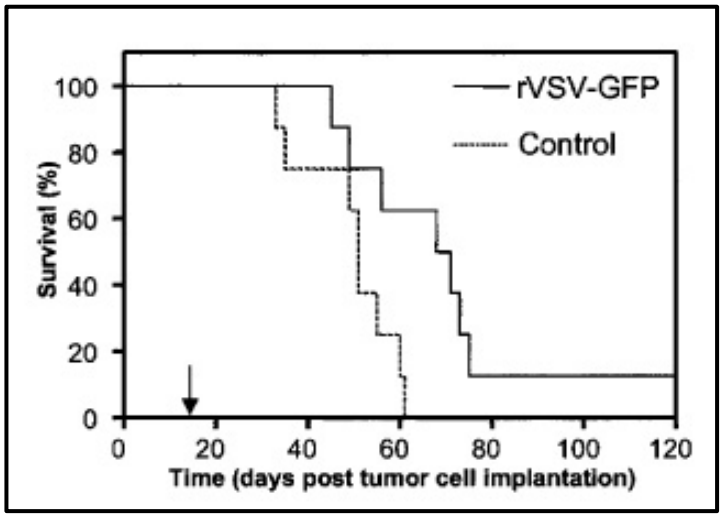

Figure 6. Survival of HCC-bearing rats after rVSV-GFP or control treatment

Kaplan-Meier curve of unifocal tumor-bearing rats after intratumoral injection of either 1 x 10^8 rVSV-GFP (n=8) or buffer control (n=8). Arrow indicates time of treatment (i.e. day 14) after tumor implantation.

In the next step, the VSV therapy was applied to rats bearing multifocal HCC lesions, as this mimics the clinical situation much better. Additionally, the intratumoral injection was replaced by arterial infusion of the virus directly into the hepatic artery (see methods chapter 3.2.8.4). This was done based on the knowledge that in humans HCC tumors in the liver are predominantly fed by arterial blood [74, 75]. The results of this study also demonstrated significant survival benefits of rVSV-GFP-treated versus control treated rats [76]. In the following years, different strategies to enhance the potency of the VSV

treatment in HCC were successfully applied: a fusogenic VSV was established [77], repeated VSV infusions were tested [78], a combination therapy with transarterial embolization (TAE) was introduced [79], and also immune-suppressive VSV vectors showed strong enhancements in therapeutic effects [80, 81]. Additionally, just recently the safety of VSV treatment of HCC with underlying fibrosis was proven, which has an additional strong impact on the applicability of VSV as an HCC therapeutic, since most patients present themselves in this status [82].

As a result, all the convincing data culminated in a phase I clinical trial at the Mayo Clinic (NCT01628640), which was initiated in 2012 and uses VSV expressing interferon-beta in liver cancer patients. These had been shown to have increased safety with greatly diminished neurotoxicity in Buffalo rats in comparison to non-interferon-beta expressing vectors [83].

Taken together, VSV is a highly promising novel candidate for HCC treatment and its development will be an exciting journey to follow.

1.3 Molecular *in vivo* imaging

Molecular *in vivo* imaging has emerged as an essential tool for the management of patients in the clinic. The great advantage of this technique is the possibility to monitor processes inside the body on a cellular basis and, therefore, to receive diagnostically valuable information without applying invasive procedures, like biopsies, to the patient.

By molecular imaging, specific targets can be addressed and analysed. Usually, a relevant molecule (“biomarker”) is identified at the beginning, which is then

either directly transformed into a probe or, alternatively, a probe is designed for the indirect tracking of this marker. The probe can be of almost any kind. It could, for example, be a metabolic molecule for which the uptake correlates with the function of the target of interest. It could also be a substrate, which is metabolized by the enzyme of interest. Furthermore, it is also possible to make use of an antibody, which binds to a receptor that is over-expressed on the cell type of interest.

These various possible probes need to be equipped with a suitable tracer, depending on the imaging modality of choice. Modalities for molecular imaging have expanded substantially over the last few years. However, for this study the focus was put on the combined imaging of positron emission tomography (PET) and computed tomography (CT), which are broadly available and well established methods in the clinic. By the simultaneous application of a morphological (CT) with a functional (PET) imaging modality, the physician can benefit from the detailed anatomic information offered by CT, while biological processes are detected by PET. An overlay of the two signals produces a hybrid image, enabling the acquisition of highly detailed information regarding internal processes and their precise location.

With the possibilities offered by molecular imaging, another keyword increasingly important in medicine: personalized therapy. Personalized therapy aims to select treatments for every patient individually. The idea behind personalized therapy is to overcome the limits of conventional therapies, which usually follow a strict treatment pattern, which often does not match the diversity of patients. It is highly desirable to be able to make better therapy selections based on better predictions of success of potential therapies and, additionally,

to report responses to an applied therapy as early as possible. Therefore, it is also hoped that molecular imaging will allow us to monitor therapeutic responses at a molecular level to better understand the mechanisms behind success and failure, and, consequently, optimize treatments for every patient in a personalized manner [84].

1.3.1 Reporter gene imaging by PET

Another subfield of molecular imaging is the reporter gene imaging. For this strategy, biomarkers are artificially introduced into targets of interest. These artificially introduced reporter genes can be of various kinds: they can either serve as direct reporters (e.g. GFP), which need no further targeting by probes but can be detected directly by the specific modality, or they are members of one of the three classes of reporter genes, which are receptors, enzymes and transporters and can be detected indirecty via labeled probes [85-88].

Two very prominent and well-characterized reporter genes are the sodium iodide symporter (NIS) and the herpes simplex virus 1- thymidine kinase (HSV1-tk).

NIS is a transporter protein with thirteen transmembrane domains (shown in Figure 7), which is endogenously located in the follicular cells of the thyroid and mediates the transport of iodide into the cells.

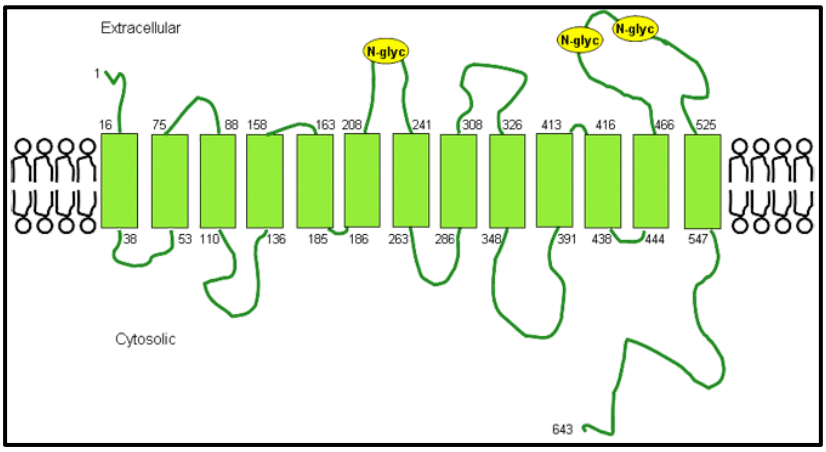

Figure 7. Schematic model of the human sodium iodide symporter (NIS).

NIS is an intrinsic protein with thirteen transmembrane domains located in the follicular cells of the thyroid (from atlasgeneticsoncology.org).

A favorable benefit of NIS is its double applicability. On the one hand it can be used as a diagnostic gene, for example, in PET imaging by the application of ^{124}I. On the other hand, it can also be exploited as a therapeutic gene by the application β-emitters, like ^{131}I. These β-emitters cause a so-called crossfire effect, which results in an additional bystander cell killing effect, since not only infected cells, which take up the therapeutic radionuclide themselves, are hit by the radiation but also neighbouring cells, which might have escaped the viral infection.

Moreover, human NIS has been used as a reporter for oncolytic viruses, such as measles [36] or oncolytic herpes simplex virus [89]. Notably, VSV was successfully equipped with NIS, allowing it to be tracked *in vivo* before [90]. Therefore, NIS was considered as an adequate candidate as reporter gene in our model.

Since for this thesis an immunocompetent rat model has been used, rat NIS (rNIS) has been tested as a reporter for imaging rVSV (rVSV-rNIS). Rat NIS had been shown previously to be highly homologous (87%) to the human

version [91, 92]. Additionally, rNIS has been reported to be superior to the human version concerning its tracer uptake efficiency [93], emphasizing its suitability as reliable *in vivo* reporter gene.

The next reporter gene tested in this thesis is a member of the class of intracellular enzymes and represents a mutant version of the HSV1-tk (HSV1-sr39tk) shown in Figure 8.

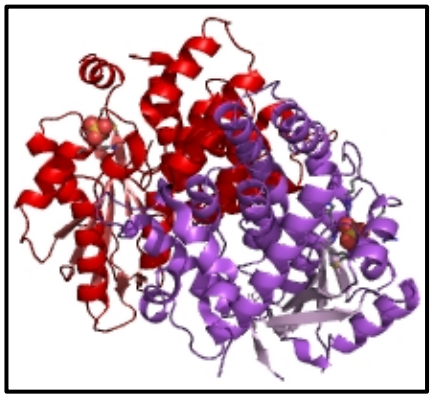

Figure 8. Crystal structure of HSV1-thymidine kinase protein.

From ebi.ac.uk.

The mutant version of this reporter was chosen, because it had been shown before to possess enhanced affinity and phosphorylation properties in comparison to the wt version [94]. Vectors equipped with the gene of this reporter protein are detectable by PET after application of an appropriate radionuclide-labeled tracer. ^{18}F-FHBG (9-(4-[18F]-fluoro-3-[hydroxymethyl]butyl)guanine) is one of these tracers, which showed favorable pharmacokinetics and dosimetry in humans and was defined to be safe in preclinical evaluations [95, 96].

The combination of the HSV1-sr39tk reporter together with the ^{18}F-FHBG tracer was demonstrated as suitable combination in other imaging studies with hepatic

targets before [97, 98]. Hence, this combination has been selected as an eligible candidate system to detect VSV via PET/CT in the liver.

1.3.2 Tumor response imaging by PET

Accurate detection and staging is crucial in the management of patients with malignant tumors. A well characterized and versatile tracer in cancer imaging by PET is ^{18}F-fluorodeoxyglucose (^{18}F-FDG). FDG is a glucose-analogue, which is not only used for the detection of tumors but also has various imaging applications in other fields, like brain imaging [99, 100] or cardiac imaging [101]. When FDG-PET is applied for the detection of tumors, the uptake of FDG in tumor tissues is due to the Warburg effect seen in aggressive, fast growing cancers. These tumors tend to have alterations in their metabolism and develop increased uptake levels of glucose. Hence, the uptake of glucose by a tumor, in theory correlates with its growth and malignancy, and a comparison of FDG uptakes by the tumor pre- and post-treatment can give precious information regarding the response of the tumor to therapy [102-104].

Nevertheless, ^{18}F-FDG is not the ideal tracer for answering questions concerning tumor responses [105]. A very unfavorable attribute of FDG is its accumulation in inflamed tissues [106-108]. Notably, FDG has already been stated as not optimal for the detection of cancer lesions in the liver [109, 110].

Many other PET tracers are available for the detection and characterization of various kinds of lesions, and this thesis focused on finding a specific tracer for imaging responses of HCC lesions upon VSV treatment. Two candidate tumor response PET tracers, possibly adequate for imaging responses to VSV therapy in HCC, are O-(2-(^{18}F)fluoroethyl)-L-tyrosine (^{18}F-FET) and 3´-deoxy-3´-^{18}F-

fluorothymidine (^{18}F-FLT).

FET is a fluoroalkylated analogue of tyrosine, an essential amino acid. FET has been well established for the imaging of brain tumors [111, 112] and shows advantages over FDG for discrimination between tumor lesions and inflamed tissues [113]. The principle of the FET tracer is that an increase in cell proliferation and growth results in an upregulation of protein use for production of novel membranes and other cell compartments. Thus, the uptake of amino acids should, in theory, correlate with an increase of tumor growth in malignant lesions. The suitability of FET could also be shown for tumors other than gliomas but has not been reported for HCC before [114, 115].

FLT is a thymidine analogue, which is trapped inside cells after phosphorylation by thymidine kinase 1 [116, 117]. Higher uptake of thymidine in malignant tissues is due to their rapid growth and genome replication, which results in an enhanced need of nucleosides for DNA synthesis.

FLT has been demonstrated as a suitable tracer, showing high accumulation in proliferating tissues and malignant tumors [118], enabling detection [119-122] and staging of various kinds of cancer [123-125]. Moreover, FLT has already been reported as a suitable tracer for the imaging of proliferation of HCC [126]. Consequently, FLT was chosen as a second candidate for the imaging of HCC tumor responses to VSV therapy in this thesis.

1.3.3 Small animal imaging

There has always been the vision of being able to perform longitudinal studies in animal models in order to monitor novel therapies already at the preclinical stage. Due to the significant development of imaging modalities over the last two decades, nowadays molecular imaging is applicable to preclinical models such as rat and mouse models, the most predominant species in preclinical research.

However*, in vivo* imaging of small animals adds completely novel challenges to the hardware and the software of all imaging modalities. A number of considerations have to be included for the application of molecular imaging in a preclinical model.

First of all, novel logistical problems with the handling of the animals arise, as animals in general need to be anethesized for the acquisition of the image. But anesthesia strongly influences the biology of any organism. Normal processes can be disturbed and, for example, biodistributional patterns of the applied tracers can possibly be altered significantly.

Other crucial points are spatial resolution and contrast. Proportions are completely different to those in humans, and abnormalities in tissues or biological processes might not be detected, since they are below the detection limit [127]. Some examples of spatial resolutions of different preclinical imaging modalities are shown in Table 1.

Table 1. Performance parameters of small animal imaging modalities

Modality	Spatial resolution	Intrinsic contrast	Probe or contrast agent sensitivity
MRI	≤ 100 µm	high	µM - mM
PET	1 - 2 mm	none	sub pM
SPECT	0.5 - 2 mm	none	sub pM
CT	≤ 200 µm	high among soft tissue, lung and bone; none among soft tissues	mM

Nevertheless, small animal imaging is already established and applied in biomedical research and offers incomparable possibilities in the study of diseases and also in the development of novel drugs and therapies.

2 AIMS OF THE THESIS

Oncolytic viruses are a highly promising novel cancer therapeutic and have been in the focus of research over the last decades, resulting in relevant findings for and improvements of the treatment of various cancers. Many OVs have already been or currently are involved in clinical studies. Especially with this current status and background, the necessity of a trackable vector, whose distribution can be followed after application to the patient, becomes crucial in order to improve the safety of OV therapy.

Therefore, the first aim of this thesis was the establishment and characterization of a novel non-invasively *in vivo* trackable VSV vector.

To date, OV therapy does not represent a path of standard therapy for cancer patients. The mechanisms, occuring inside the patients upon application are not fully understood yet. This is due to the complexicity of the tumor responses to oncolytic virotherapy, which is targeting cancerous tissue and its microenvironment at various levels. This situation strongly impedes the application of an eligible tumor response tracer, since these usually detect one specific mechanism.

Since there is no established PET tracer for imaging tumor responses to oncolytic virotherapy, the second aim of this thesis was the screening and comparison of different tumor response PET in order to identify an eligible oncolytic virotherapy PET response tracer.

3 MATERIAL & METHODS

3.1 Material

Please see the lists provided in the appendix (chapter 8) for detailed information on equipment, consumables, chemicals and commercially available buffers, as well as kits and enzymes and applied software.

3.1.1 Primers

All primers were purchased from Metabion (Martinsried, Germany)

Table 2. ***Primers***

Name	Sequence
rNIS-NheI fwd	agt aaa gct agc gcc acc atg gag ggt gcg gag gc
rNIS-HindIII rev	ctg tac gat aag ctt tca gag gtt ggt ctc cac at
rNIS-XhoI fwd	tca gct agt cac tcg agg cca cca tgg agg gtg cgg agg c
rNIS-NheI rev	agt aaa gct agc tca gag gtt ggt ctc cac at
HSV1-sr39tk-NheI fwd	agt aaa gct agc gcc acc atg gct tcg tac ccc ggc ca
HSV1-sr39tk-HindIII rev	tac tga cta agc ttt cag tta gcc tcc ccc atct
HSV1-sr39tk-XhoI fwd	att ata ctc gag gcc acc atg gct tcg tac ccc ggc ca
HSV1-sr39tk-NheI rev	agt aaa gct agc tca gtt agc ctc ccc cat ct
McyA	ggc gaa tgg gtg agt aac acg
MycB	cgg ata acg ctt gcg acc tat g

3.1.2 Plasmids

3.1.2.1 Commercially available and published plasmids

pcDNA3.1 (-) Invitrogen, Life Technologies

pVSV-GFP published [73]

pVSV-lacZ published [76]

3.1.2.2 Plasmids constructed for this project

- **pcDNA3.1-rNIS**
- **pcDNA3.1-HSV1-sr39tk**
- **pVSV-rNIS**
- **pVSV-HSV1-sr39tk**

3.1.3 Antibodies

3.1.3.1 Primary antibodies

Table 3. ***Primary antibodies***

	Company	**Host**	**Application**
α-VSV-G	Rockland	Rabbit	WB, IF
α-rNIS	Santa Cruz	Rabbit	WB
α-rNIS	kindly provided by Elena Mitrofanova	Rabbit	IF
α-HSV1-tk	Santa Cruz	Goat	WB
α-HSV1&2-tk	Bioworld Consulting Lab	Mouse	IHC, IF
α-actin	Sigma-Aldrich	Mouse	WB

3.1.3.2 Secondary antibodies

3.1.3.2.1 Peroxidase-conjugated secondary antibodies

Table 4. ***Peroxidase-conjugated secondary antibodies***

	Company	**Host**	**Application**
α-mouse	Jackson Immunoreserach	Goat	WB
α-rabbit	Jackson Immunoreserach	Goat	WB
α-goat	Santa Cruz	Donkey	WB

3.1.3.2.2 Fluorophore-conjugated secondary antibodies

Table 5. ***Fluorophore-conjugated secondary antibodies***

	Company	**Host**	**Fluorophore**	**Application**
α-mouse	Jackson Immunoreserach	Goat	Cy3	IF
α-rabbit	Jackson Immunoreserach	Goat	FITC	IF

3.1.4 Cell lines, virus strains and bacterial strains

3.1.4.1 Cell lines

Cell lines were originally obtained as frozen cultures from ATCC (Manassas, VA, USA):

Table 6. ***Cell lines***

Name	**Organism**	**Cell type**	**Tissue**	**Disease**
BHK-21	*Mesocricetus auratus*	Fibroblast	Kidney	Normal
McA-RH7777	*Rattus norvegicus, Buffalo*	HCC	Liver	Morris Hepatoma

3.1.4.2 Newly established cell lines

Table 7. ***Newly established cell lines***

Name	**Origin**	**Modification**
Morris rNIS # 9	McA-RH7777	stably expressing rNIS
Morris tk #13	McA-RH7777	stably expressing HSV1-sr39tk

3.1.4.3 Virus strains

3.1.4.3.1 Published virus strains

Virus strains are all based on VSV_{IN} (see chapter 1.2.2) with transgenes cloned as additional transcription units between G and L as depicted in Figure 9.

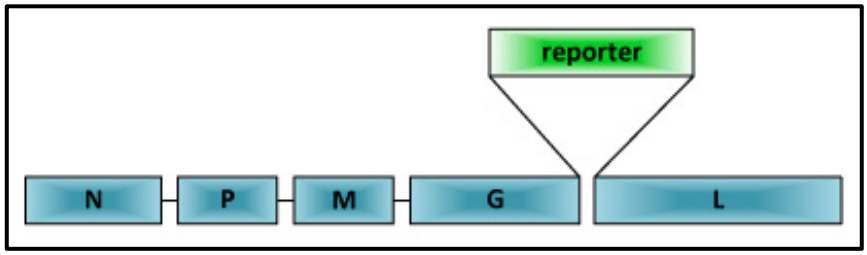

Figure 9. Diagram of recombinant VSV vectors

Transgenes are located at position 5 between the G- and L-genes. All recombinant VSV vectors used in this thesis had a reporter gene located in this position.

- rVSV-GFP [73]
- rVSV-lacZ [76]

3.1.4.3.2 Virus strains cloned for this project

- rVSV-rNIS
- rVSV-HSV1-sr39tk

3.1.4.4 Bacterial Strains

Competent *Escherichia coli* strains were purchased from Invitrogen Life Technologies (Germany).

Table 8. ***Bacterial strains***

Name	**Species**	**Applications**
MAX Efficiency DH5α	*E. coli*	Cloning
MAX Efficiency Stbl2	*E. coli*	Cloning

3.1.5 Buffers, solutions and media

3.1.5.1 Media for cell culture

Morris DMEM

containing L-Glutamine

10 % (v/v) FCS (heat inactivated)

1 % (v/v) Penicillin/Streptomycin

BHK-21 G-MEM

containing L-Glutamine

10 % (v/v) FCS (heat inactivated)

1 % (v/v) Tryptose phosphate broth solution

1 % (v/v) Penicillin/Streptomycin

3.1.5.2 Solutions for cell culture applications

Crystal Violet	12.25 mM	Crystal violet
	137 mM	Sodium chloride
	5 % (v/v)	Formaldehyde (37 %)
	50 % (v/v)	Ethanol
	in ddH_2O	
Agarose Overlay	1.5 % (w/v)	Agarose
	in PBS	
TCID50 assay	Opti-Pro	
	1x L-Glutamine	

3.1.5.3 Media for bacterial applications

All media were autoclaved for 20 min at 121 °C prior to use.

LB medium	20 g/L	LB Broth
	in ddH_2O	
LB agar	4 % (w/v)	LB Agar
	in ddH_2O	

For bacterial selection, LB medium and LB agar were supplemented with ampicillin (100 µg/ml).

3.1.5.4 Buffers and solutions for protein biochemistry

Here only reagents, which were prepared specially, are listed. For off-the-shelf reagents please see appendix.

1 x Blotting Buffer	100 mL	10 x Blotting Buffer
	200 mL	Methanol absolute
	700 mL	ddH_2O
PBS	1 M	Phosphate-HCl pH 8.0
	150 mM	Sodium chloride
	in ddH_2O	
PBS-T	1x PBS	
	0.25 % (v/v)	Tween-20
Blocking Buffer	5 % (w/v)	Blotting Grade Blocker in PBS-T
APS solution	10% (w/v)	in ddH_2O

3.2 Methods

Commercially available kits were used according to the manufacturer's guidelines.

3.2.1 Tissue culture

3.2.1.1 Cell lines

Morris cells (Mca-RH7777) were maintained in Dulbecco's Modified Eagles Medium (DMEM 30-2002; ATCC, Manassas, MA) supplemented with 10% FCS.

Stable Morris cell lines were maintained in the standard Morris cell medium and kept under constant selective pressure by supplementation with 400µg/ml Geneticin.

BHK-21 cells were maintained in Glasgow Minimal Essential Medium (G-MEM BHK-21; Gibco, life technologies, UK) supplemented with 1% Tryptose Phosphate Broth Solution (Sigma Aldrich Company, UK) and 10% FCS.

Cells were kept in a humidified atmosphere at 5% CO_2 and 37°C.

Mycoplasma PCR was performed once per month in order to rule out contamination. Primer sequences are shown in 3.1.1.

3.2.1.2 Stable transfection of cell lines

Stable Morris cell lines were generated in this project: one expressing hNIS and the other expressing HSV1-sr39tk. Initial transfections were performed with pcDNA3.1 plasmids expressing either hNIS or HSV1-sr39tk using Lipofectamine 2000 Reagent. 24 hours after transfection, selection pressure was applied by administration of Geneticin (400 µg/mL). Resistant clones were picked and indivually screened for functional reporter protein expression by Western Blot analysis (SDS-PAGE + Immunoblotting), immunofluorescence microscopy and *in vitro* tracer uptake assay.

3.2.2 Molecular Biology

3.2.2.1 Analysis and cloning of DNA

3.2.2.1.1 PCR amplification of DNA inserts for cloning

PCR amplification was done with the Takara PrimeSTAR GXL DNA Polymerase following the manufacturer's instructions. For amplification of inserts for cloning into the pcDNA3.1 plasmid respective primers "NheI fwd" and "HindIII rev" were used; for cloning into the pVSV plasmid respective primers "XhoI fwd" and "NheI rev" were used (for primer sequences see Table 2).

3.2.2.1.2 Restriction enzyme digestion

Restriction digestion of plasmids or PCR products was performed in a total volume of 20 µL and according the manufacturer's guidelines. Reactions were incubated for 4 h at 37 °C.

3.2.2.1.3 Agarose gel electrophoresis

DNA fragments obtained by restriction digest or PCR were separated and analyzed by agarose gel electrophoresis. All agarose gels were prepared in 1 x TAE buffer with 1% agarose. To stain DNA fragments, ethidium bromide was added to a final concentration of 100 ng/mL before pouring the gel into the gel preparation tray. Samples were mixed with 5x loading dye in a ratio of 4:1. For size determination of the fragments and concentration estimations of the samples, 5 µL of either a 100 bp or 1 Kb DNA ladder were added to the gel and run together with the samples. Agarose gels were run in 1 x TAE buffer and separated at 100 V for 1 h. DNA bands were visualized Biorad Gel Doc XR+ system and analysed by the corresponding software.

3.2.2.1.4 Extraction of DNA fragments from agarose gels

For extraction of DNA fragments from agarose gels the QIAquick Gel Extraction Kit was applied accoring the manufacturer's guidelines.

3.2.2.1.5 Ligation of plasmids

Ligation of plasmids with inserts was performed with the Quick Ligation Kit (NEB), following the manufacturer's guidelines.

3.2.2.1.6 Sequencing of plasmids

Correct sequences of novel plasmids were checked by DNA sequencing (performed by Eurofins MWG Operon, Martinsried, Germany), and alignment analysis was performed using the MacVector Software.

3.2.2.2 Isolation and purification of DNA

3.2.2.2.1 Transformation of competent E. coli

Chemically competent *E. coli* DH5α cells were used for transformations of pcDNA3.1-based plasmids, and *E. coli* Stbl2 cells were used for transformations of pVSV-based plasmids, following the manufacturer's protocols. Briefly, bacteria were thawn on ice and about 10 ng of Plasmid-DNA were added. After incubation on ice for 30 min, heatshock was performed for 45 s (DH5α) or 25 s (Stbl2) at 42°C. Cells were put back on ice immediately for another 2 min. Subsequently, S.O.C. medium was added and cultures were incubated for 1 h at 37 °C (DH5α) or 1.5 h at 30 °C (Stbl2), shaking at 225 rpm. Afterwards, bacteria were spread onto LB agar plates containing ampicillin. Plates were incubated overnight at 37 °C (DH5α) or 30°C (Stbl2).

3.2.2.2.2 Isolation of plasmid DNA

Small scale (miniprep) and medium scale (midiprep) isolation of plasmid DNA were performed using the respective kits from Qiagen following the manufacturer´s instructions.

3.2.2.2.3 Determination of DNA concentration

DNA concentration and purity were determined by measurement of the optical density (OD) at 260 nm and 280 nm by a spectrophotometer. An OD of 1 at OD_{260} refers to a double stranded DNA concentration of 50 µg/mL.

3.2.2.2.4 Determination of DNA purity

The ratio of OD_{260} to OD_{280} expresses the purity of the sample and possible protein contaminations. Only samples of high purity were used for further experiments ($OD_{260/280}$ ~1.8).

3.2.3 Protein biochemistry

3.2.3.1 Preparation of cell lysates

Cells were harvested and pellets of the respective samples were lysed in 1x cell lysis buffer supplemented with protease inhibitor and phosphatase inhibitor. Lysis was always carried out on ice and samples were stored at -20°C.

3.2.3.2 Determination of protein concentration

Protein concentration of samples was measured by photometric analysis using the Pierce BCA Protein kit according to the manufacturer's guidelines. Measurement was done with Spectrophotometer SmartSpec Plus (Bio-Rad).

3.2.3.3 SDS polyacrylamide gel electrophoresis (PAGE)

Proteins were separated by SDS-PAGE. Resolving gels were used at a polyacrylamide concentration of 7.5%. Protein samples were mixed 1:1 with 2x Laemmli buffer (incl. 5% β-Mercaptoethanol, both from Biorad) and incubated for 5 min at 95 °C before they were loaded on the gel. Additionally a protein size standard was added. Gels were run in 1x running buffer at 120 V for 100 min at 4°C.

Table 9. ***Composition of SDS-PAGE gels***

	Resolving Gel	***Stacking Gel***
	7.5%	**4%**
Acrylamide solution	2.5 mL	0.666 mL
4 x Resolving Gel Buffer	2.5 mL	---
4 x Stacking Gel Buffer	---	1.25 mL
SDS	100 µL	50 µL
ddH_2O	4.85 mL	3 mL
10 % APS	50 µL	25µL
TEMED	5 µL	5 µL

3.2.3.4 Immunoblotting

After SDS-PAGE the separated proteins were transferred to a nitrocellulose membrane by wet electroblotting at 4°C for 1 h at 120 V.

3.2.3.5 Protein detection by horseradish-peroxidase induced chemiluminescence

After blocking in 5% WB blocking buffer, the membrane was subsequently incubated with the respective antibodies at 4 °C over night. Membranes were then washed three times in PBS-T for 5 min at RT before they were incubated with the respective horseradish peroxidase-conjugated secondary antibodies and washed again three times in PBS-T. Detection of the proteins was done with Amersham ECL Prime Western Blotting Detection Reagent as recommended by the manufacturer. Detection was performed on CL-XPosure Film (Thermo Fisher Scientific).

If more then one protein was detected on the same membrane, antibodies were stripped by incubation of the membrane in Western Blot Stripping Buffer, following the manufacturer's protocol before detection of another protein was performed.

3.2.4 Indirect immunofluorescence microscopy

Cells were plated on Chamber Culture Slides. Virus samples were infected at an MOI of 1 for 8 h. All samples were fixed for 15 min with 4% paraformaldehyde before they were quenched by incubation with 50 mM NH_4Cl and permeabilized by incubation with MeOH. Afterwards samples were blocked in 5% horse serum and incubated with antibodies VSV-G-protein and HSV1&2-tk at 4 °C over nigth. Afterwards respective fluorophore-conjugated, secondary antibodies (α-rabbit and α-mouse) were added. All samples were counterstained in the nuclei, with DAPI, PI or Hoechst before they were mounted with Roti-Mount FluorCare and visualized by the Zeiss AxioVert microscope.

3.2.5 Virus work

3.2.5.1 Cloning of recombinant vectors

The rNIS gene or the HSV1-sr39tk gene, respectively, was cloned into the VSV vector in between the G- and L-protein as described before [128, 129]. To generate recombinant VSV expressing the reporters, the sequences were amplified by PCR from plasmid (rNIS-containing plasmid pS5-rNIS was a kind gift from Elena Mitrofanova; HSV1-sr39tk-containing plasmid was a kind gift

from Dr. Martina Anton, TU München) using the forward and reverse primers containing unique restrictions sites for *XhoI* and *NheI*, respectively. The PCR product was digested with *XhoI* and *NheI,* as well as a pVSV plasmid before the novel insert was ligated into the pVSV vector.

Afterwards, the recombinant constructs were rescued as described previously [130, 131]. Briefly, individual plasmids encoding T7 promoter-driven VSV nucleoprotein (N), phosphoprotein (P) and polymerase (L) were transfected into BHK-21 previously infected with vTF-7.3, a recombinant vaccinia virus expressing T7 polymerase. In addition, a plasmid encoding the full-length antigenomic VSV RNA with insertion of the respective reporter gene transcription unit into the 3`noncoding region of the VSV-G gene was also co-transfected into the cells. After successful recovery of recombinant VSV, vaccinia virus was completely eliminated by plaque purification.

3.2.5.2 Virus propagation

For production of stocks of various VSV vectors, BHK-21 cells were infected with the respective virus vector at an MOI of 0.0001. Infected cells were cultured for approximately 48 hours, or until a strong cytopathic effect was visible. At this time point virus-containing supernatant was harvested and centrifuged at 2,500 rpm for 5 min in order to get rid of cell debris of the lysed cells.

3.2.5.3 Purification of virus stocks

For *in vivo* applications, virus preparations needed to be purified by sucrose gradient centrifugation. Therefore, the cleared cell culture supernatant was centrifuged for 1 h at 25,000 rpm in an ultracentrifuge. The obtained pellet was resuspended in PBS and applied to a sucrose gradient:

Top layer	10% sucrose	3 mL
Middle layer	30% sucrose	6 mL
Bottom layer	60% sucrose	7 mL

Gradient and virus were centrifuged for another hour at 25,000 rpm. The resulting virus-containing band was collected carefully using a 3ml syringe and 20g needle and aliquoted. Aliquots were stored at -80°C.

3.2.5.4 Determination of viral titer by plaque assay

In order to determine the viral titers of virus stocks plaque assay was performed as described before [132]. Therefore, BHK-21 cells were plated into 6-well plates and infected with different dilutions of the newly generated virus stocks in 10-fold dilution steps diluted in 1x PBS containing Ca^{2+} and Mg^{2+} for 45 min at RT. Afterwards, cells were washed three times with 1x PBS before the infected cell layers were overlayed with an agarose overlay, prepared by combining equal volumes of 1.5% agarose and complete BHK-21 medium, in order to avoid diffusion and subsequent novel infection of possibly released virus progeny. After approximately 36 h plaques were formed. At that time point the agarose overlay was carefully removed and cells were stained and fixed with 1 mL crystal violet solution per well for 30 min at RT. Cells were rinsed with tap water and plaques were counted to determine the viral titer.

3.2.5.5 Determination of viral titers by $TCID_{50}$ assay

In order to quantify the virus content of different samples the tissue infective dose 50 assay ($TCID_{50}$ assay) was performed. This assay is based on the cytopathic effect (CPE) of the virus and can only be used on susceptible cells. Here, VSV was used on BHK-21 cells. Briefly, cells were plated on 96-well plates. When they reached a confluence of approximately 70%, 10-fold serial dilutions of each virus sample were prepared. 100 µL of each dilution was added to four different wells of cells. After 48 h, wells have been checked for CPE and viral titer was calculated by the Reed & Münch endpoint calculation method.

3.2.5.6 Virus growth curve

Morris cells were plated into 24-well plates. After 24 hours, when cells reached a confluence of 70%, infection followed at an MOI of 0.01 and of 10, respectively, for 30 min at 37°C. After the infection, cells were washed three times with 1x PBS before fresh medium was added. Supernatant was collected at several time points after infection (0, 8, 12, 24, 48, 72, 96 hours). The viral titers were determined by $TCID_{50}$ assay (50% tissue culture infective dose) on BHK-21 cells. Data points are presented as mean +/- SD.

3.2.6 *In vitro* cell proliferation assay

In order to determine the oncolytic potency of newly generated recombinant viruses, *in vitro* cell killing assays were performed. Therefore, Morris cells were plated in 96-well plates. After 24 hours, when cells reached a confluence of 70%, infection followed with an MOI of 0.01 and of 10, respectively. Cell viability was tested at various time points after infection by MTS assay (CellTiter96

AQ_{ueous} One Solution Cell Proliferation Assay). Values are expressed as percentage of viable cells and are normalized to respective uninfected controls at each time point. Data points are presented as mean +/- SD.

3.2.7 *In vitro* tracer uptake assay

Cells were plated in 12-well plates. Those samples dedicated to virus infection were infected 16 hrs before uptake at an MOI of 0.1.

1 MBq of the respective tracer (i.e. ^{125}I for hNIS samples and ^{18}F-FHBG for HSV1-sr39tk samples) was added to each well. Subsequently, cells were incubated at 37°C for 45 min. Supernatant was removed and cells were washed twice with ice-cold PBS before they were lysed in 1N NaOH. Tracer uptake was measured in a γ-counter.

For normalization, cells were counted in a Neubauer counting chamber. A mean of three wells of each sample was normalized to the value of untreated wt cells. The uptake values of the individual samples were then normalized to the respective cell number ratios.

3.2.8 Morris hepatoma model

The Morris hepatoma model is an implantable model of HCC in immunocompetent, syngeneic Buffalo rats. A big advantage of this model is that the tumors can be implanted in various manners, so that different locations and numbers of lesions can be chosen according to the experimental outline of the study. Implantable models in general have the benefit of accurate predictability of the tumor growth so that the fault rate in these models is low. Another advantage of this model is its clinical relevance. The resulting pattern of lesions

in the multifocal orthotopic model is comparable to the clinical situation. Although immunocompetent models are especially challenging, they are crucial for achieving relevant information for the translation into the clinic.

The similarity of this model to human HCC can also be seen Figure 10. The comparison of an MRT scan of an HCC bearing rat with a scan of a patient shows the same distribution and growth of tumors and similar tissue density.

Rat HCC **Human HCC**

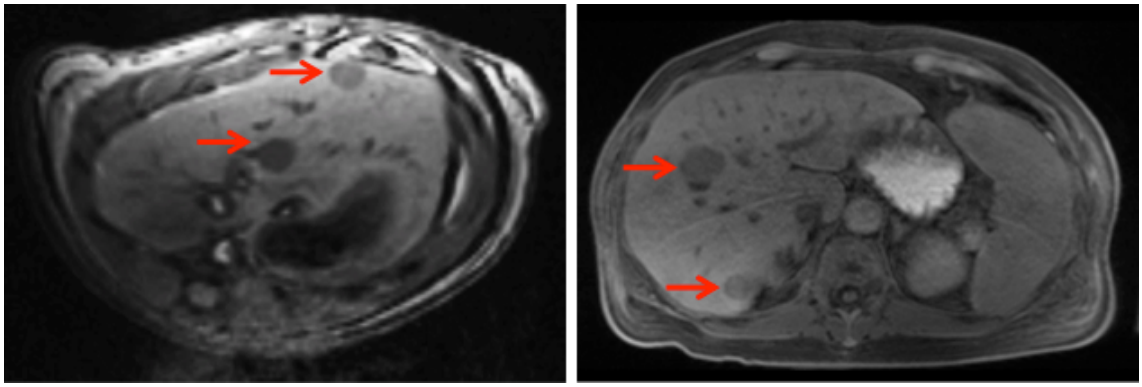

Figure 10. Comparison of the Morris hepatoma model to the clinical scenario of HCC.

MRT T1-weighted images of the liver of a Buffalo rat implanted with multifocal orthotopic HCC lesions and of a human liver of a HCC patient. Arrows point to HCC lesions. Both images were kindly provided by Dr. Rickmer Braren, Department of Radiology, Klinikum rechts der Isar TUM

3.2.8.1 Subcutaneous HCC tumor model

1 x 10^6 Morris cells were resuspended in 100 µL of OPTI MEM and injected subcutaneously into the flanks of Buffalo rats. After 14 days tumors reached a size of approximately 0.5 to 1 cm in diameter and were ready for further applications.

3.2.8.2 Orthotopic unifocal HCC implantation

Buffalo rats were anaesthesized by Isoflurane inhalation. The abdominal cavities were opened, and 4 x 10^6 Morris cells, resuspended in 20 µL OPTI MEM, were injected directly into the capsule of the left liver lobe. The injection site was cauterized after application to prevent bleeding and leakage of tumor cells into the peritoneum . After 10 days, tumors reached a size of approximately 0.5 to 1 cm in diameter. At this time point, the tumors had the optimal size for further applications.

3.2.8.3 Intratumoral virus injection

Buffalo rats were anaesthesized by Isoflurane inhalation. Abdominal cavities were opened for a second time, and application of the respective virus solution or the PBS control (100 µL total volume, respectively) was applied directly into the tumor.

3.2.8.4 Intra-arterial virus injection

Buffalo rats were anaesthesized by Isoflurane inhalation. Animals were laparotomized for a second time, and application of the respective virus solution or the PBS control (1 mL total volume) was applied into the hepatic artery as previously described [76] and illustrated in Figure 11.

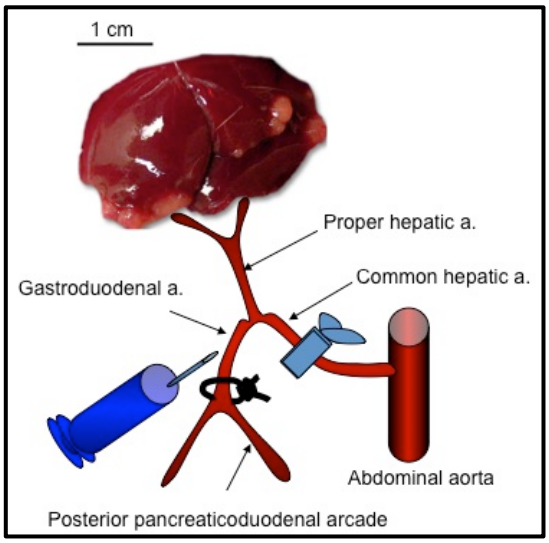

Figure 11. Intra-arterial injection into the gastroduodenal artery in Buffalo rats.

Shown is a representative Buffalo rat liver with multifocal HCC lesions. After the gastroduodenal artery is ligated permenantely, the common hepatic artery is temporarily blocked. Then the virus solution is applied into the gastroduodenal artery above the permanent ligation. Subsequently, a second permanent ligation above the injection site is applied to prevent bleeding, when blockade of the common hepatic artery is released. Figure taken from Shinozaki et al., 2004.

3.2.9 Small animal imaging

3.2.9.1 Micro CT

For contrast enhanced CTs, ExitronNano12000 [133] was applied 24 h before image acquisition at a dose of 2 mL/kg i.v. into the tail vein. In case of multiple imagings of the same animal, contrast agent was only applied once before the first time point.

3.2.9.1.1 Low-contrast CT

Acquisition consisted of 121 projections acquired with exposure time of 200 ms, x-ray voltage of 80 kVp and anode current of 500uA. Images were reconstructed using a modified Feldcamp algorithm. The resulting matrix was 256x256 pixels with 631 transverse slices (reconstructed pixel size 0.21 x 0.21 x 0.21 mm).

3.2.9.1.2 High-contrast CT

Acquisition consisted of 271 projections acquired with exposure time of 400ms, x-ray voltage of 80 kVp and anode current of 400uA. Images were reconstructed using a modified Feldcamp algorithm. The resulting matrix was 256x256 pixels with 384 transverse slices (reconstructed pixel size 0.21 x 0.21 x 0.21 mm).

3.2.9.2 Micro PET

All scans were performed using a small-animal in-line PET/CT scanner (Inveon, Siemens Medical Solutions, Knoxville, Tenn, USA). Animals were anaesthetised using 1.5% isoflurane, while breathing was monitored and temperature was maintained using a heating pad throughout the imaging procedures. Tracer injections were done i.v. into the tail vein. Rats were allowed to wake up in between tracer injection and image acquisition. For the image acquisition rats were anaesthetised for a second time as described before.

3.2.9.2.1 ^{124}I PET

22 MBq of ^{124}I (commercially available) were applied per animal. Scans were performed 2, 4 and 24 h after tracer application. Static PET data was acquired for 15 min and reconstructed using a 2D-filtered back-projection algorithm. Additionally, animals have been treated with L-T_4 (L-thyroxin) for 10 days at 5 mg/L in the drinking water prior to imaging in order to prevent thyroidal iodine-tracer uptake.

3.2.9.2.2 ^{18}F-FDG PET

^{18}F-FDG was prepared as previously described [134]. 20 MBq of ^{18}F-FDG were applied per animal. All animals were fasted 120 min prior to image acquisition. Scans were performed 45 min after tracer application. Static PET data was acquired for 15 min and reconstructed using a 2D-filtered back-projection algorithm.

3.2.9.2.3 ^{18}F-FET PET

^{18}F-FET was prepared as previously described [135]. 20 MBq of ^{18}F-FET were applied per animal. Scans were performed 45 min after tracer application. Static PET data was acquired for 15 min and reconstructed using a 2D-filtered back-projection algorithm.

3.2.9.2.4 ^{18}F-FLT PET

^{18}F-FLT was prepared as previously described by Machulla et al. 2000. 20 MBq of ^{18}F-FLT were applied per animal. Dynamic scan was performed with on-bed tracer application for 115 min. Static scans were performed 45 min (Figure 52 and Figure 53) or 105 min (Figure 55 and Figure 56) after tracer application. PET data was reconstructed using a 2D-filtered back-projection algorithm.

3.2.9.2.5 ^{18}F-FHBG PET

^{18}F-FHBG was prepared as previously described [136]. After i.v. injection of 40 MBq of ^{18}F-FHBG into the tail vein, rats were allowed to wake up from anaesthesia again before static image acquisition was performed 2 h later for 15 min. PET data were reconstructed using a 3D-filtered back-projection algorithm.

3.2.9.3 Image analysis by Siemens INVEON Research Workplace

Image analysis was performed on the INVEON Research Workplace (Siemens, Knoxville, Tenn, USA). CT images were scaled for best visualisation, while PET intensities are indicated in the respective legends.

Resulting CT and PET images were carefully aligned. 3-dimensional regions of interest (ROIs) were drawn manually around important areas (i.e. liver, whole tumor, spinal muscle) based on the anatomical information given by the CT signal. Mean activities from the entire ROIs were automatically calculated by the software and expressed in Bq/mL.

All uptake tissue values were normalized to the spinal muscle of each respective animal.

3.2.9.4Statistical analysis

Mean values and SD or SEM were calculated, analysed and graphically expressed by Prism GraphPad.

3.2.10 *Ex vivo* tissue analysis

3.2.10.1 Tracer biodistribution assay by tissue γ-counting

Rats were euthanized directly after the last PET scan via intracardial injection of pentobarbiturate (Narcoren ®, Merial, Rohrdorf, Germany). Animals were dissected and tissues of interest were collected and weighted. The radioactivity of the tissue samples was measured by γ counting. The radioactivity decay was corrected to the time of injection by normalization of the individual samples to a tracer standard. The radioactivity that accumulated in the tissues after tracer injection was expressed as the percentage of the injected dose per gram of tissue (%ID/g).

3.2.10.2 Tissue autoradiography assay

Samples of the tissues of interest (i.e. tumor, liver, muscle) were dissected after the animals were euthanized (see above). Three slices of each tissue were fixed with 4% paraformaldehyde and subsequently, exposed overnight to a phosphoimage plate. Image plates were scanned by an image plate scanner at an internal sensitive resolution of 50 µm.

Resulting data were then aligned with the resulting data from the autoradiography to identify areas of tracer accumulation. Autoradiography analysis was performed with AIDA Image Analyser Software (Raytest Isotopenmeßgeräte, Germany).

3.2.10.3 Tissue titer assay

For measurements of tissue titers, tissues were stored at -80°C immediately after dissection. After thawing, tissues were weighted and homogenized in 10 µL of 1x PBS containing 1x penicillin/streptavidin per mg of tissue.

Subsequently, $TCID_{50}$ assay was performed from these samples.

3.2.10.4 Tissue histology

After tissues of interest were dissected and fixed in 4% paraformaldehyde, they were embedded in paraffin, and serial sections were stained with hematoxylin-eosin (HE) or after HIER immunohistochemically stained with α-rNIS or α-HSV1&2-tk for one hour using a Dako Autostainer. Detection was done by an HRP-conjugated antibody. The slides were analyzed by two blinded pathologists, and the areas of HSV-tk expression were marked.

3.2.10.4.1

4 RESULTS

4.1 Non-invasive *in vivo* imaging of recombinant VSV

4.1.1 Non-invasive *in vivo* imaging of rVSV-rNIS

4.1.1.1 Novel rVSV-rNIS could be successfully cloned and rescued

The rat sodium idodide symporter gene (rNIS) was successfully cloned into the pVSV plasmid and the novel rVSV-rNIS was rescued as described in chapter 3.2.5.1. Figure 12 depicts the resulting virus genome.

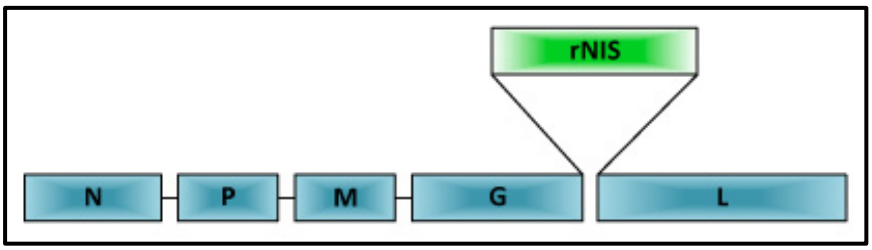

Figure 12. Schematic presentation of the genome of rVSV-rNIS.

The rNIS gene is located at position five between the G- and L-gene.

4.1.1.2 rVSV-rNIS is not attenuated in vitro

In order to characterize the novel recombinant virus rVSV-rNIS, its replication *in vitro* was tested on Morris cells (rat hepatoma cell line). To rule out potential attenuation in the replication profile a one-step (infection at MOI 10) and a multi-step (infection at MOI 0.01) growth curve was generated in comparison to an already established and characterized recombinant VSV, rVSV-GFP, which has the GFP-transgene at the same position as rVSV-rNIS. The growth curves of

both viruses are shown in Figure 13.

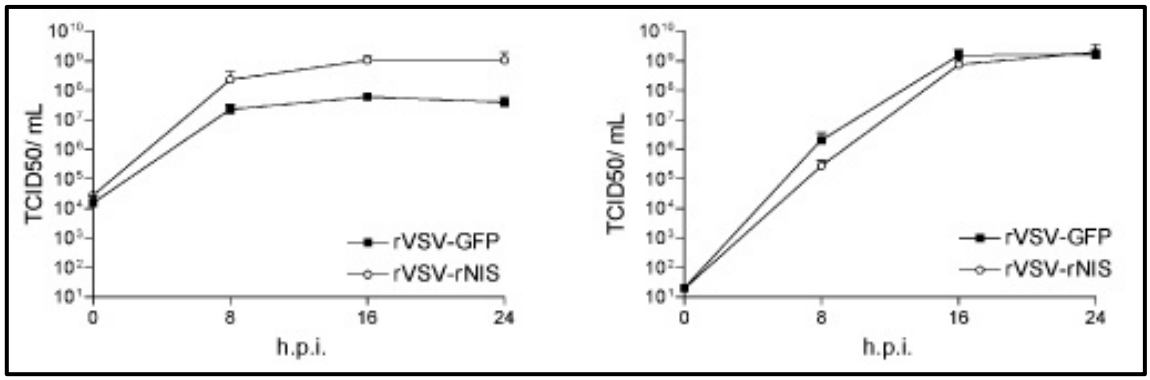

Figure 13. One-step and multi-step growth curve of rVSV-rNIS.

Viral replication was tested *in vitro* on Morris cells after an infection of MOI 10 (one-step, left panel) and MOI 0.001 (multi-step, right panel). Viral titers in the supernatant of the cell culture were detected at various time points after infection (h.p.i. = hours post infection). All samples were performed in triplicates and values are expressed as mean with SD.

The viral titers of both vectors were indistinguishable at all times points tested, indicating that the expression of the rNIS reporter gene does not alter viral kinetics (Figure 13).

4.1.1.3Morris cells express the rNIS protein after infection with rVSV-rNIS

To test the protein expression of the rNIS reporter protein upon infection with rVSV-rNIS, Morris cells were infected with the virus and, subsequently, the protein expression was detected by indirect immunofluorescence microscopy (Figure 14). Untreated Morris cells and VSV-wt-infected Morris cells were additionally monitored as negative controls.

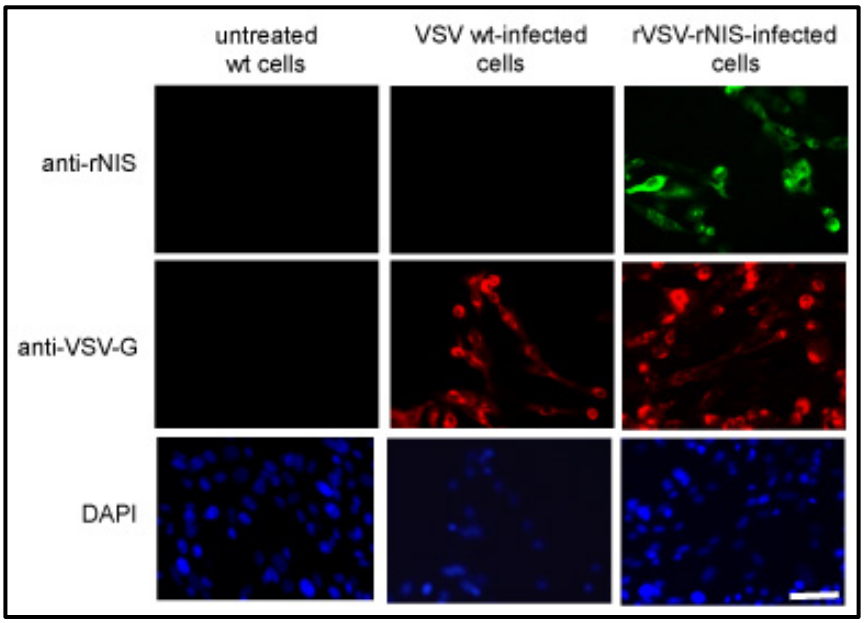

Figure 14. Indirect immunofluorescence of Morris cells after infection with rVSV-rNIS.

Untreated wt cells and either VSV-wt or rVSV-rNIS-infected cells were analysed for the expression of rNIS (green signal, upper panel) and VSV-G (red signal, second panel). As a counterstaining of all nuclei, cells were stained with DAPI (blue signal, third panel). Microscopy was performed at a magnification of 20x and scale bar refers to 100 µm.

Expression of the rNIS protein was detected in rVSV-rNIS-infected Morris cells via indirect immunofluorescence, while no expression could be detected in untreated Morris cells or VSV-wt-infected cells (Figure 14). Additionally, the expression of the VSV-G protein was tested in all samples but could only be detected in VSV-wt and rVSV-rNIS-infected cells.

These results show that rNIS-expression is exclusively induced in rVSV-rNIS-infected Morris cells. Therefore, the rNIS-signal in those cells is specific and not based on a side effect induced upon VSV-infection in general, since VSV-wt-infected cells were negative for rNIS. Additionally, no rNIS signal could be detected in Morris wt cells by indirect immunofluorescence, indicating that the endogenous expression of rNIS in Morris wt cells is below the detection limit.

This demonstrates the suitability of rNIS as suitable reporter in the Morris hepatoma model, since a low background of tracer uptake can be expected in Morris tumors *in vivo*.

4.1.1.4 Stable rNIS Morris cell line expresses the rNIS protein in vitro

For the establishment of the PET/CT imaging of rVSV-rNIS, a stable Morris cell line, expressing rNIS, was generated in order to function as a positive control, showing maximal tracer uptakes *in vitro* and later on also *in vivo*. rNIS protein expression of the stable cell line was checked by indirect immunofluorescence microscopy (Figure 15). Untreated Morris wt cells were additionally tested as a negative control.

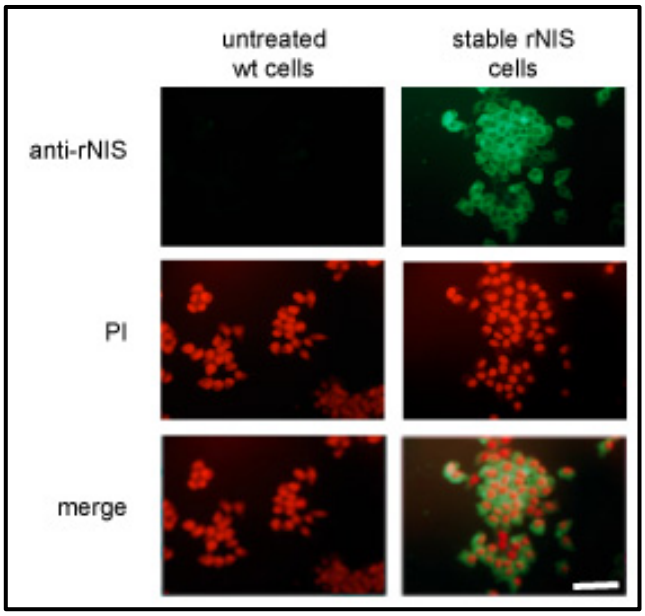

Figure 15. Indirect immunofluorescence stable, rNIS-expressing Morris cells.

Untreated wt cells and stable rNIS-expressing cells were analysed for the expression of rNIS (green signal, upper panel). As a counterstaining of all nuclei, cells were stained with PI (red signal, middle panel). Merged images of signals are shown in the lower panel. Microscopy was performed at a magnification of 20x and scale bar refers to 100 µm.

Expression of the rNIS protein was detected in the stable rNIS-expressing Morris cell line via indirect immunofluorescence. This signal could not be seen in untreated Morris cells (Figure 15). These results show that rNIS is stably expressed in the stable rNIS cell line and indicate its suitability as positive control for PET/CT *in vivo* imaging.

4.1.1.5 rVSV-rNIS-infected Morris cells and rNIS stable cell line show iodine uptake in vitro

^{125}I *in vitro* tracer uptake was performed in order to monitor the functionality of the expressed reporter protein of either rVSV-rNIS Morris wt cells or stable rNIS-expressing Morris cells *in vitro*. As a control for the specificity of the tracer uptake, a subset of the samples was treated with 10 mM $KClO_4$, which is a specific NIS inhibitor and, therefore, blocks the NIS-mediated uptake of iodine into the cells.

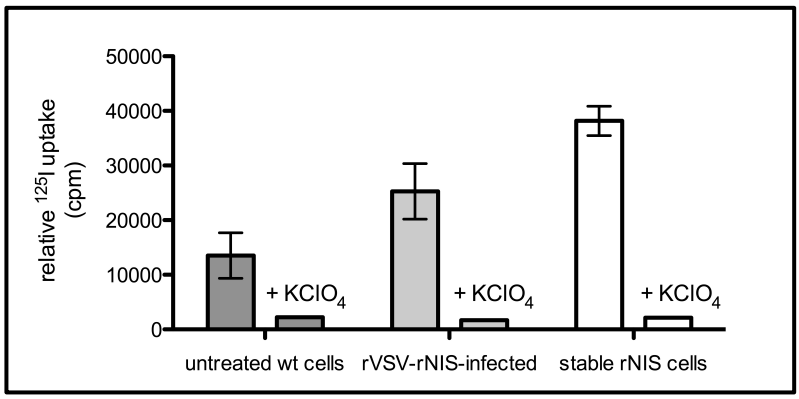

Figure 16. ^{125}I in vitro uptake of rVSV-rNIS-infected and stable rNIS-expressing Morris cells.

Shown are the means of ^{125}I uptake (cpm) and SD of untreated Morris wt cells, rVSV-rNIS-infected cells and stable rNIS-expressing Morris cells in a column bar graph. Samples were performed in triplicates and an additional sample subset of each sample was additionally

incubated with 10 mM $KClO_4$.

The results of the ^{125}I *in vitro* uptake assay show a low but specific background iodine uptake in untreated Morris wt cells (Figure 16). The rVSV-rNIS-infected cells showed an increase in specific tracer uptake, while the highest specific iodine uptake was obtained by the stable rNIS cell line. These results prove the functionality of the rNIS reporter model and indicate the suitability of the system for PET/CT *in vivo* imaging.

4.1.1.6 Stable Morris tumors expressing rNIS do not show a detectable iodine uptake in a subcutaneous model in vivo

For the establishment of the non-invasive PET imaging of rVSV-rNIS, a proof of principle imaging was performed. For this attempt, Buffalo rats were implanted with two subcutaneous tumors, one at each shoulder: a wt Morris tumor at the right flank and a stably rNIS-expressing tumor at the left shoulder. In this way, both controls, a positive by the stable tumor, and a negative control by the wt tumor could be represented in the same animal. Image acquisition has been performed 6 h after i.v. tracer application. A representative example of a PET/CT scan is shown in **Figure 17**.

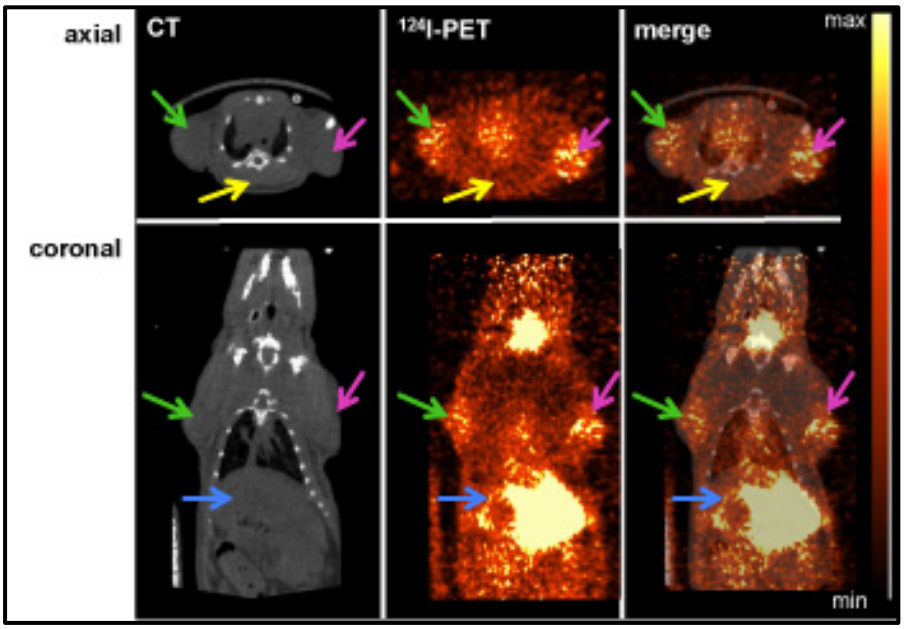

Figure 17. ^{124}I-PET/CT scan of subcutaneous HCC-bearing rats.

Representative scans of tumor-bearing rats with subcutaneous tumors at both flanks (right shoulder stable rNIS-expressing tumor, left shoulder wt tumor) in axial (upper panel) and coronal (lower panel) view. Image acquisition was performed 6 h after tracer tracer application. Areas, which were used for region of interest (ROI) analysis, are marked with arrows in green for stable tumor, magenta for the wt tumor, yellow for the muscle and blue for the liver. Native CT scans were performed at low resolution. PET intensity scale is set to 1x 10^5 Bq/mL at maximum value and 0 Bq/mL at minimum value.

Quantitative analysis of the PET/CT scans revealed a lower tracer uptake in wt tumors compared to liver and, notably, also in the tumors of the the stably rNIS-expressing cell line (Figure 18).

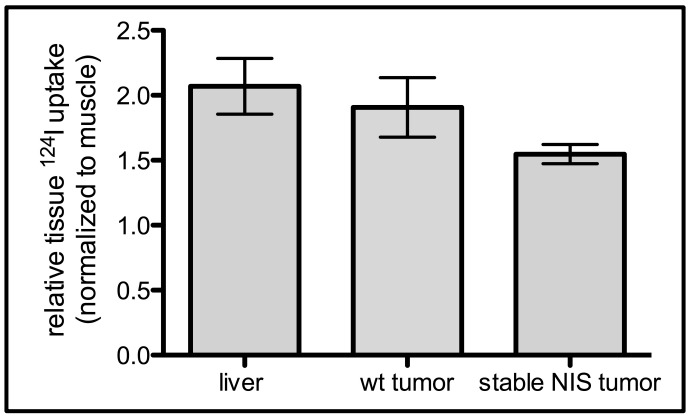

Figure 18. Quantitative analysis of ^{124}I-PET by region of interest analysis.

Results of the PET/CT imaging shown in **Figure 17** were analysed by ROI analysis. 3-dimensional ROIs were drawn manually around respective tissues. Mean uptakes of each area were normalized to muscle uptakes in each animal. Expressed are mean uptake values and SD of the respective tissue of all animals (n= 4) in a column bar graph.

Histological analysis of the tumors of animals, which were sacrificed after the scan, shows expression of the rNIS protein in the stable tumors, while no rNIS protein expression could be deteted in the wt tumors (Figure 19).

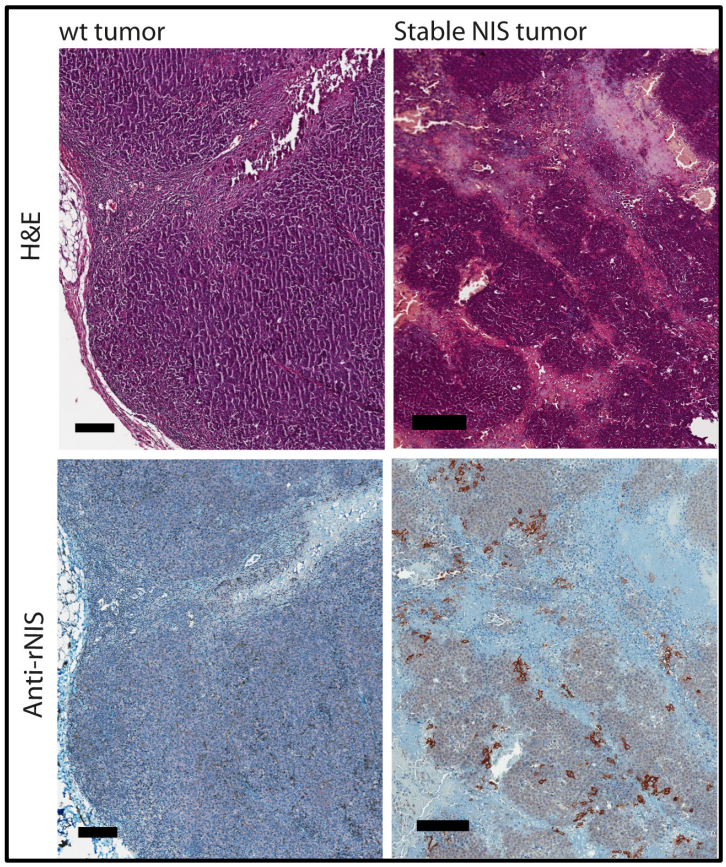

Figure 19. Histology of stable NIS tumor and untreated wt tumor.

Histological analysis of tumors of a representative animal imaged by ^{124}I-PET/CT (Figure 17). Upper panel shows H&E staining and lower panel shows respective immunohistological staining against rNIS. Bar refers to 200 µm.

4.1.1.7 Subcutaneous Morris tumors do not show iodine uptake after intratumoral treatment with rVSV-rNIS in vivo

4.1.1.7.1 ^{124}I-PET/CT scans of subcutaneous HCC-bearing rats show no increase in tracer uptake in stable rNIS-expressing or rVSV-rNIS-treated wt tumors

Since no specific tracer uptake could be detected in the stable rNIS-expressing tumors in the first imaging (chapter 4.1.1.6), for the next imaging 1x10^7 pfu rVSV-rNIS were injected intratumorally into the wt tumor. 15 h after virus application another image acquisition was performed and a representative scan

is shown in Figure 20.

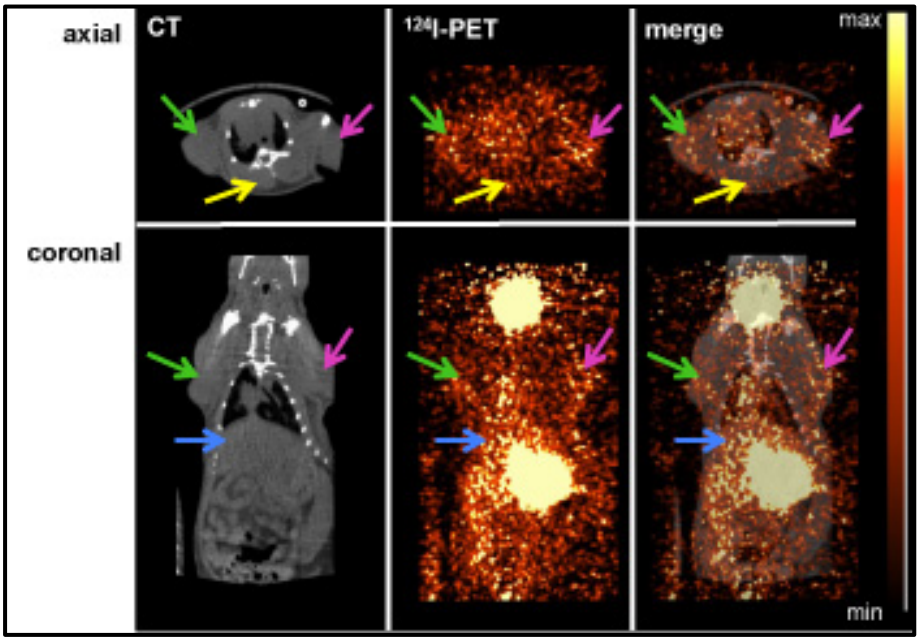

Figure 20. ^{124}I-PET/CT scan of subcutaneous HCC-bearing rats 16 h after intratumoral rVSV-rNIS injection.

Representative scans of a tumor-bearing rat with subcutaneous tumors at both flanks (right shoulder stable rNIS-expressing tumor, left shoulder wt tumor) in axial (upper panel) and coronal (lower panel) view. Image acquisition was performed 24 h after tracer tracer application. Areas used for region of interest (ROI) analysis are marked with arrows in green for stable tumor, magenta for the rVSV-rNIS-treated tumor, yellow for the muscle and blue for the liver. Native CT scans were performed at low resolution. PET intensity scale is set to 2 x 10^4 Bq/mL at maximum value and 0 Bq/mL at minimum value.

Quantitative analysis of the PET/CT scans revealed, that tracer uptake was lower in rVSV-rNIS-treated wt tumors as well as in the tumors of the stably rNIS-expressing cell line compared to liver as depicted in Figure 21.

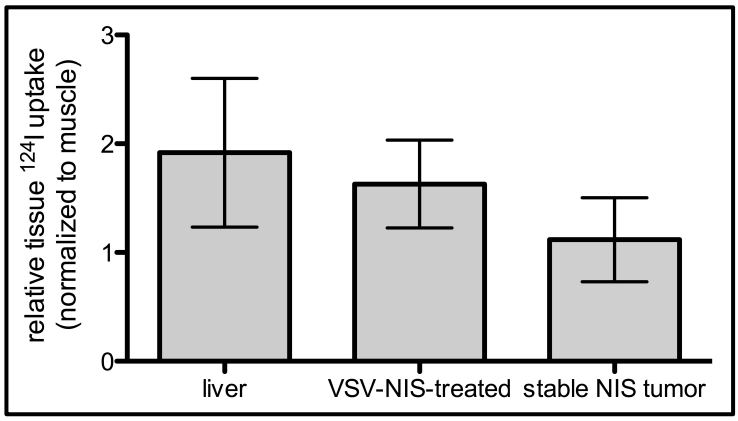

Figure 21. Quantitative analysis of ^{124}I-PET by region of interest analysis.

Results of the PET/CT imaging shown in Figure 20 have been analysed by ROI analysis. 3-dimensional ROIs were drawn manually around respective tissues. Mean uptakes of each area were normalized to muscle uptakes in each animal. Expressed are mean uptake values and SD of the respective tissue of all animals (n= 4) in a column bar graph.

4.1.1.7.2 Ex vivo validation of PET results by tracer biodistribution analysis and histology

Histological analysis of the tumors of animals sacrificed after the last scan revealed that the rNIS protein was expressed in both tumors, in the stable rNIS tumors as well as in the rVSV-rNIS-treated wt tumors (**Figure 22**).

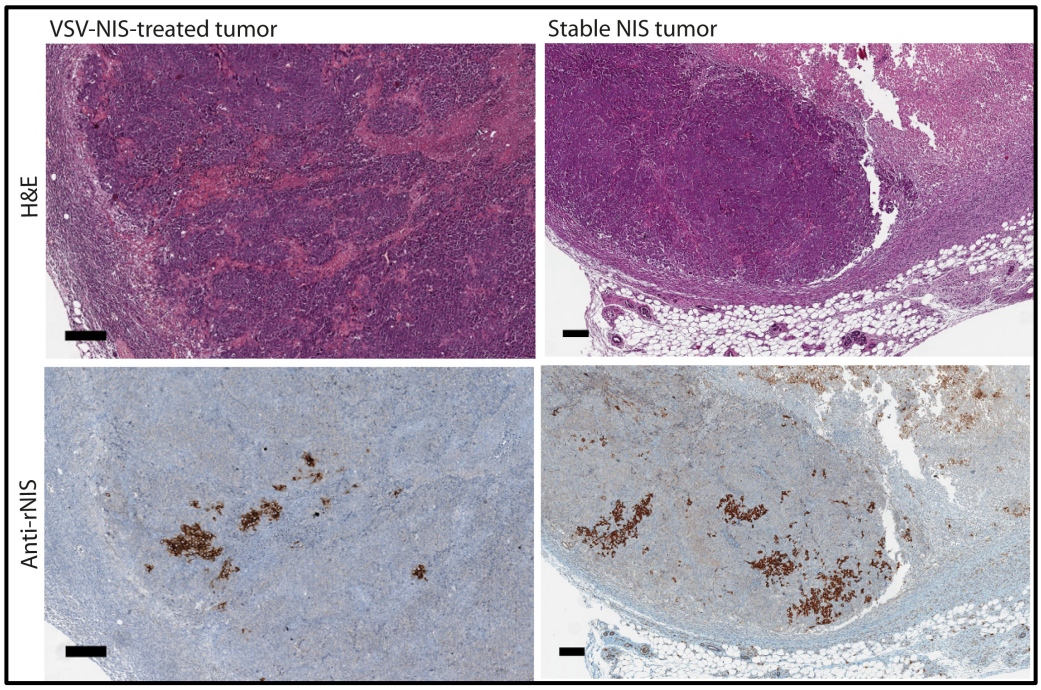

Figure 22. Histology of stable NIS tumor and rVSV-rNIS-treated tumor.

Histological analysis of tumors of a representative animal imaged by ^{124}I-PET/CT (Figure 20). Upper panel shows H&E staining and lower panel shows respective immunohistological staining against rNIS. Bar refers to 200 µm.

As an additional confirmation of the ROI analysis, the ^{124}I tracer biodistribution was detected *ex vivo* by γ-counting of the tissues of interest (Figure 23).

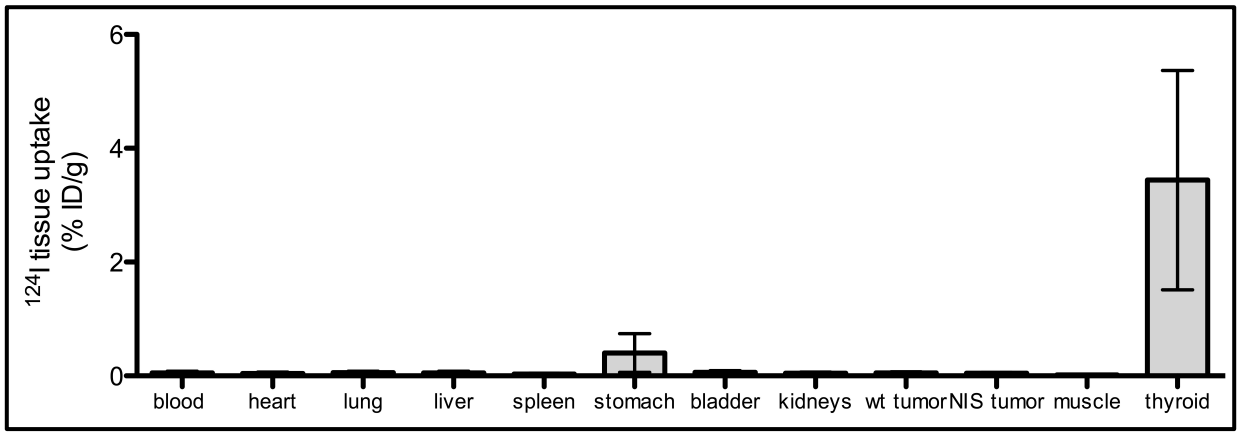

Figure 23. *Ex vivo* ^{124}I tracer biodistribution in tissues of interest.

Shown is the % of the injected tracer dose per gram of tissue (% ID/g) of different tissues. Values are expressed as mean with SD of the respective tissue of all animls (n = 4) in a column bar graph.

Tracer biodistribution confirms the quantitative ROI analysis of the PET/CT scans (Figure 21). No increase in tracer uptake could be detected in neither the rVSV-rNIS-treated wt tumors, nor in the stably rNIS expressing tumors. Increase in tracer uptakes could be detected in stomachs and thyroids (Figure 23).

4.1.2 Non-invasive *in vivo* imaging of rVSV-HSV1-sr39tk

4.1.2.1 Novel rVSV-HSV1-sr39tk could be successfully cloned and rescued

The HSV1-sr39tk gene was cloned into the pVSV plasmid and the novel rVSV-HSV1-sr39tk was rescued as described in chapter 3.2.5.1. Figure 24 depicts the resulting virus genome.

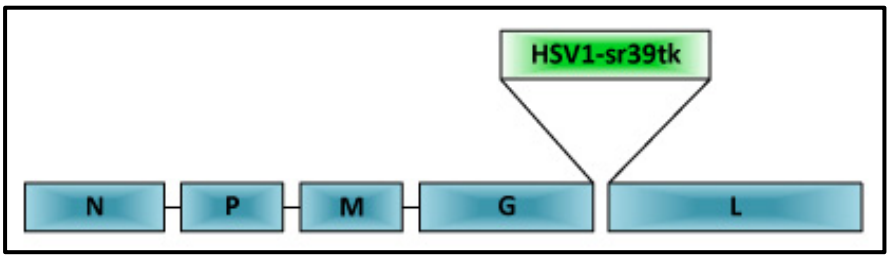

Figure 24. Schematic presentation of the genome of rVSV-HSV1-sr39tk.

The HSV1-sr39tk gene is located at position five between the G- and L-gene.

4.1.2.2 rVSV-HSV1-sr39tk is not attenuated in vitro

As a control for the growth of the novel rVSV-HSV1-sr39tk, an already established and characterized virus, rVSV-lacZ was analysed in parallel. The titers of both viruses were indistinguishable at all time points.

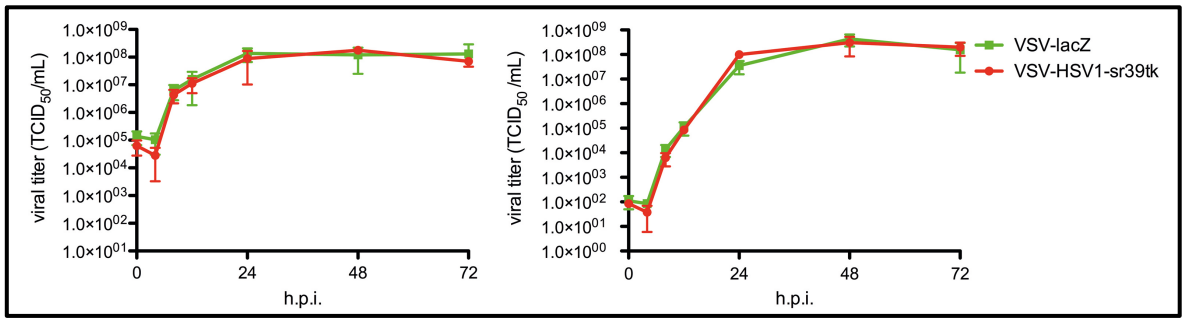

Figure 25. **One-step and multi-step growth curve of rVSV-HSV1-sr39tk.**

Viral replication of rVSV-HSV1-sr39tk (red) and rVSV-lacZ (green) was tested *in vitro* on Morris cells after an infection of MOI 10 (one-step, left panel) and MOI 0.001 (multi-step, right panel). Viral titers in the supernatant of the cell culture were analysed at various time points after infection (h.p.i. = hours post infection). All samples were performed in triplicates and values are expressed as mean with SD.

4.1.2.3 rVSV-HSV1-sr39tk does not show any restriction in its oncolytic potency

In order to test, whether the oncolytic potency is diminished in the novel recombinant virus, its cell killing ability was tested *in vitro* via a cell viability assay on Morris cells in comparison to the already characterized rVSV-lacZ.

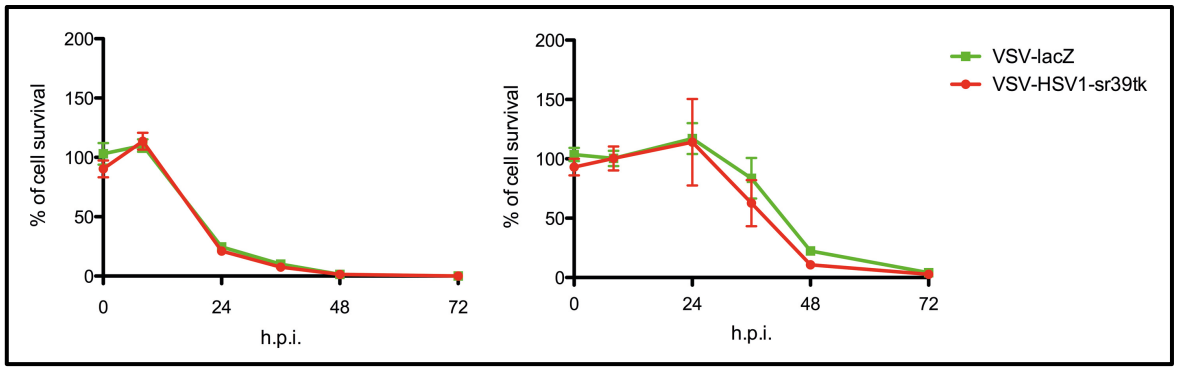

Figure 26. Survival of Morris cells after infection with rVSV-HSV1-sr39tk.

Cell survival after rVSV-HSV1-sr39tk (red) or rVSV-lacZ (green) infection was tested *in vitro* on Morris cells after an infection at MOI 10 (left panel) and MOI 0.001 (right panel). Survival of the

cells was detected at various time points after infection (h.p.i. = hours post infection) by MTS assay. All samples were performed in triplicates and values are expressed as mean with SD.

Cell survival of rat HCC cells (Morris cells) revealed no appreciable difference in the cytotoxicity of rVSV-HSV1-sr39tk as compared to the control vector (Figure 26).

4.1.2.4 Stable HSV1-sr39tk cell line and rVSV-HSV1-sr39tk-infected Morris cells express the HSV1-sr39tk protein

A stably HSV1-sr39tk-expressing Morris cell line was generated in order to establish the PET/CT imaging via the HSV1-sr39tk reporter. To confirm, that the HSV-1-sr39tk reporter enzyme is translated in VSV-HSV1-sr39tk infected cells as well as in the stably transfected cell line, the expression of the reporter protein was tested via Western Blot analysis (Figure 27) and additionally via indirect immunofluorescence microscopy (Figure 28).

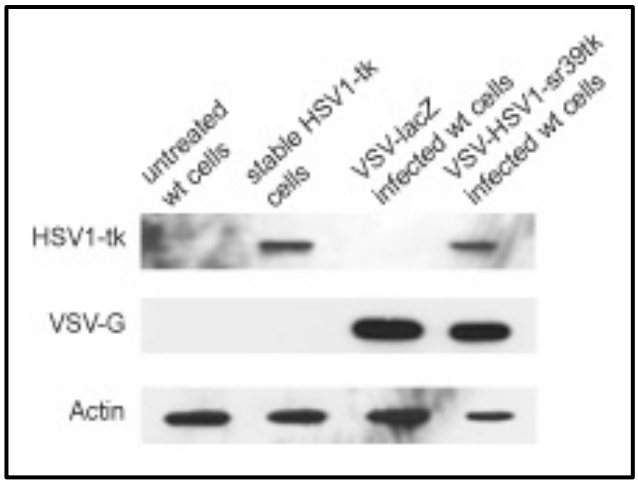

Figure 27. Western Blot analysis of whole cell lysates from Morris cells.

Western Blot of whole cell lysates of untreated wt Morris cells, stably HSV1-sr39tk-expressing Morris cells and either VSV-lacZ- or VSV-HSV1-sr39tkiinfected cells.

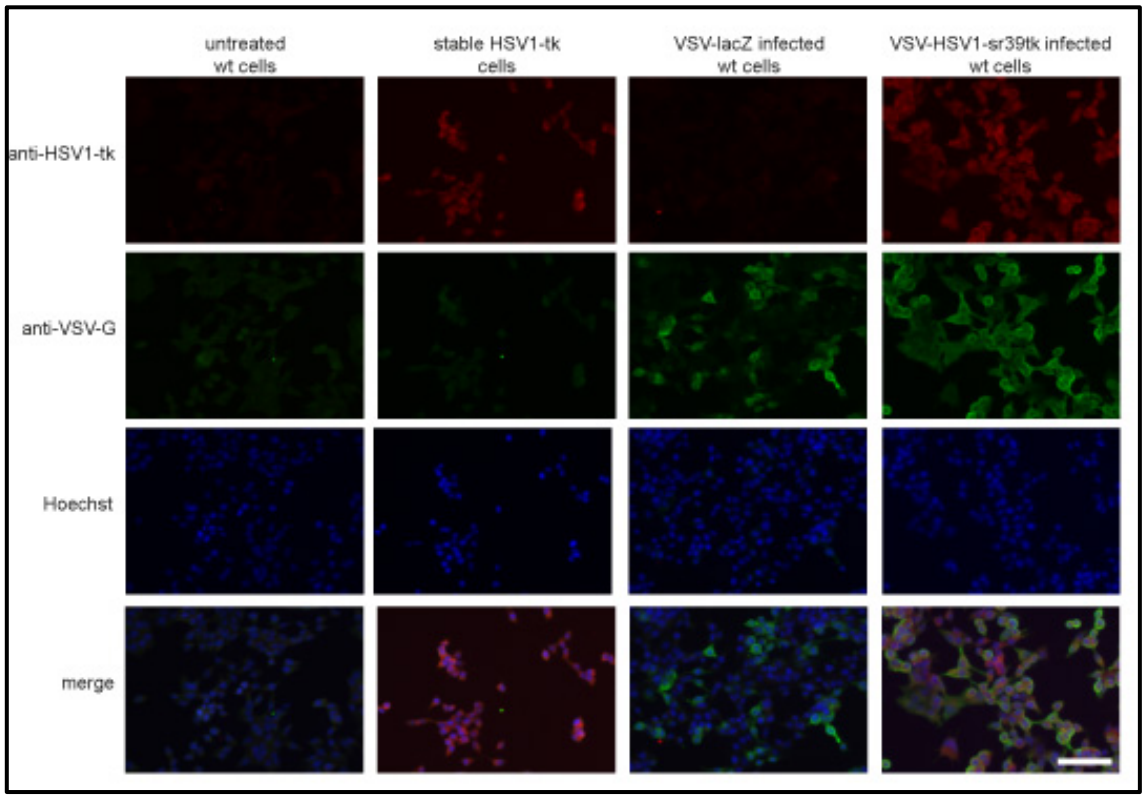

Figure 28. Indirect immunofluorescence of Morris cells.

Indirect immunofluorescence of cultured cells of untreated wt Morris cells, stably HSV1-sr39tk-expressing Morris cells and either VSV-lacZ- or VSV-HSV1-sr39tk-infected cells. Microscopy was performed at a magnification of 20x. Scale bar refers to 100 µm.

Both protein assays showed a high signal for the HSV1-tk protein in the stable cell line, as well as in the VSV-HSV1-sr39tk-infected cells. In contrast, neither in the untreated wt cell control nor in the control virus (VSV-lacZ)- infected cells HSV1-tk protein expression was be detected. Additionally, the expression of the VSV-G-protein was tested in all samples. Only the VSV infected cells showed a positive signal, while the untreated wt Morris cells as well as the stably HSV1-sr39tk-expressing Morris cell line were proven to be negative for VSV-G-expression.

4.1.2.5 Stable HSV1-sr39tk cell line and rVSV-HSV1-sr39tk-infected Morris cells show increased FHBG uptake in vitro

FHGB *in vitro* tracer uptake was performed in order to test the functionality of the HSV1-sr39tk reporter protein.

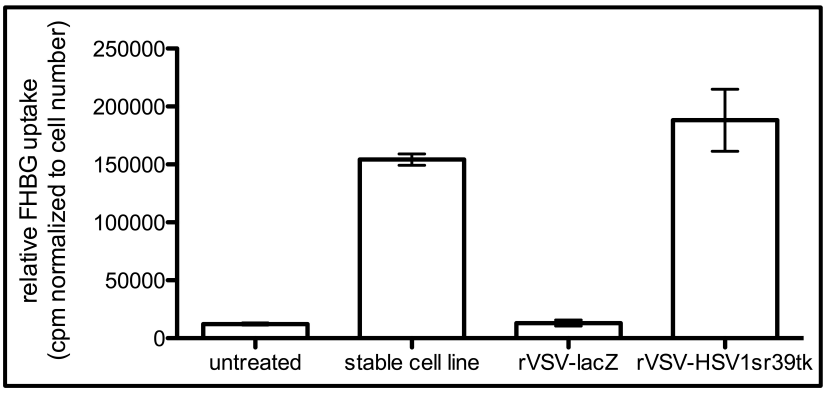

Figure 29. *In vitro* FHBG tracer uptake.

Samples were performed in triplicates and values are expressed in mean with SD in a column bar graph. Tracer uptake was normalized to the number of cells in the respective sample.

After 45 min of incubation with the FHBG tracer the untreated wt Morris cells showed a very low background uptake. In contrast, a very high tracer uptake could be detected in the stably HSV1-sr39tk-expressing cell line as well as in the rVSV-HSV1-sr39tk-infected Morris cells. Infection of wt Morris cells with rVSV-lacZ did not result in an increase of the FHBG *in vitro* tracer uptake of the cells.

4.1.2.6 Stable Morris cell line expressing HSV1-sr39tk shows high FHBG uptake in subcutaneous tumors in vivo

4.1.2.6.1 Stable HSV1-sr39tk-expressing tumors show high signals in FHBG-PET

In order to establish the PET/CT imaging and investigate the optimal amount of injected tracer and imaging timepoint, animals were implanted with two subcutaneous tumors, respectively. The stably HSV1-sr39tk-expressing Morris tumor was located on the right and wt Morris tumors on the left shoulder. PET/CT scans were performed 2 hours after tracer injection of 40 MBq FHBG. Imaging revealed a strong signal in tumors of the stable cell line, while no signal was detected in wt tumors (Figure 30).

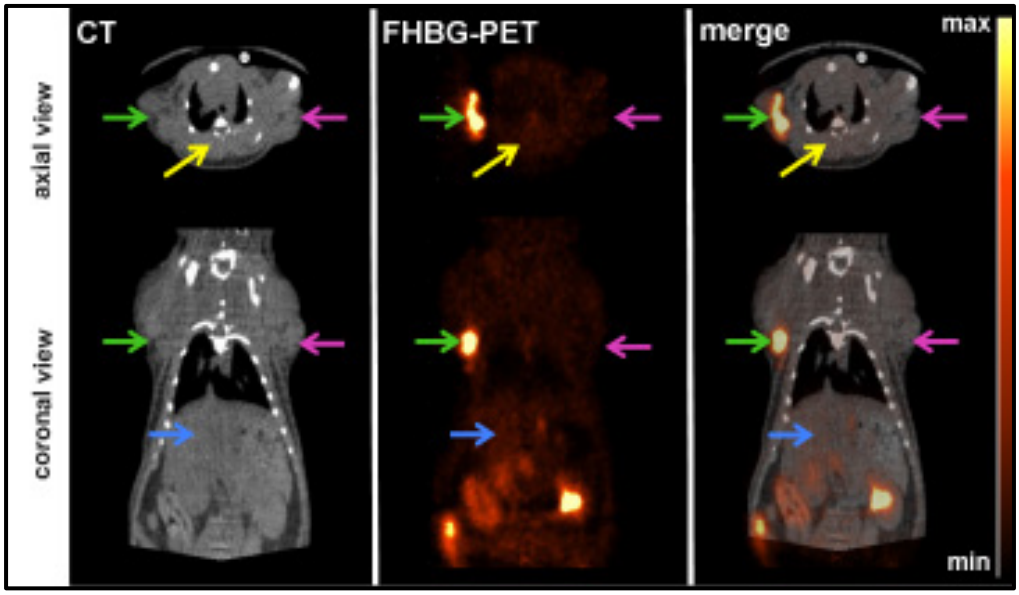

Figure 30. PET/CT of subcutaneous wt and stable HSV1-sr39tk-expressing HCC tumors in rats.

Representative scan of a rat bearing subcutaneous tumors at both flanks in axial (upper panel) and coronal (lower panel) view. Shown are the signals of low-resolution, native CT and PET separately, as well as a merged image of both signals. Arrows indicate the tumors (green: stable HSV1-sr39tk-expressing tumor; magenta: wt tumor), the liver (blue arrow) and the spinal muscle (yellow arrow). PET intensity scale is set to 3 x 10^5 Bq/mL at maximum value and 0 Bq/mL at minimum value.

A high FHBG tracer uptake in the stable HSV1-sr39tk-expressing tumors compared to liver was shown by quantitative ROI analysis, while the wt tumors showed no increase in tracer uptake in comparison to the liver background (Figure 31).

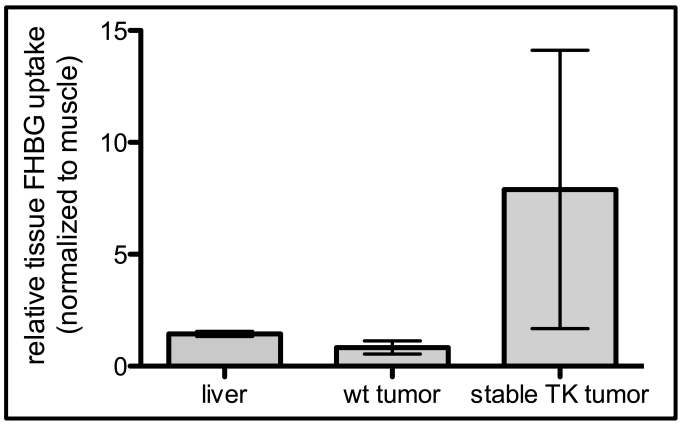

Figure 31. Quantitative analysis of tissue tracer uptakes from FHBG-PET.

Quantitative analysis of tracer accumulation in regions of interest (ROI) from PET/CT scans. Results of the PET/CT imaging shown in Figure 30 were analysed by ROI analysis. 3-dimensional ROIs were drawn manually around respective tissues. Expressed are means and SD of all animals (n= 4) in a column bar graph.

4.1.2.6.2 Ex vivo validation of HSV1-sr39tk proof of principle PET results

The *in vivo* results received by PET/CT imaging were validated by *ex vivo* analysis. For this, *ex vivo* autoradiography was performed on tissue slices of both tumors, liver and muscle tissue (Figure 32).

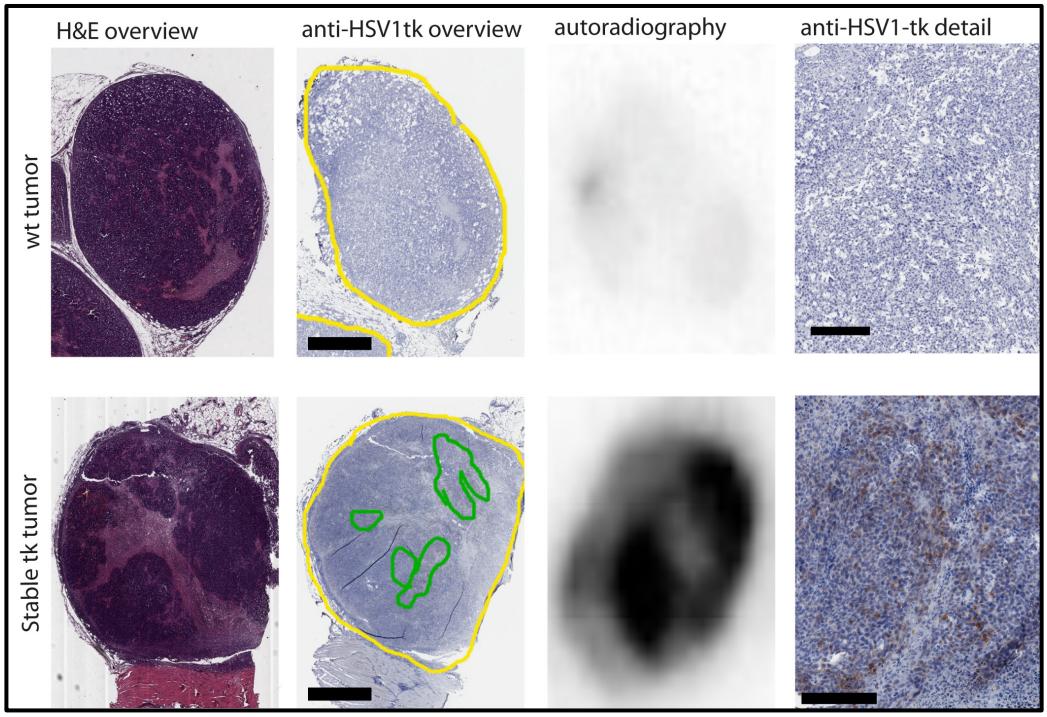

Figure 32. *Ex vivo* analysis of tumor sections.

Histological analysis of subcutaneous tumors of a representative animal imaged by ^{18}F-FHBG-PET/CT (Figure 30). Upper panel shows the wt tumor and lower panel the stably HSV1-sr39tk-expressing tumor of the same animal. From left to right: H&E-stained overview, anti-HSV1&2-tk-stained overview (tumor encircled in yellow, areas of high HSV1&2-tk signal encircled in green), and autoradiogram of the same slice, followed by a detailed image of the anti-HSV1&2-tk-stained tumor section.

Autoradiogram indicates areas of high signal by darker color, while lower intensities are indicated by lighter staining. Bars refer to 2 mm (overview) and 200 µm (detail).

No expression of HSV1-tk was detected in the wt tumors, while the stable tumors showed high signals of HSV1-tk expression. Additionally, only a low background uptake of FHBG can be seen in the tissue autoradiography of the wt tumors, while a very strong signal is detected in the stable tumors (Figure 32).

Autoradiography data of these tissues was analyzed quantitatively to determine the FHBG tracer uptake. A high uptake was detected in the stable tumors, while

the wt tumors showed no appreciable uptake compared to the background uptake by the liver (Figure 33).

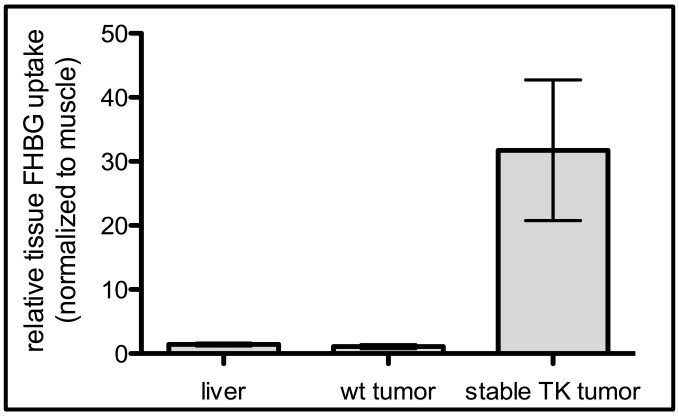

Figure 33. Quantitative analysis of tissue tracer uptakes from *ex vivo* autoradiography.

Quantitative analysis of tracer accumulation in tissues of interest from *ex vivo* autoradiography analysis, shown in Figure 32. Expressed are the means and SD of all values of n = 4 animals in a column bar graph.

Additionally, the biodistribution of the FHBG tracer was analysed *ex vivo* in the tissues of interest. Animals were dissected after the last image acquisition and γ-counting was performed to measure tracer accumulation (Figure 34).

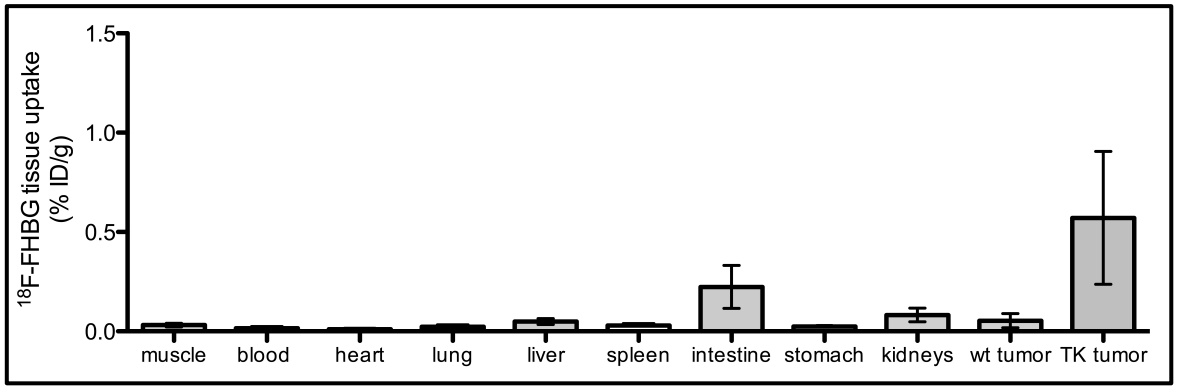

Figure 34. *Ex vivo* FHBG tracer biodistribution in tissues of interest.

Shown is the % of the injected tracer dose per gram of tissue (% ID/g) of respective tissue. Values are represented as mean with SD (n = 4) in a column bar graph.

Both *ex vivo* assays confirmed the finding from the PET/CT *in vivo* images. Only

the stably HSV1-sr39tk-expressing tumors showed increased tracer uptake, while no increase was detected in the wt tumors. Low background uptake levels were detected for the liver tissue.

4.1.2.7 rVSV-HSV1-sr39tk-treated orthotopic HCC tumors show high FHBG uptake in vivo

4.1.2.7.1 HSV1-sr39tk-treated tumors show high signals in FHBG-PET

In order to validate the applicability of the VSV-HSV1-sr39tk system in orthotopic liver tumors, orthotopic wt liver tumors bearing animals were injected intratumorally with either PBS, rVSV-lacZ control virus or rVSV-HSV1-sr39tk (1x 10^7 pfu in 100 µL total volume, respectively). On day 1 after treatment FHBG-PET/CT was performed. No signal was detected in PBS or rVSV-lacZ-treated, while high tracer uptakes were shown in positive control animals implanted with stably HSV1-sr39tk-expressing tumors as well as in rVSV-HSV1-sr39tk-treated animals (Figure 35).

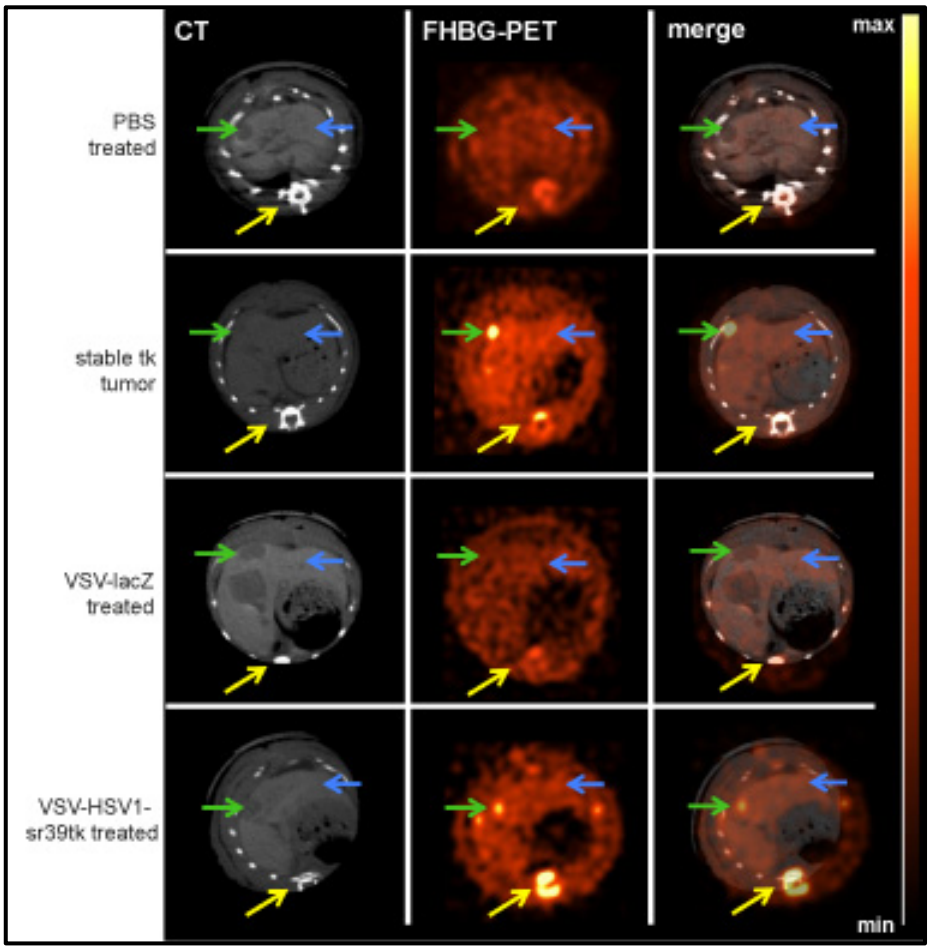

Figure 35. PET/CT images of FHBG-PET scans of rats bearing orthotopic HCC.

Representative scans of rats bearing orthotopic HCCs in axial view. Shown is one representative example of every treatment group in high resolution, contrast-enhanced CT, PET and merged signal. Arrows indicate the tumor (green), the liver (blue) and the spinal muscle (yellow), respectively. PET intensity scale is set to 3 x 10^4 Bq/mL at maximum value and 0 Bq/mL at minimum value.

Quantitative ROI analysis revealed increased tracer uptakes in the tumors of the stable HSV1-sr39tk-expressing positive control group as well as in the VSV-sr39tk-treated group, compared to the FHBG uptake level in the liver (Figure 36).

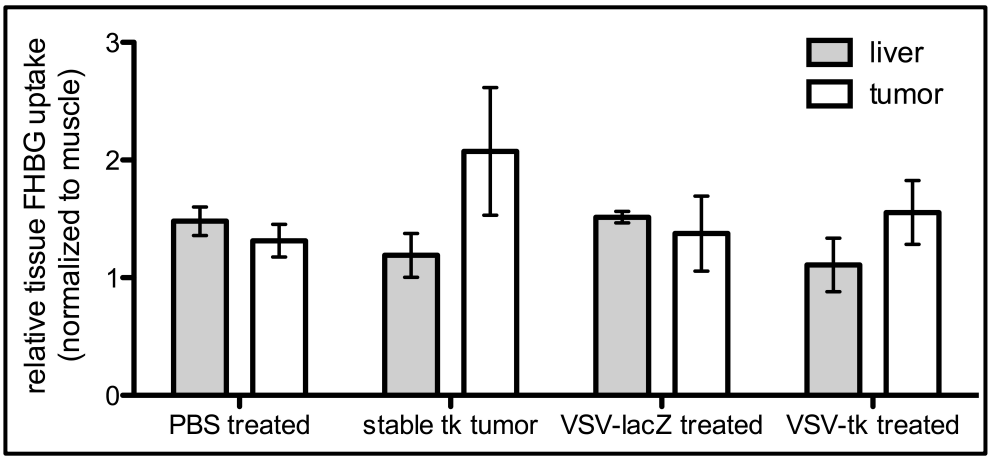

Figure 36. Quantitative ROI analysis of tissue tracer uptakes from *in vivo* FHBG-PET.

Quantitative analysis of tracer accumulation in regions of interest (ROI) from PET/CT scans. Expressed are mean and SD of each treatment group (PBS n= 4, stable tk tumor n= 3, VSV-lacZ-treated n= 2, VSV-HSV1-sr39tk-treated n= 6) in a column bar graph.

In order to understand the signal-to-noise ratio better, tumor-to-liver ratios of all animals were calculated and graphically expressed (Figure 37**).**

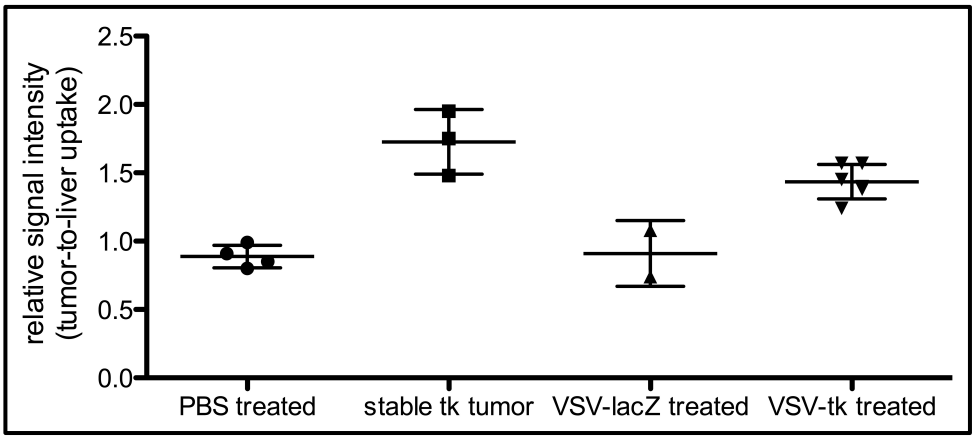

Figure 37. Relative signal intensity of the FHBG signal in the tumor from *in vivo* FHBG-PET.

Relative signal intensity of the tumor-to-liver signal of the groups shown in **Figure 36**. The tumor signal of each animal was divided by the liver signal of the respective animal. Expressed are mean and SD of each treatment group in a scatter plot.

The tumor:liver signal in PBS- and VSV-lacZ-treated animals is at the same level, while animal treated with VSV-HSV1-sr39tk or bearing stable tk tumors show a high increase in tumor:liver ratios.

4.1.2.7.2 Ex vivo validation of PET results by autoradiography and histology

Ex vivo autoradiography was performed in order to check the reliability of the values generated by quantitative ROI analysis. Regions of reporter protein expression identified by histology could be co-localized with those areas, showing high FHBG signals, in the autoradiography (Figure 38). No HSV1-tk expression could be detected in neither the PBS- nor the rVSV-lacZ-treated tumors correlating with no or only very weak background radiation in these tumors.

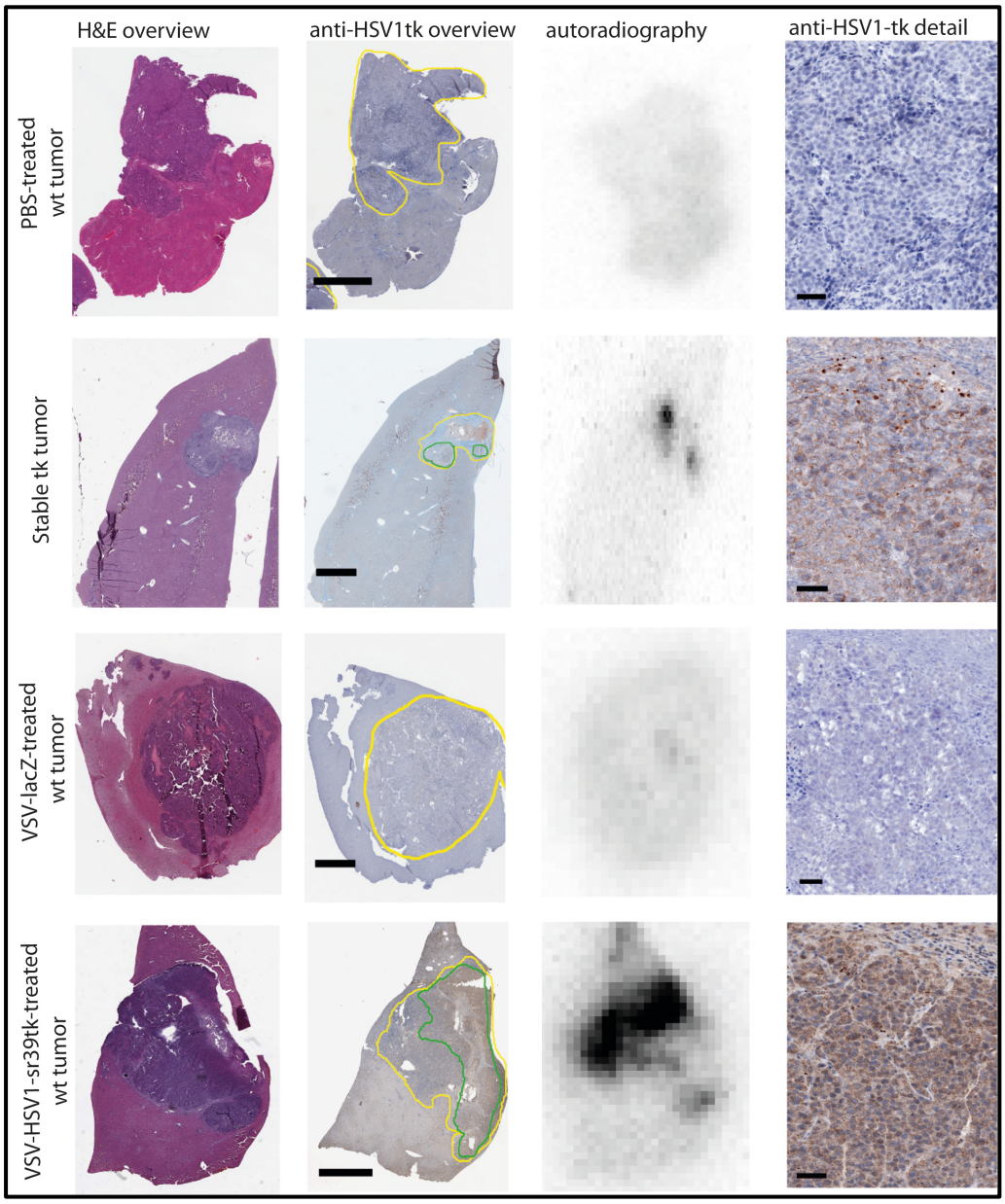

Figure 38. *Ex vivo* autoradiography of tumor tissues and corresponding histology.

Histological analysis of orthotopic HCC lesions of one representative animal of each group imaged by ^{18}F-FHBG-PET/CT (Figure 35). . From left to right: H&E-stained overview, anti-HSV1&2-tk-stained overview (tumor encircled in yellow, areas of high HSV1&2-tk signal encircled in green), and autoradiogram of the same slice, followed by a detailed image of the anti-HSV1&2-tk-stained tumor section.

Autoradiogram indicates areas of high signal by darker color, while lower intensities are indicated by lighter staining. Bars refer to 2 mm (overview) and 50 µm (detail).

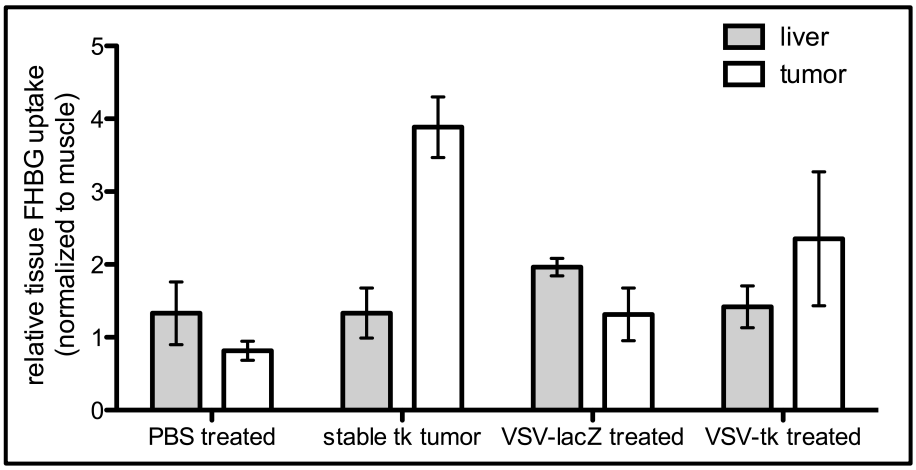

Figure 39. Quantitative analysis of tissue tracer uptakes from *ex vivo* autoradiography.

Quantitative analysis of tracer accumulation in tissues of interest from *ex vivo* autoradiography analysis. Expressed are mean and SD of each treatment group (PBS n= 4, stable tk tumor n= 3, VSV-lacZ-treated n= 2, VSV-HSV1-sr39tk-treated n= 6) in a column bar graph.

In order to understand the signal-to-noise ratio better, tumor-to-liver ratios of all animals were calculated and graphically expressed (Figure 40**).**

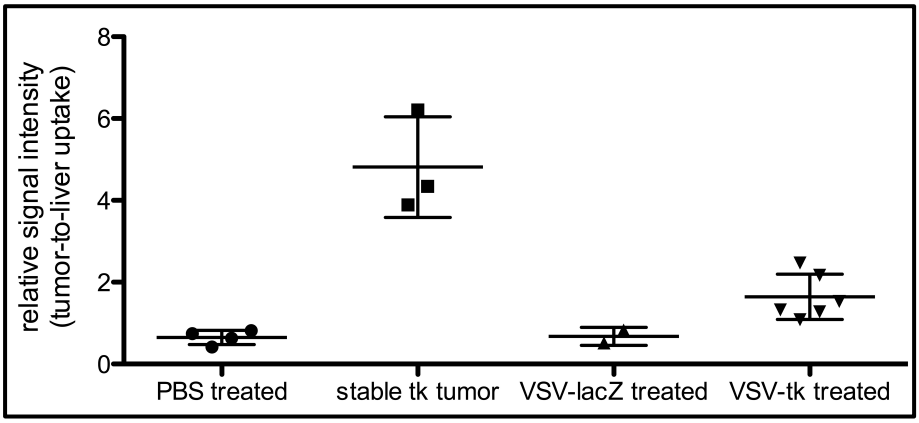

Figure 40. Relative signal intensity of the FHBG signal in the tumor from *ex vivo* autoradiography.

Relative signal intensity of the tumor-to-liver of the groups shown in **Figure 39**. The tumor signal of each animal was divided to by the liver signal of the respective animal. Expressed are mean and SD of each treatment group in a scatter plot.

As already described by the quantitative ROI analysis also the *ex vivo* autoradiography showed that the tumor:liver signal in PBS- and VSV-lacZ-treated animals is at the same level, while animal treated with VSV-HSV1-sr39tk or bearing stable tk tumors show a high increase in tumor:liver ratios. The signal distribution pattern generated by PET analysis (Figure 36) could be confirmed by the quantitative analysis of *ex vivo* autoradiography (Figure 39).

4.1.2.7.3 Ex vivo tracer FHBG biodistribution

Tissues of interest were analysed by γ-counting in order to monitor the tracer biodistributions and its suitability for the *in vivo* application.It was not possible to include tumor tissues for the *ex vivo* biodistribution studies due to unfortunate logistics.

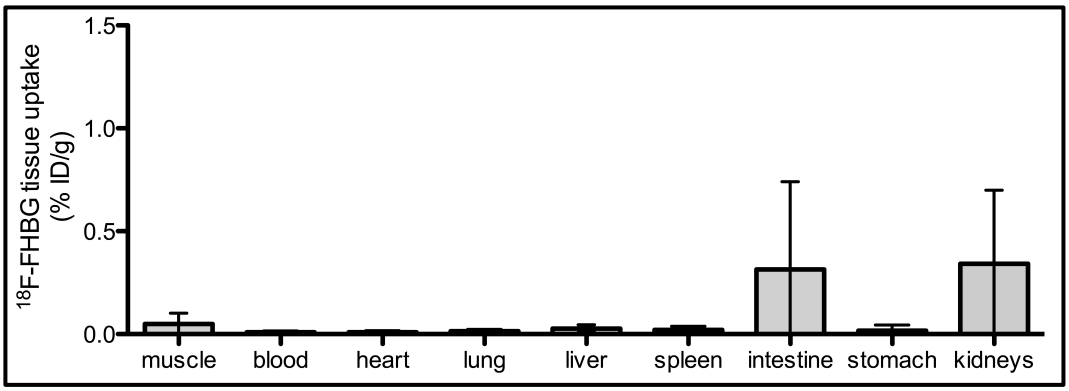

Figure 41. *Ex vivo* FHBG tracer biodistribution in tissues of interest.

Shown is the % of the injected tracer dose per gram of tissue (% ID/g) of respective tissue. Values are represented as mean with SD (n = 15) in a column bar graph.

The FHBG shows a very low background uptake in the liver and some accumulation in the intestine and kidneys, which is negligible (Figure 41).

4.1.2.8 The detection limit of rVSV-HSV1-sr39tk by PET is defined at 1x 10^6 pfu after intratumoral injection

To determine the detection limit of the minimal injected viral dose a dose decrement study was performed. Therefore, rats, bearing orthotopic liver tumors, were injected intratumorally with either PBS or four different, log-wise increasing doses of VSV-HSV1-sr39tk starting at 1x 10^4 pfu. FHBG-PET/CT was performed on day 1 after treatment (Figure 42).

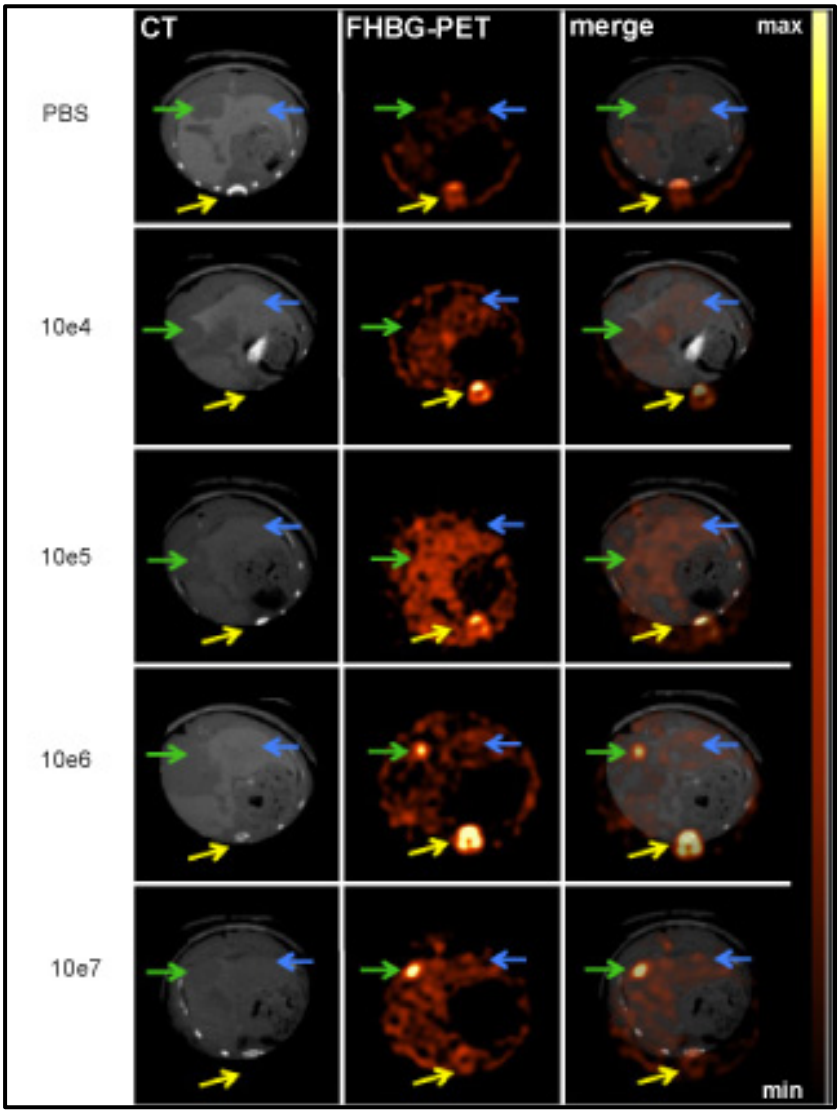

Figure 42. FHBG-PET/CT images of rats bearing orthotopic HCC treated with different doses of rVSV-HSV-sr39tk.

Representative scans of rats bearing orthotopic HCCs in axial view. Shown is one representative example of every dose group. From left to right: high resolution, contrast-

enhanced CT, FHBG-PET and merged signal. Arrows indicate the tumor (green), the liver (blue) and the spinal muscle (yellow), respectively. PET intensity scale is set to 2 x 10^4 Bq/mL at maximum value and 5 x 10^3 Bq/mL at minimum value.

PET/CT revealed signals in the tumors of those groups treated with rVSV-HSV1-sr39tk at doses of 1x 10^6 and 1x 10^7 pfu, while no signals could be detected in groups of 10^4 or 10^5 VSV-HSV1-sr39tk injected viral dose (Figure 42).

Quantitative PET analysis showed that tracer uptake was strongly increased in tumors which received a viral dose of 1x 10^6 pfu or 1x 10^7 pfu on day 1 after treatment (Figure 43).

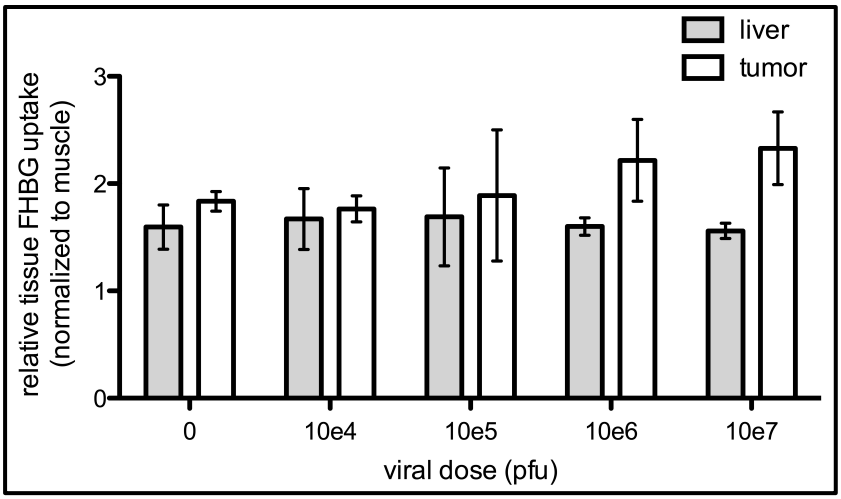

Figure 43. Quantitative ROI analysis of tissue tracer uptakes from *in vivo* FHBG-PET.

Quantitative analysis of tracer accumulation in regions of interest (ROI) from PET/CT scans. Expressed are mean and SD of each treatment group (PBS: n= 2, 1x 10^4: n= 2, 1x 10^5: n= 4, 1x 10^6: n= 3, 1x 10^7: n= 2) in a column bar graph.

In order to understand the signal-to-noise ratio better, tumor-to-liver ratios of all animals were calculated and graphically expressed (Figure 44**).**

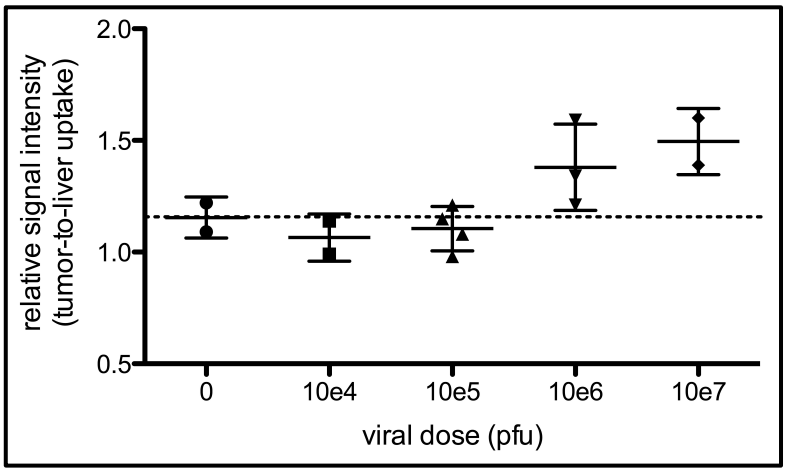

Figure 44. Relative signal intensity of the FHBG signal in the tumor from *in vivo* FHBG-PET.

Relative signal intensity of the tumor-to-liver of the groups shown in **Figure 43**. The tumor signal of each animal was divided to by the liver signal of the respective animal. Expressed are mean and SD of each treatment group in a scatter plot. Dotted line indicates background signal defined by the mean of the PBS-treated group (i.e. 1.16).

The signal-to-noise analysis revealed a mean of the PBS-treated group at tumor:liver at 1.16. This value was set as the background tracer signal in the tumor. Groups treated with a dose of 1x 10^4 or 1x 10^5 pfu showed signals below this threshold, while groups treated with either 1x 10^6 or 1x 10^7 pfu VSV-HSV1-sr39tk revealed increased levels of tracer uptake. The animals of the groups with elevated uptake levels were analysed for the goodness of fit of tumor-to-liver ratios to intratumoral titer. A correlation was shown with R^2 = 0.6653 (Figure 45).

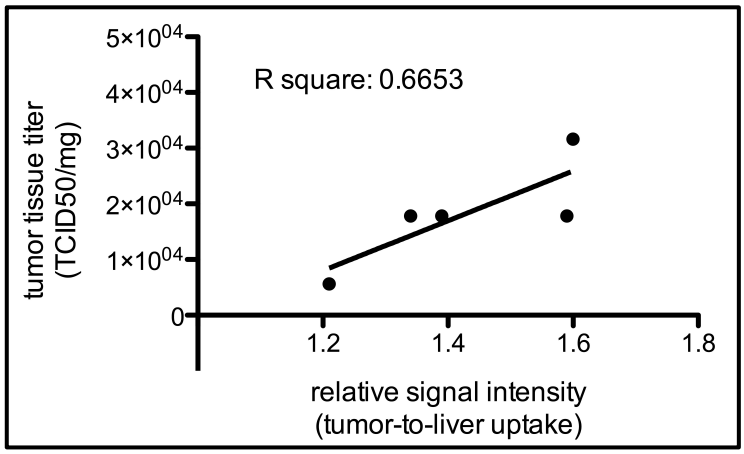

Figure 45. Goodness of fit analysis for correlation of intratumoral VSV titers to PET tumor-to-liver ratios

Analysis of correlation of tumor-to-liver ratio of the FHBG-PET signal to intratumoral virus titers ($TCID_{50}$/mg). The mean of the PBS-treated group (i.e. 1.16) was set as signal background. Only animals of groups, which showed increased tumor-to-liver ratios above the background (i.e. doses 1x 10^6 and 1x 10^7,Figure 44), were analyzed for correlation. Goodness of fit could be shown at R square = 0.6653.

4.1.2.9 rVSV-HSV1-sr39tk kinetic by PET

To investigate the kinetics of VSV-mediated HSV1-sr39tk imaging and to test thepossibility of monitoring rVSV-HSV1-sr39tk replication, animals were treated intratumorally with 1 x 10^7 pfu VSV-HSV1-sr39tk and FHBG-PET was applied at various time points after treatment (Figure 46).

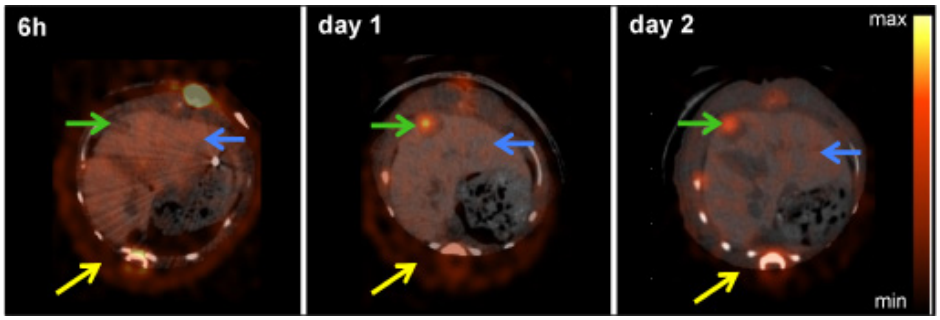

Figure 46. PET/CT scan of the HCC-bearing animals rats at various time points after rVSV-HSV1-sr39tk treatment.

Representative scans of rats bearing orthotopic HCCs in axial view. Shown is one representative example of every group in a merged image of high resolution, contrast-enhanced CT and PET signal. Arrows indicate the tumor (green), the liver (blue) and the spinal muscle (yellow), respectively. PET intensity scale is set to 2 x 10^4 Bq/mL at maximum value and 0 Bq/mL at minimum value.

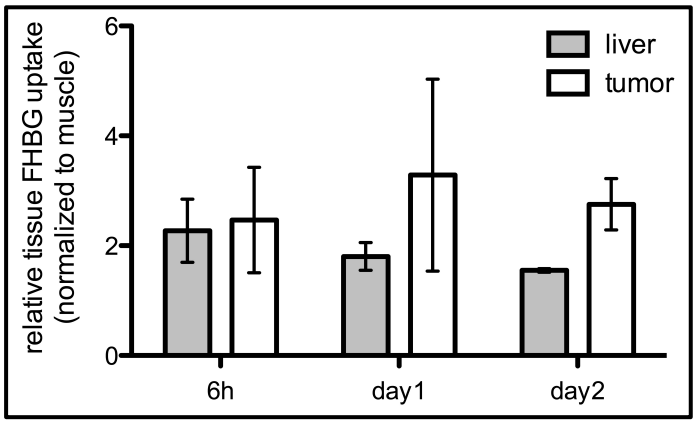

Figure 47. Quantitative ROI analysis of tissue tracer uptakes from *in vivo* FHBG-PET.

Quantitative analysis of tracer accumulation in regions of interest (ROI) from PET/CT scans. Expressed are mean and SD of each group (6h n= 7; day1 n= 5; day2 n= 3) in a column bar graph.

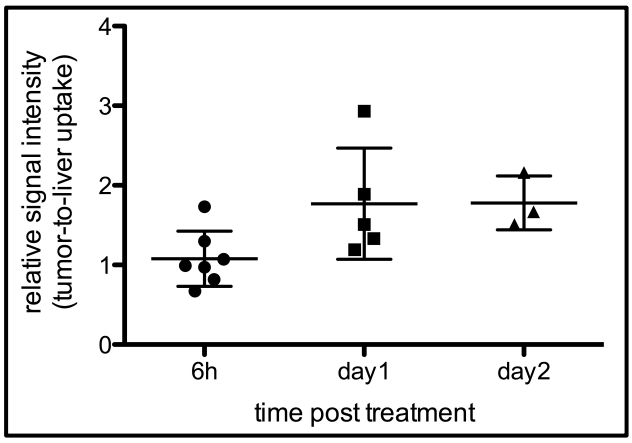

Figure 48. Relative signal intensity of the FHBG signal in the tumor from *in vivo* FHBG-PET.

Relative signal intensity of the tumor-to-liver of the groups shown in **Figure 47**. The tumor signal of each animal was divided by the liver signal of the respective animal. Expressed are mean and SD of each group in a scatter plot.

Quantitative ROI analysis revealed no specific tracer uptakes of the tumors 6 h after the rVSV-HSV1-sr39tk-treatment (tumor:liver at 1.07). A strong increase in tracer uptake in the tumors was detected on day 1 after treatment, which was still visible at the same level on day 2 (Figure 47).

4.2 Response imaging

In order to identify a PET tracer suitable for imaging specific tumor responses of HCC to VSV therapy, different established PET response tracers were screened.

4.2.1 ^{18}F-FDG PET

FDG, as the most prominent PET response tracer, was the first tracer tested for its suitability. Therefore, orthotopic HCC-bearing rats were injected with 20 MBq ^{18}F-FDG intraveniously into the tail vein. Static PET acquisition was performed 45 min after tracer application. Animals were allowed to wake up in between tracer application and image acquisition.

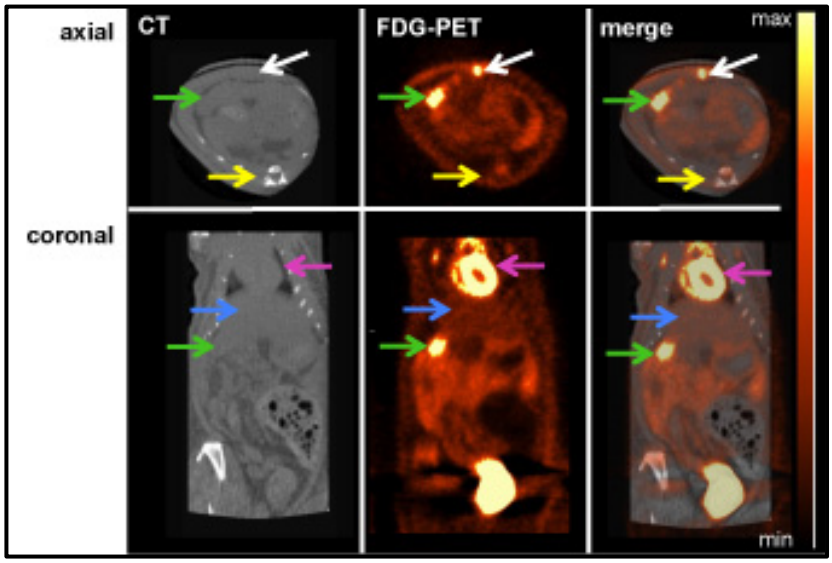

Figure 49. FDG-PET/CT scan of an orthotopic HCC-bearing rat.

Representative scans of a rat bearing orthotopic HCC (n = 4) in axial view (upper panel) and coronal view (lower panel). Arrows indicate the tumor (green), the liver (blue) spinal muscle (yellow), surgery scar (white) and the heart (magenta), respectively. PET intensity scale is set to 2 x 10^5 Bq/mL at maximum value and 0 Bq/mL at minimum value. Native CT scans were performed at low resolution.

FDG-PET showed a specific tracer uptake in all tumors. Additionally, the characteristic FDG uptake of the heart could be seen. Strong signals were monitored in scar tissues (Figure 49).

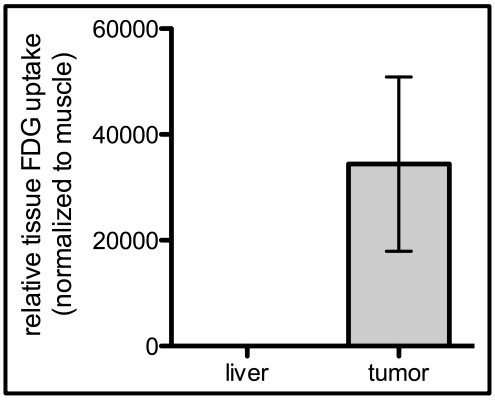

Figure 50. Quantitative ROI analysis of tissue tracer uptakes from *in vivo* FDG-PET.

Quantitative analysis of tracer accumulation in regions of interest (ROI) from PET/CT scans shown in Figure 49. Values are expressed as mean and SEM (n= 4) in a column bar graph.

4.2.2 ^{18}F-FET PET

One day after the FDG-PET/CT scans, the same animals were scanned in FET-PET/CT. Analysis of the PET and CT images revealed no specific tracer accumulation in the tumor. The side signal in the PET scans, which can be seen in axial view, is co-located with the spleen and was detected in all animals.

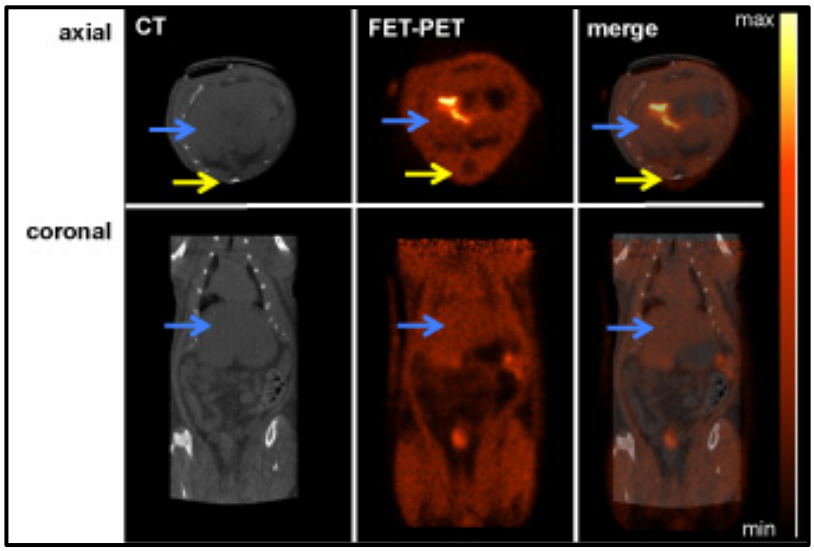

Figure 51. FET-PET/CT scan of an orthotopic HCC-bearing rat.

Representative scan of a rat bearing orthotopic HCC (n = 4) in axial view (upper panel) and coronal view (lower panel). Arrows indicate the liver (blue) and the spinal muscle (yellow), respectively. PET intensity scale is set to 3 x 10^5 Bq/mL at maximum value and 0 Bq/mL at minimum value. Native CT was performed at low resolution.

4.2.3 ^{18}F-FLT PET

Another candidate previously reported as a promising tracer for the detection of HCC is FLT. FLT was screened in untreated, orthotopic HCC-bearing rats. Therefore, the FLT tracer was injected and 15 min static acquisition was performed 45 min after tracer application.

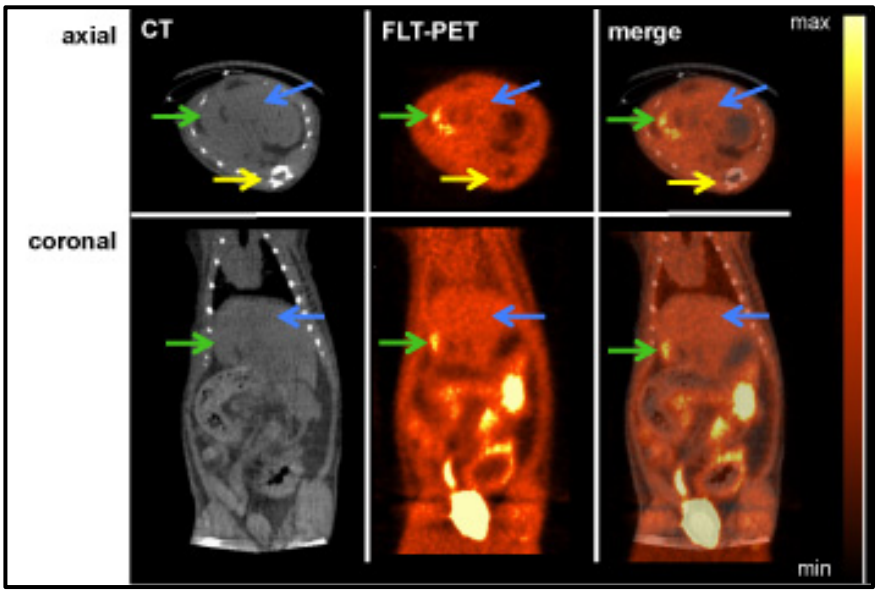

Figure 52. ^{18}F-FLT-PET/CT scan of untreated orthotopic HCC-bearing rats.

Representative scan of a rat bearing orthotopic HCC (n = 3) in axial view (upper panel) and coronal view (lower panel). Arrows indicate the tumor (green), the liver (blue) and the spinal muscle (yellow), respectively. PET intensity scale is set to 2 x 10^5 Bq/mL at maximum value and 0 Bq/mL at minimum value. Native CT was performed at low resolution.

FLT imaging revealed a specific uptake in all tumors as shown in Figure 52 with slightly increased tracer uptakes in the tumors compared to the liver background (Figure 53).

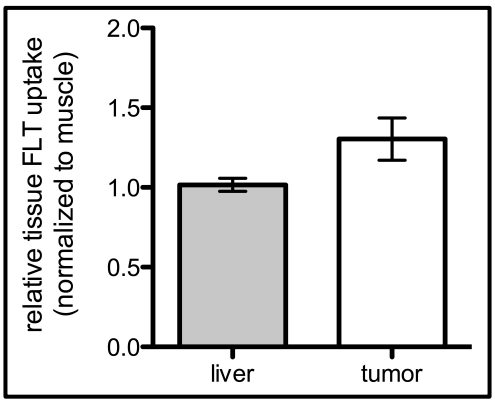

Figure 53. Quantitative ROI analysis of tissue tracer uptakes from *in vivo* FLT-PET.

Quantitative analysis of tracer accumulation in regions of interest (ROI) from PET/CT scans shown in Figure 52. Values are expressed as mean and SD (n= 3) in a column bar graph.

In order to optimize the tumor:ratios, a dynamic scan was performed in one rat to determine the optimal time point for the image acquisition after tracer injection. 20 MBq ^{18}F-FLT were applied to an orthotopic HCC-bearing rat. Imaging was performed from the time point of injection up to 115 min after tracer application.

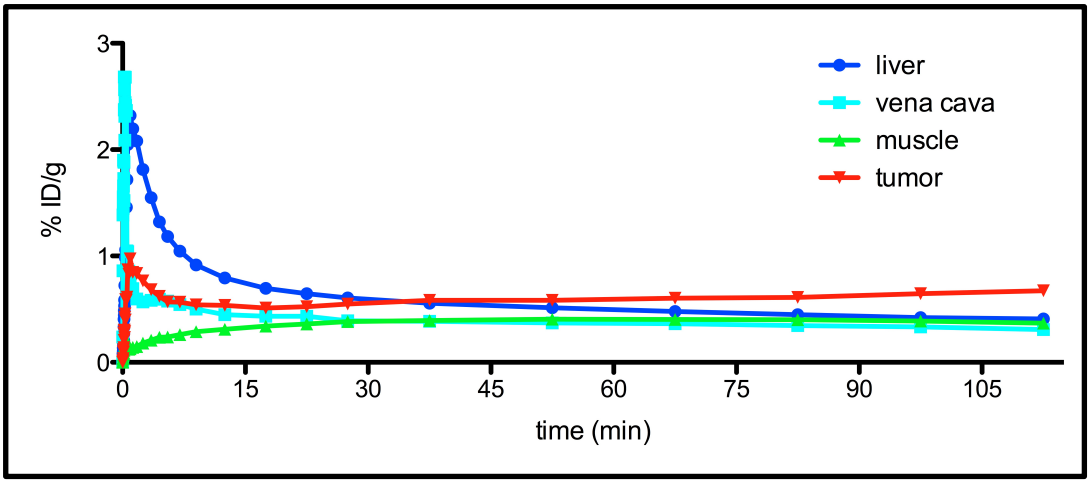

Figure 54. ^{18}F-FLT time activity curve in an HCC-bearing rat.

Time activity curve (TAC) of FLT in different tissues of interest after intravenious on bed-injection into the tail vein. Dynamic imaging has been performed over 115 min. Region of interests (ROIs) were drawn manually around tissues of interest and the FLT tracer accumulation was detected over time and is expressed in % of injected dose per gram (% ID/g) at each time point.

Dynamic scanning revealed the optimal time point for the static acquisition at 105 min after FLT i.v. administration. At this time point, the tumor to liver ratio of the FLT signal is at 1.66. In contrast, a tumor:liver ratio of only 1.3 was detected 45 min after tracer application. Therefore, the time point of the static imaging of FLT-PET was changed to a 15 min acquisition from 105 to 120 min after tracer injection.

In a next attempt, the changes in the FLT uptake of HCC treated with PBS- versus VSV-treated lesions pre and post therapy were tested. Orthotopic HCC-bearing rats were scanned by FLT-PET/CT one day before and one day after intra-arterial treatment.

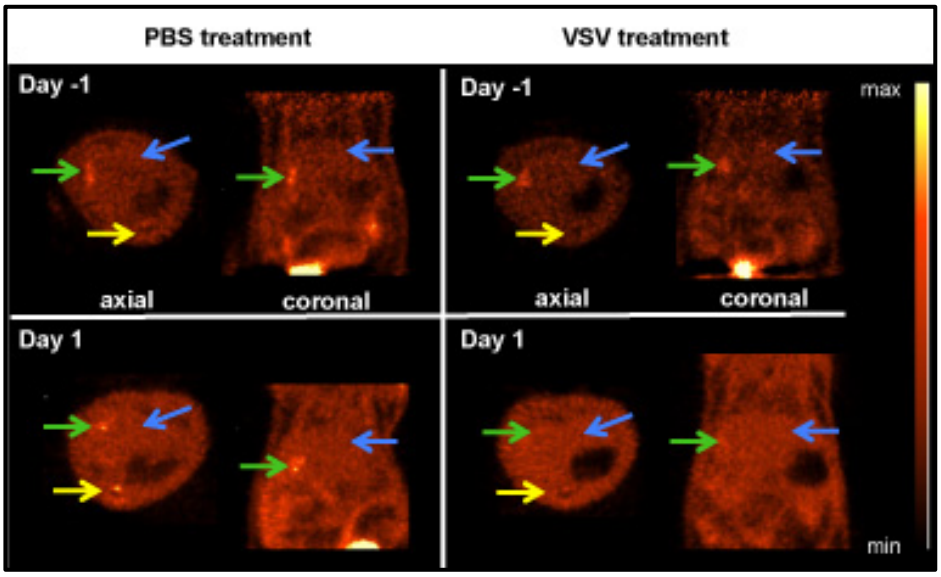

Figure 55. ^{18}F-FLT-PET scan of orthotopic HCC-bearing rats pre and post VSV treatment.

Representative scan of a rat bearing orthotopic HCC one day before (upper panel) and after (lower panel) intra-arterial treatment of either PBS (left side) or 1 x 10^7 rVSV-NIS (right side) in axial and coronal view. Arrows indicate the tumor (green), the liver (blue) and the spinal muscle (yellow), respectively. PET intensity scale is set to 2 x 10^5 Bq/mL at maximum value and 0 Bq/mL at minimum value. Native CT was performed at low resolution.

Quantitative ROI analysis revealed an interesting trend in tracer uptake values in PBS- versus VSV-treated tumors, indicating a reduction in the FLT signal in VSV-treated tumors, which was not detected in the PBS-treated group (Figure 56).

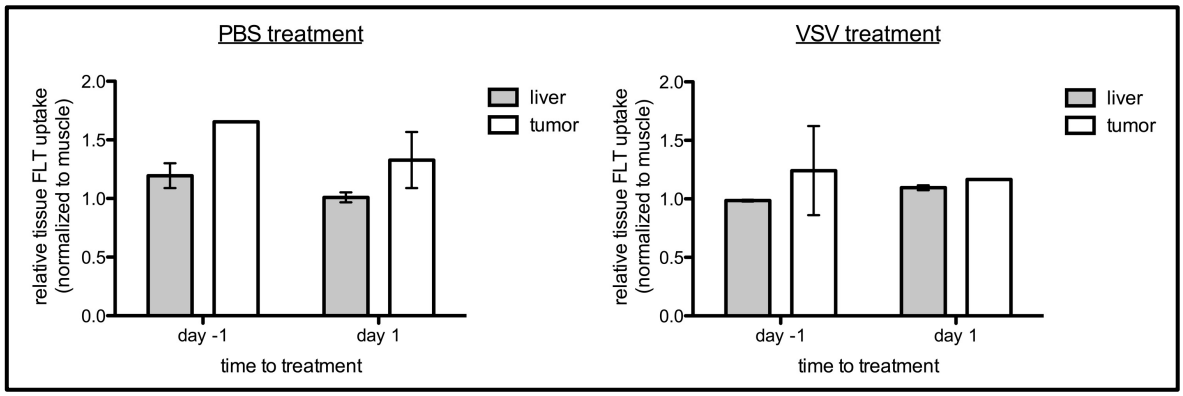

Figure 56. Quantitative ROI analysis of tissue tracer uptakes from *in vivo* FLT-PET before and after treatment.

Quantitative analysis of tracer accumulation in regions of interest (ROI) from PET/CT scans shown in Figure 55. Values are expressed as mean and SD (n= 2) in a column bar graph.

5 DISCUSSION

5.1 Virus imaging

Over the last decade, substantial progress in the field of oncolytic virus development has enabled the clinical translation of OV therapy to become a reality. In light of this development, the clinical need for an accurate, sensitive, and reproducible method of non-invasively imaging the virus after application to patients has become evident. Such a system would allow clinicians to determine virus replication and biodistribution in real-time to predict the efficacy of the therapy, as well as to monitor safety, and offer the possibility of providing personalized medicine, such that the course of therapy could be altered based on imaging findings. However, non-invasive imaging of replicating viruses in vivo presents a unique set of challenges. Since lysis of cancerous cells occurs rapidly after infection, the time frame, in which the expression of a reporter protein can be exploited for imaging, is very limited. Due to innate differences in the replication kinetics of each vector platform, as well as the time-course of reporter protein expression versus half-life, the optimal time-point for detection of virus-mediated reporter expression needs to be determined individually for each vector and reporter system.

To date, numerous reports have described non-invasive imaging of oncolytic viruses *in vivo* [90, 97, 98]; however, to our knowledge, there has been no account of virus imaging in an orthotopic and immune-competent animal model of HCC. This is undoubtedly due to the additional inherent technical challenges associated with these models, such as rapid immune clearance of the virus and

high background in the liver due to hepatic excretion of many tracers, which consequently causes strong background accumulation and unfavorable signal-to-noise-ratios for targets located in the liver.

Nevertheless, it is extremely important to establish viral imaging modalities, especially now that many OVs have entered the clinic and are being applied to patients. A trackable virus offers the possibility to monitor virus distribution inside the body while avoiding invasive procedures, like biopsies. Whole body imaging allows the monitoring of all tissues at the same time and in a very short period of time. This stands in contrast to punctual and locally isolated biopsies were the physician receives very limited and sometimes unrepresentative results of what is happening inside the patient. Non-invasive imaging of OVs also might help to identify possible off-target replication of the viruses, which is one of the major concerns in OV therapy and in that way could have a great impact on the safety of the therapy. Additionally, non-invasive imaging can be applied on several consecutive days without causing any harm to the patient. This means that the viral replication and fate can be monitored in real-time, so that completely individualized treatment options can be designed and applied to each patient [84, 137].

When choosing an appropriate reporter system for non-invasive *in vivo* imaging, several points have to be considered. First, the modality, by which the detection should be performed, has to be chosen. In this thesis, we aimed to establish a translatable system with the opportunity of a directly applicable transfer into the clinic, a decision for combined PET/CT was made. The combination of PET and CT unites anatomical imaging (CT) with functional imaging (PET) and,

therefore, offers multimodal and very accurate information. Moreover, using PET as a functional imaging modality provides several benefits. First of all, the higher tissue penetration of the signal by radiotracers is much more favorable for imaging of patients than those of optical tracers. So far, optical tracers face limited applications due to this fact. To date, optical imaging in the clinic unique applications are in imaging of breast cancer or intra-operative imaging but not for deep tissues imaging due to a too low penetration of the tissue by the signal [138-140].

5.1.1 *In vivo* imaging of rVSV-rNIS

One potential candidate as suitable reporter gene was the rat sodium iodine symporter (rNIS). In the first step a novel recombinant VSV vector encoding for rNIS was successfully cloned and rescued. Additionally, a stably rNIS-expressing rat HCC cell line was established. The novel cell line and virus were tested *in vitro* for the expression of the rNIS reporter protein and also its functionality. The *in vitro* tracer uptake assay revealed some uptake of iodine in untreated Morris cells. This specific and potassium-perchlorate ($KClO_4$)-blockable iodine uptake could be due to endogenous NIS expression in HCC, which has already been described before [141]. Nevertheless, since no NIS expression could be detected by indirect immunofluorescence (Figure 14) and the tracer uptake of rVSV-rNIS-infected cells was more then doubled, the endogenous iodine uptake of the Morris wt cells was considered as background and NIS was investigated further as possible reporter gene in our model.

The first *in vivo* application was a proof-of-principle imaging with subcutaneous tumors of the stable rNIS cell line at one wt Morris tumors at the other shoulder.

A subcutaneous model was chosen in order to facilitate the conditions and to rule out tumor location-based variability. Those tumors of the stably rNIS-expressing cell line were considered as a positive control with maximum tracer uptake in the imaging.

Surprisingly, the PET/CT scans (Figure 17) show no specific uptake in the stable rNIS tumors. Moreover, a very strong signal was detected in the liver regions of all animals. Subsequent quantitative region of interest (ROI) analysis (Figure 18) showed that the signal detected in the liver is even higher than the signal of both, the stable rNIS-expressing and the wt, tumors.

We hypothesized that the low tracer uptake in the tumors of the stably rNIS-expressing cell line could be due to the loss of ther reporter *in vivo*, since no drug was applied upon implantation into the animals to provide selective pressure and guarantee for the reporter protein expression. A subgroup of the animals was sacrificed after the imaging and the tumors were analysed *ex vivo*. Immunohistological analysis demonstrated high expression of the reporter protein in the stably rNIS-expressing tumors (Figure 19), why loss of reporter gene expression cannot explain the low signals.

Before ruling out NIS as a suitable reporter gene in our system, we decided to apply ^{124}I-PET/CT imaging to rVSV-rNIS-treated tumors. To this end, the wt tumors were injected intratumorally with 1x 10^7 pfu rVSV-rNIS and image acquisition was performed 15 h after virus application. PET/CT scans of these animals (Figure 20) and ROI analysis (Figure 21) showed no significant tracer uptake in both, neither in the stably rNIS-expressing, nor in the rVSV-rNIS-treated, tumors.

Ex vivo immunohistological analysis demonstrated expression of the reporter

protein in both tumors. The rVSV-rNIS-treated tumors exhibited a patchy rNIS protein expression pattern. A patchy expression pattern has been reported before for VSV-proteins (i.e. VSV-G) after intratumorally VSV-treated tumors [73]. Even though the histological detection of the rNIS protein is not absolutely accurate and quantitative, the low expression is not optimal for imaging attempts and might be one crucial reason for the failure of the attempt.

Of relevance, the sodium iodide symporter has previously been described as a successful reporter in a hepatocellular carcinoma model [142, 143]. In these studies beneficial biodistribution of the iodine tracer in a rodent models were shown.

Additionally, there is an abundance of evidence in the literature in support of the use of the NIS as an ideal reporter for virus imaging [144-146]. NIS has been employed for imaging replicating adenovirus resulting in a favourable detection of the reporter in host cells *in vivo* after viral delivery [145, 147]. However, in these studies, which describe successful application of the NIS reporter after non-viral and viral delivery, hepatoma xenografts were employed as tumor models. Although their results are in stark contrast to our results, we speculate that there could be several possible explanations. For our studies an immune-competent model was used, which results in relatively rapid clearance of the virus from the host and could severly limit the kinetics of the NIS expression. Moreover, our studies involved tumors located orthotopically in the liver. A known drawback of NIS as a reporter is the high tracer uptake in the stomach in rodent models, which have a much higher expression of NIS in the stomach than humans [148]. This was also monitored in our study. The high noise by the background signal of the stomach might have produced a false and artificially

high liver background signal, which resulted in the poor tumor:liver signals shown in our study. A possible solution to this problem is the application of barium sulfate, which might inhibit the uptake of radioactive iodine in the stomach as described recently [149].

An additionaly challenge to imaging of VSV is the kinetics of viral replication and clearance. A replication cycle is completed within 8 to 12 hours and oncolysis of infected cells can be expected shortly thereafter. For this reason, the time window for the detection of a potential reporter in infected cells is very narrow. A reporter that is a transporter with intramembrane localization, which demands delicate processing and transportation after translation, might be an especially risky choice for imaging VSV.

Nevertheless, a recombinant VSV(Δ51)-NIS vector has previously been reported for *in vivo* imaging in a multiple myeloma model in immunocompromised mice and could be imaged successfully [90]. We speculate that the failure in our model could be attributed to the functional immune system or the fact that we used the wild-type VSV backbone, in which the endogenous matrix protein (as opposed to the MΔ51 mutant used in the Goel et al. study) shuts down host gene expression and perhaps interferes with the ability of NIS to function as a transporter. Regardless of the reason, we decided not to pursue NIS in further studies, as we had already accumulated substantial data to indicate that it is not an ideal reporter in our system.

We concluded that rVSV-NIS was not an ideal vector for *in vivo* imaging of therapy in our orthotopic HCC model, at least partially due to the position of the

liver, which results in high background signals from endogenous NIS expression in the neighboring stomach.

In summary, even though NIS could be shown to be a suitable reporter in many other models, the signal to noise ratios seem to be insuperable for targets in the liver in the immunocompetent Morris hepatoma model for imaging of VSV.

5.1.2 *In vivo* rVSV-HSV1-sr39tk imaging

After declaring rNIS as not suitable for imaging VSV in the Morris hepatoma model, we aimed to identify a reporter with low or no endogenous expression, and herpes simplex virus 1- semi-random mutation 39- thymidine kinase (HSV1-sr39tk) proved to be an ideal candidate. The HSV1-sr39tk reporter, together with the FHBG tracer, has already been shown to be a successful combination for hepatic imaging by other groups [97, 98].

The same strategy as for the rNIS reporter was followed and the stable HSV1-sr39tk-expressing cell line as well as the successfully cloned and rescued rVSV-HSV1-sr39tk showed high and functional HSV1-tk reporter protein expression *in vitro* (figures 24 – 29).

A proof-of-principle study was performed with subcutaneous tumors of the stable HSV1-sr39tk reporter cell line at the right and wt tumors at the left shoulders in the each animal (Figure 30). Image acquisition was performed 2 h after application of the tracer, as this seemed to be a good time point estimated from previous biodistribution studies [96]. PET/CT imaging revealed highly specific FHBG tracer uptake only in the tumors of the stable cell line, while wt tumors remained without high signals compared to liver. PET data were

validated *ex vivo* by comparison with autoradiography and immunohistochemistry of the respective tissue sections.

Although, we were expecting homogenously high expression of HSV-TK in the stable HSV1-sr39tk-expressing tumors, we observed sparse and patchy expression patterns by immunohistochemical analysis. This observation could be partially due to low sensitivity of the antibody used, which would result in visualization of only those cells with very high HSV-TK expression. However, we believe that this observation is an accurate reflection of the loss of signal, due to the lack of drug selection and subsequent loss of gene expression *in vivo* (Figure 32 and Figure 33).

After the successful proof-of-principle imaging, *in vivo* imaging of the novel recombinant rVSV-HSV1-sr39tk vector was performed in orthotopic unifocal HCCs. The rVSV-HSV1-sr39tk was injected intratumorally at the previously determined maximum tolerated dose of VSV of 1x 10^7. PET/CT scans were performed one day after treatment, which presents the previously determined time point of peak in virus replication [73].

All PET data in this study were validated *ex vivo* by comparison with autoradiography and immunohistochemistry of the respective tissue sections. In all cases, PET and autoradiography analyses produced nearly identical tumor:liver ratios, confirming that the PET signals did indeed originate from the tumor tissue and correlate with ^{18}F-FHBG uptake. Furthermore, by overlaying autoradiography and immunohistochemistry from the same tissue sections, we were able to determine that patterns of tracer uptake were quite similar to those of HSV-TK expression. Although signals were not completely identical, we attribute the discrepancies to differences in sensitivity of the two methods and to

the fact that the thick tissue sections (about 1mm) used for autoradiography were sub-sectioned to 3 µm thickness for immunohistochemistry. As a consequence, the autoradiography data represent the average of a much thicker slice of tumor.

Nonspecific tracer uptake after injection of VSV could be ruled out by the negativity of the tumor signal upon injection of rVSV-lacZ.

Interestingly, the expression of the HSV1-tk protein could be detected close to the necrotic areas in the rVSV-HSV1-sr39tk-treated tumors, indicating that the expression of the reporter occurs shortly before the VSV-directed cell lysis.

The FHBG tracer is excreted via the kidneys and, therefore, no unwanted liver accumulation was expected. The desirable biodistribution of the FHBG tracer could be proven in a preclinical mouse model as well as in humans before [95, 96], and similar biodistributions could be found in this study (Figure 41).

As a subsequent step, the detection limit of rVSV-HSV1-sr39tk was identified. Orthotopic tumors were injected with log-wise increasing doses of rVSV-HSV1-sr39tk from 1x 10^4 to 1x 10^7 pfu. FHBG-PET/CT was performed on day 1 after treatment (Figure 42). Interestingly, a viral dose of only 10^6 pfu VSV-HSV1-sr39tk could already be shown to generate an increased tumor signal in FHBG-PET by quantitative ROI analysis (Figure 43).

Correlation of intratumoral virus titer in groups with tumor-to-liver ratios above the PBS background resulted in a goodness of fit of R^2 = 0.6653. This data indicates the reliability of the established system with the additional benefit of providing information on the intratumoral viral titer.

Moreover, the peak of the PET signal in the kinetic study detected on day 1, which is still stable on day 2, could give a first impression on the behavior of the tumor FHBG uptake upon treatment with rVSV-HSV1-sr39tk. However, due to the limited time period of monitoring this data is only prelimnary and a study with consecutive imagings of the same animals over a longer period remains to be done. Nevertheless, from our previous studies showing the replication kinetics of VSV in orthotopic HCC tumors, with the viral titer peaking on day 1, followed by a strong titer reduction on day 3 we would expect a similar detection pattern by FHBG-PET [73, 76].

Although we have not explicitly evaluated the efficacy of the rVSV-HSV1-sr39tk virus in vivo in this study, our *in vitro* data demonstrated that the recombinant vector was nearly identical to the control rVSV-GFP vector with respect to replication kinetics and tumor cell killing. Therefore, we expect that the in vivo efficacy of this recombinant vector should not be significantly altered in comparison to the rVSV-GFP vector, which we have thoroughly demonstrated in the same HCC model used in the current study.

An additional benefit of incorporation of HSV-TK into the VSV vector is the possibility of exploiting the transgene as a suicide gene and thereby enhancing the therapeutic effect of VSV upon application of the prodrug ganciclovir (GCV), which has been reported previously as a successful therapy option for HCC [150] and could improve the therapeutic efficacy of oncolytic VSV. Additionally, the combination of HSV-TK and prodrug therapy has been shown to be effective in a clinical trial for HCC [151], and synergistic tumor responses were reported as a result of VSV-mediated expression of the wildtype HSV-TK in

combination with GCV in a mammary carcinoma and melanoma model [72]. However, since this thesis focused on the characterization of the TK-reporting virus as an imaging vector, the additional therapeutic benefits conferred by combination therapies were beyond the experimental scope.

5.1.3 Conclusion and outlook

In this thesis we have successfully established a trackable recombinant VSV, which not only maintains its efficacy for treatment of HCC, but it enables *in vivo* monitoring of virus replication. We have demonstrated HSV1-sr39tk to be an ideal reporter for VSV therapy of HCC, due to strong vector-specific signals, low background, and correlation between viral titer and the respective PET signal. This represents a major step forward in the clinical development of VSV as an oncolytic agent for HCC, as it allows for non-invasive imaging of viral therapy to monitor safety and potentially facilitate novel combination therapies. We envision the possibility that this tool might additionally serve as a predictor of therapy outcome, as strong virus replication, resulting in high PET signals could indicate for strong therapy responses and subsequent survival benefits. Therefore, possible correlations of the initial FHBG-PET signal after VSV-sr39tk therapy should be a major focus of the future research with this model.

In summary, these results demonstrate the establishment of an imaging system in a highly challenging preclinical model. We believe this reporter system to be highly relevant and readily translatable for non-invasive tracking of oncolytic virus therapy and offering individualized therapy options while simultaneously providing the option of combination therapy with GCV, which is why the novel VSV-HSV1-sr39tk vector might even function as a theranostic virus in future clinical applications.

5.2 Response imaging

5.2.1 Imaging tumor responses to oncolytic virotherapy

The metabolism of cancerous tissue often shows high alterations compared to healthy tissue. These changes can be employed for as biomarkers. Biomarkers can serve for the detection (diagnostic biomarker) or the prognosis (prognostic biomarker) of tumors and they can even be used for the stratification of patients and therapies to offer personalized treatment (predictive biomarker) [152]. One possible application of biomarkers is in biomedical imaging, where specific biomarker-based probes (i.e. tracer) can be designed to detect metabolic changes in diseased tissue.

In this thesis we were aiming to identify a suitable PET response tracer for the detection of the responses of tumors after the treatment with oncolytic VSV. Imaging with the identified tracer should in a first step give information about response of the tumor to the viral treatment in order to in a next step enable to identify a correlation of specific changes in tracer uptakes in virus-treated tumors to later being able to, on the one hand, find the optimal and individual therapy schedule for every patient and, on the other hand, to stratify patients for VSV therapy (predictive marker).

Even though the aim here was not to identify a diagnostic marker for HCC, tracer biodistributions of possible candidates needed to be considered in order to avoid unfavorable ratios due to high hepatic accumulations.

5.2.2 ^{18}F-FDG-PET

The most versatile and frequently used for PET tracer for the imaging of tumors is ^{18}F-FDG. Numerous studies concentrated on the suitability of FDG for the detection of cancerous lesions in the liver are reporting contradicting results. While some studies report FDG-PET not being ideal for the detection of tumors in the liver [109, 110] other groups successfully used FDG-PET in other

approaches as a prognostic biomarker for the characterization of HCC lesions [153, 154]. Additionally, FDG-PET has been shown to be a predictive marker for tumor control in HCC after SABR (stereotactic ablative radiotherapy) [155] Moreover, other tumors have been reported to be reliably identified by FDG-PET combined imaging approaches [156].

Therefore, FDG-PET was considered a reasonable candidate in our approach.

The orthotopic HCCs in the Morris hepatoma model was successfully detected and relative signal to noise ratios of the tumor lesions in the liver were shown to be very favorable after PET ROI analysis (Figure 50). Nevertheless, a very high tracer uptake could also be detected in the scar tissue from the surgery, which was performed 10 days in advance. This strong uptake of FDG in inflamed tissue is well known and characteristic for FDG imaging [157].

Nevertheless, inflammatory responses to VSV are a possible aspect of the tumor response. Therefore, the FDG signal and its changes upon oncolytic virus treatment are possibly of importance in order to fully monitor all aspects of the tumoral response. Therefore, the application of additional tracers for the discrimination of tumoral against inflammatory FDG signal are mandatory. This issue has been addressed by other goups before.

FET- and FLT-PET were performed in a rat model in order to reliably identify the different reasons for high FDG uptake and combined imaging reliably enabled discrimination of the inflamed versus cancerous tissue [158].

In conclusion, since inflammation often occurs in tumor tissue upon OV therapy, a change in the FDG signal in response to treatment could possibly provide precious information on the success of the OV therapy in a patient and should possibly combined with other response imaging modalities as described in the following sections.

5.2.3 ^{18}F-FET-PET

As already mentioned above, FET-PET has been reported before to be a valuable tool for the discrimination of cancerous against inflammatory tissue [159]. The same rats, which had been used for the screening of FDG the day before, have been scanned via FET-PET/CT. Unfortunately, no tumor specific tracer uptake could be detected (Figure 51). Nevertheless, it is still possible that intratumoral tracer uptake could occur in response to VSV treatment. A very interesting fact is, that FET revealed favorable uptake ratios in the liver, with a very low liver:muscle ratio of 1.

5.2.4 ^{18}F-FLT-PET

Another previously mentioned candidate for the discrimination of cancerous against inflammatory tissue is FLT (Lee, Ahn et al. 2009). But moreover, FLT solely has already been reported as a reliable tracer for the detection of HCC in patients [126].

When the FLT tracer was applied for the detection of HCC lesions in the Morris hepatoma model, the tumors could be detected in all animals with some physiological background uptake in the liver (Figure 53).

For this first screening the protocol suggested by Eckel et al. was applied, i.e. static image acquisition for 15 min, 45 min after tracer application, which represents the standard protocol for FLT imaging in preclinical models [160, 161]. Dynamic imaging in our HCC model indicated that the optimal time point is reached much later at 105 min after FLT tracer application (Figure 54).

In the following study, the acquisition time point was changed according to this finding. HCC-bearing rats were imaged one day before and one day after intra-

arterial treatment with either rVSV-rNIS or PBS as control. While the FLT uptake remained at the same level before and after treatment in PBS-treated tumors, a decrease in tracer uptake was detected in VSV-treated tumors upon treatment (Figure 56). This decrease does probably indicate a reduction in the proliferation of these tumors. But notably, we cannot identify the exact pathway in this set up. Other studies could more precisely correlate the reduction in the FLT signal to tumor growth reduction by the inhibition of specific pathways. Here, we can only speculate about the various anti-tumor effects of VSV, which then may result in a synergistic anti-proliferative therapeutic in our model indicated by reduced FLT signals [162, 163].

5.2.5 Conclusion and outlook

Since the studies on the imaging of tumor responses to VSV treatment were at a preliminary state, none of the screened response tracers can really be excluded.

FLT showed a high potential for imaging responses of HCCs to oncolytic VSV therapy, but the presented data is only preliminary due to the very small number of animals in the groups. Nevertheless, the trend of the tissue uptake kinetics upon viral treatment is very promising and should be investigated further.

Another well-described tracer for the imaging of HCC is ^{18}F-methyl-choline [164]. This PET tracer seems to be very reliable in the staging of HCC and might therefore also be a suitable tracer for imaging HCC responses after OV therapy. This will be investigated in future studies, but was beyond the scope of the thesis work.

For sure, confining the response imaging to only one modality or tracer does only offer a limited insight of processes happening inside the treated tumor. The key will be to combine several modalities and techniques in order to get a reliable and informative insight of the tumor response upon VSV treatment. These combinations could consist of the two functional imaging modalities as it is done in PET/MRI (magnetic resonance imaging) [165]. In this way, not only one aspect of the tumor's behavior upon treatment can be tested at once, but, the imaging by an appropriate PET tracer could be combined with functional MRI, and detect perfusion and diffusion of the lesions simultaneously. Moreover, it might be possible to monitor inflammation via ^{19}F-MRI, which has recently been reported before as a promising response imaging option for OV therapy [166], while the tumor growth is detected by FLT-PET. Also, a combination of several PET tracers in the same animal could result more detailed and complex information [158].

In conclusion, there is still the need of further investigations on this topic. Especially with various OV therapy entering the clinic, a reliable tumor response imaging protocol for these potent but complex anti-tumor drugs needs to be established based on predictive markers. Based on a reliable imaging protocol optimized OV therapy for each individual cancer patient could be realized in future clinical applications.

6 SUMMARY

Hepatocellular carcinoma (HCC) is the most predominant form of liver cancer and the third leading cause of cancer-related death worldwide. As conventional therapies are largely ineffective and the prognosis remains poor, novel therapies employing oncolytic viruses (OV) have emerged as promising treatment alternatives. Because of valid safety concerns associated with administering replicating vectors in patients, the need to monitor the virus and the responses to OV therapy non-invasively and in real-time has become a priority. Therefore, the first aim of this thesis was to establish a system to reliably and sensitively image oncolytic vesicular stomatitis virus (VSV) in a clinically relevant model of HCC. To this end, an orthotopic Morris HCC model in immune-competent, syngeneic Buffalo rats was used to test recombinant VSV vectors encoding for reporters, which would allow the indirect detection of specific VSV signals in the liver via positron emission tomography (PET) imaging. Although the sodium iodide symporter (NIS) has been shown to be a suitable reporter for PET imaging of viruses in other tumor models, here, NIS was inappropriate for the detection of VSV in orthotopic HCC nodules, due to strong iodide uptake in the stomach and weak specific signals produced in the tumors, despite high levels of virus-mediated NIS expression demonstrated by immunohistochemical analysis. As an alternative, the use of an enhanced version of the Herpes-Simplex 1- thymidine kinase (HSV1-sr39tk) reporter has been investigated. Application of the recombinant VSV-sr39tk resulted in minimal background signals and allowed us to sensitively detect VSV via ^{18}F-FHBG PET.

In order to find a reliable tracer to detect tumor responses to OV therapy via PET/CT, established tracers have been screened. While ^{18}F-FDG and ^{18}F-FET offered unsatisfactory results, ^{18}F-FLT showed promising results in preliminary imaging studies.

In conclusion, the results of this thesis demonstrate an accurate and sensitive system for non-invasive imaging of oncolytic VSV in a clinically-relevant HCC model, which could be translated into a valuable tool for patient monitoring as oncolytic viruses advance further in clinical applications and presents a possible tumor response PET-tracer for HCC after VSV therapy.

7 REFERENCES

1. Parkin, D.M., et al., *Global cancer statistics, 2002.* CA Cancer J Clin, 2005. **55**(2): p. 74-108.
2. Jemal, A., et al., *Global patterns of cancer incidence and mortality rates and trends.* Cancer Epidemiol Biomarkers Prev, 2010. **19**(8): p. 1893-907.
3. Forner, A., J.M. Llovet, and J. Bruix, *Hepatocellular carcinoma.* Lancet, 2012. **379**(9822): p. 1245-55.
4. Ferlay, J., et al., *Estimates of worldwide burden of cancer in 2008: GLOBOCAN 2008.* Int J Cancer, 2010. **127**(12): p. 2893-917.
5. Bosch, F.X., et al., *Primary liver cancer: worldwide incidence and trends.* Gastroenterology, 2004. **127**(5 Suppl 1): p. S5-S16.
6. Barazani, Y., et al., *Chronic viral hepatitis and hepatocellular carcinoma.* World J Surg, 2007. **31**(6): p. 1243-8.
7. Altekruse, S.F., K.A. McGlynn, and M.E. Reichman, *Hepatocellular carcinoma incidence, mortality, and survival trends in the United States from 1975 to 2005.* j Clin Oncol, 2009. **27**(9): p. 1485-91.
8. Pawlik, T.M., et al., *Tumor size predicts vascular invasion and histologic grade: Implications for selection of surgical treatment for hepatocellular carcinoma.* Liver Transpl, 2005. **11**(9): p. 1086-92.
9. Poon, R.T., et al., *Long-term survival and pattern of recurrence after resection of small hepatocellular carcinoma in patients with preserved liver function: implications for a strategy of salvage transplantation.* Ann Surg, 2002. **235**(3): p. 373-82.
10. Kim, W.R., Gores, G., Benson, J., et al, *Mortality and hospital utilization for hepatocellular carcinoma in the United States.* Gastroenterology, 2005. **129**: p. 486-493.
11. Yao, F., Bass, NM., Nikolai, B., et al, *Liver transplantation for hepatocellular carcinoma: analysis of survival according to the intention-to-treat principle and dropout from the waiting list.* Liver Transpl, 2002. **8**: p. 873-83.
12. Shrimal, A., M. Prasanth, and A.V. Kulkarni, *Interventional radiological treatment of hepatocellular carcinoma: an update.* Indian J Surg, 2012. **74**(1): p. 91-9.
13. Llovet, J.M., et al., *Sorafenib in advanced hepatocellular carcinoma.* N Engl J Med, 2008. **359**(4): p. 378-90.
14. Bruix, J., et al., *Efficacy and safety of sorafenib in patients with advanced hepatocellular carcinoma: subanalyses of a phase III trial.* J Hepatol, 2012. **57**(4): p. 821-9.
15. Mazioti, A., et al., *Safety and efficacy of transcatheter arterial chemoemboliazation in the real-life management of unresectable hepatocellular carcinoma.* Hepat Mon, 2013. **13**(8): p. e7070.
16. Ikeda, M., et al., *Efficacy of sorafenib in patients with hepatocellular carcinoma refractory to transcatheter arterial chemoembolization.* J Gastroenterol, 2013.
17. Kirn, D., Martuza, R.L., and Zwiebel, J., *Replication-selective virotherapy for cancer: biological principles, risk management, and future directions.*

Nat Med, 2001. **7**: p. 781-7.
18. Parato, K.A., et al., *Recent progress in the battle between oncolytic viruses and tumours.* Nat Rev Cancer, 2005. **5**(12): p. 965-76.
19. Russell, S.J. and K.W. Peng, *Viruses as anticancer drugs.* Trends Pharmacol Sci, 2007. **28**(7): p. 326-33.
20. Bierman, H.R., et al., *Remissions in leukemia of childhood following acute infectious disease: staphylococcus and streptococcus, varicella, and feline panleukopenia.* Cancer, 1953. **6**(3): p. 591-605.
21. Dock, G., *The influence of complicating diseases upon leukemia.* Am J Med Sci, 1904. **127**: p. 563-92.
22. Pelner, L., G.A. Fowler, and H.C. Nauts, *Effects of concurrent infections and their toxins on the course of leukemia.* Acta Med Scand Suppl, 1958. **338**: p. 1-47.
23. Sinkovics, J.G. and J.C. Horvath, *Newcastle disease virus (NDV): brief history of its oncolytic strains.* J Clin Virol, 2000. **16**(1): p. 1-15.
24. Bourke, M.G., et al., *The emerging role of viruses in the treatment of solid tumours.* Cancer Treat Rev, 2011. **37**(8): p. 618-32.
25. Kelly, E. and S.J. Russell, *History of oncolytic viruses: genesis to genetic engineering.* Mol Ther, 2007. **15**(4): p. 651-9.
26. Martuza, R.L., et al., *Experimental therapy of human glioma by means of a genetically engineered virus mutant.* Science, 1991. **252**(5007): p. 854-6.
27. Miyatake, S., et al., *Transcriptional targeting of herpes simplex virus for cell-specific replication.* J Virol, 1997. **71**(7): p. 5124-32.
28. Rodriguez, R., et al., *Prostate attenuated replication competent adenovirus (ARCA) CN706: a selective cytotoxic for prostate-specific antigen-positive prostate cancer cells.* Cancer Res, 1997. **57**(13): p. 2559-63.
29. Kuhn, I., et al., *Directed evolution generates a novel oncolytic virus for the treatment of colon cancer.* PLoS One, 2008. **3**(6): p. e2409.
30. Edge, R.E., et al., *A let-7 MicroRNA-sensitive vesicular stomatitis virus demonstrates tumor-specific replication.* Mol Ther, 2008. **16**(8): p. 1437-43.
31. Kelly, E.J., et al., *Engineering microRNA responsiveness to decrease virus pathogenicity.* Nat Med, 2008. **14**(11): p. 1278-83.
32. Russell, S.J., K.W. Peng, and J.C. Bell, *Oncolytic virotherapy.* Nat Biotechnol, 2012. **30**(7): p. 658-70.
33. Al-Hendy, A., *Gene therapy of epithelial ovarian cancer using adenoviral vectors.* Prim Care Update Ob Gyns, 1998. **5**(4): p. 158.
34. Doronin, K., et al., *Tumor-specific, replication-competent adenovirus vectors overexpressing the adenovirus death protein.* J Virol, 2000. **74**(13): p. 6147-55.
35. Wong, R.J., et al., *Cytokine gene transfer enhances herpes oncolytic therapy in murine squamous cell carcinoma.* Hum Gene Ther, 2001. **12**(3): p. 253-65.
36. Dingli, D., et al., *Image-guided radiovirotherapy for multiple myeloma using a recombinant measles virus expressing the thyroidal sodium iodide symporter.* Blood, 2004. **103**(5): p. 1641-6.
37. Kim, J.H., et al., *Relaxin expression from tumor-targeting adenoviruses and its intratumoral spread, apoptosis induction, and efficacy.* J Natl Cancer Inst, 2006. **98**(20): p. 1482-93.
38. Aghi, M., et al., *Multimodal cancer treatment mediated by a replicating*

oncolytic virus that delivers the oxazaphosphorine/rat cytochrome P450 2B1 and ganciclovir/herpes simplex virus thymidine kinase gene therapies. Cancer Res, 1999. **59**(16): p. 3861-5.
39. Thorne, S.H., R.S. Negrin, and C.H. Contag, *Synergistic antitumor effects of immune cell-viral biotherapy.* Science, 2006. **311**(5768): p. 1780-4.
40. Morrison, J., et al., *Virotherapy of ovarian cancer with polymer-cloaked adenovirus retargeted to the epidermal growth factor receptor.* Mol Ther, 2008. **16**(2): p. 244-51.
41. Cattaneo, R., et al., *Reprogrammed viruses as cancer therapeutics: targeted, armed and shielded.* Nat Rev Microbiol, 2008. **6**(7): p. 529-40.
42. Dorer, D.E. and D.M. Nettelbeck, *Targeting cancer by transcriptional control in cancer gene therapy and viral oncolysis.* Adv Drug Deliv Rev, 2009. **61**(7-8): p. 554-71.
43. Patel, M.R. and R.A. Kratzke, *Oncolytic virus therapy for cancer: the first wave of translational clinical trials.* Transl Res, 2013. **161**(4): p. 355-64.
44. Ottolino-Perry, K., et al., *Intelligent design: combination therapy with oncolytic viruses.* Mol Ther, 2010. **18**(2): p. 251-63.
45. Hastie, E. and V.Z. Grdzelishvili, *Vesicular stomatitis virus as a flexible platform for oncolytic virotherapy against cancer.* J Gen Virol, 2012. **93**(Pt 12): p. 2529-45.
46. Lichty, B.D., et al., *Vesicular stomatitis virus: re-inventing the bullet.* Trends Mol Med, 2004. **10**(5): p. 210-6.
47. Ball, L.A., et al., *Phenotypic consequences of rearranging the P, M, and G genes of vesicular stomatitis virus.* J Virol, 1999. **73**(6): p. 4705-12.
48. Gaddy, D.F. and D.S. Lyles, *Vesicular stomatitis viruses expressing wild-type or mutant M proteins activate apoptosis through distinct pathways.* J Virol, 2005. **79**(7): p. 4170-9.
49. Rose, J.K., Whitt, M.A., *Rhabdoviridae: the viruses and their replication*, in *Fields Virology*, D.M. Knipe, Howley, P.M., Editor. 2001, Lippincott Williams & Wilkins: Philidelphia. p. p. 1221-42.
50. Oliere, S., et al., *Vesicular stomatitis virus oncolysis of T lymphocytes requires cell cycle entry and translation initiation.* J Virol, 2008. **82**(12): p. 5735-49.
51. Fields, B.N., D.M. Knipe, and P.M. Howley, *Fields virology*. 6th ed. 2013, Philadelphia: Wolters Kluwer Health/Lippincott Williams & Wilkins.
52. Ge, P., et al., *Cryo-EM model of the bullet-shaped vesicular stomatitis virus.* Science, 2010. **327**(5966): p. 689-93.
53. Finkelshtein, D., et al., *LDL receptor and its family members serve as the cellular receptors for vesicular stomatitis virus.* Proc Natl Acad Sci U S A, 2013. **110**(18): p. 7306-11.
54. Georgel, P., et al., *Vesicular stomatitis virus glycoprotein G activates a specific antiviral Toll-like receptor 4-dependent pathway.* Virology, 2007. **362**(2): p. 304-13.
55. Rieder, M. and K.K. Conzelmann, *Rhabdovirus evasion of the interferon system.* J Interferon Cytokine Res, 2009. **29**(9): p. 499-509.
56. Staeheli, P. and J. Pavlovic, *Inhibition of vesicular stomatitis virus mRNA synthesis by human MxA protein.* J Virol, 1991. **65**(8): p. 4498-501.
57. Krishnamoorthy, J., et al., *The eIF2alpha kinases inhibit vesicular stomatitis virus replication independently of eIF2alpha phosphorylation.* Cell Cycle, 2008. **7**(15): p. 2346-51.
58. Dinh, P.X., et al., *Antagonistic effects of cellular poly(C) binding proteins*

on vesicular stomatitis virus gene expression. J Virol, 2011. **85**(18): p. 9459-71.
59. Chelbi-Alix, M.K., et al., *Resistance to virus infection conferred by the interferon-induced promyelocytic leukemia protein.* J Virol, 1998. **72**(2): p. 1043-51.
60. Weidner, J.M., et al., *Interferon-induced cell membrane proteins, IFITM3 and tetherin, inhibit vesicular stomatitis virus infection via distinct mechanisms.* J Virol, 2010. **84**(24): p. 12646-57.
61. Sarojini, S., T. Theofanis, and C.S. Reiss, *Interferon-induced tetherin restricts vesicular stomatitis virus release in neurons.* DNA Cell Biol, 2011. **30**(12): p. 965-74.
62. Barber, G., *Vesicular stomatitis virus as an oncolytic vector.* Viral Immunology, 2004. **17**(4): p. 516-27.
63. Li, Q. and M.A. Tainsky, *Epigenetic silencing of IRF7 and/or IRF5 in lung cancer cells leads to increased sensitivity to oncolytic viruses.* PLoS One, 2011. **6**(12): p. e28683.
64. Marozin, S., Altomonte, J., Stadler, F., Thasler, W.E., Schmid, R.M., and Ebert, O., *Inhibition of the IFN-beta response in hepatocellular carcinoma by alternative spliced isoform of IFN regulatory factor-3.* Mol Ther, 2008. **16**(11): p. 1789-97.
65. Stojdl, D.F., Lichty, B.D., tenOever, B.R., et al, *VSV strains with defects in their ability to shutdown innate immunity are potent systemic anti-cancer agents.* Cancer Cell, 2003. **4**(4): p. 263-75.
66. Stojdl, D.F., et al., *Exploiting tumor-specific defects in the interferon pathway with a previously unknown oncolytic virus.* Nat Med, 2000. **6**(7): p. 821-5.
67. Zhang, H., Wen, Y.J., Mao, B.Y., Gong, Q.Y. Qian, Z.Y. and Wei, Y.Q., *Plasmid encoding matrix protein of vesicular stomatitis viruses as an antitumor agent inhibiting rat glioma growth in situ.* Exp Oncol, 2007. **29**(2): p. 85-93.
68. Bi, Z., Barna, M., Komatsu, T., et al, *Vesicular stomatitis virus infection of the central nervous system activates both innate and acquired immunity.* Journal of Virology, 1995a. **69**: p. 6466-72.
69. van den Pol, A., Dalton, K., and Rose, J., *Relative neurotropism of a recombinant rhabdovirus expressing a green fluorescent envelope glycoprotein.* Journal of Virology, 2002. **76**(3): p. 1309-27.
70. Balachandran, S., M. Porosnicu, and G.N. Barber, *Oncolytic activity of vesicular stomatitis virus is effective against tumors exhibiting aberrant p53, Ras, or myc function and involves the induction of apoptosis.* J Virol, 2001. **75**(7): p. 3474-9.
71. Balachandran, S.a.B., G.N., *Vesicular stomatitis virus (VSV) therapy of tumors.* IUBMB Life, 2000. **50**(2): p. 135-8.
72. Fernandez, M., Porosnicu, M., Markovic, D., and Barber, G.N., *Genetically engineered vesicular stomatitis virus in gene therapy: application for treatment of malignant disease.* J Virol, 2002. **76**: p. 895-904.
73. Ebert, O., Shinozaki, K., Huang, T.G., Savontaus, M.J., Garcia-Sastre, A., and Woo, S.L.C., *Oncolytic vesicular stomatitis virus for treatment of orthotopic hepatocellular carcinoma in immune-competent rats.* Cancer Research, 2003. **63**(13): p. 611-3.
74. Breedis, C. and G. Young, *The blood supply of neoplasms in the liver.* Am J Pathol, 1954. **30**(5): p. 969-77.

75. Mohr, L., Geissler, M., et al, *Gene therapy for malignant liver disease.* Expert Opin Biol Ther, 2002. **2**(2): p. 163-75.
76. Shinozaki, K., et al., *Oncolysis of multifocal hepatocellular carcinoma in the rat liver by hepatic artery infusion of vesicular stomatitis virus.* Mol Ther, 2004. **9**(3): p. 368-76.
77. Ebert, O., Shinozaki, K., Kournioti, C., et al, *Syncytia induction enhances the oncolytic potential of vesicular stomatitis virus in virotherapy for cancer.* Cancer Research, 2004. **64**: p. 3265-70.
78. Shinozaki, K., O. Ebert, and S.L. Woo, *Eradication of advanced hepatocellular carcinoma in rats via repeated hepatic arterial infusions of recombinant VSV.* Hepatology, 2005. **41**(1): p. 196-203.
79. Altomonte, J., et al., *Synergistic antitumor effects of transarterial viroembolization for multifocal hepatocellular carcinoma in rats.* Hepatology, 2008. **48**(6): p. 1864-73.
80. Altomonte, J., et al., *Exponential enhancement of oncolytic vesicular stomatitis virus potency by vector-mediated suppression of inflammatory responses in vivo.* Mol Ther, 2008. **16**(1): p. 146-53.
81. Altomonte, J., et al., *Enhanced oncolytic potency of vesicular stomatitis virus through vector-mediated inhibition of NK and NKT cells.* Cancer Gene Ther, 2009. **16**(3): p. 266-78.
82. Altomonte, J., et al., *Antifibrotic Properties of Transarterial Oncolytic VSV Therapy for Hepatocellular Carcinoma in Rats With Thioacetamide-Induced Liver Fibrosis.* Mol Ther, 2013.
83. Jenks, N., et al., *Safety studies on intrahepatic or intratumoral injection of oncolytic vesicular stomatitis virus expressing interferon-beta in rodents and nonhuman primates.* Hum Gene Ther, 2010. **21**(4): p. 451-62.
84. Schwaiger, M. and C. Peschel, *Biological imaging for selecting and monitoring cancer therapy; a pathway to individualised therapy.* Eur J Nucl Med Mol Imaging, 2006. **33 Suppl 1**: p. 1-5.
85. Raty, J.K., et al., *Non-invasive Imaging in Gene Therapy.* Mol Ther, 2007. **15**(9): p. 1579-86.
86. Serganova, I., V. Ponomarev, and R. Blasberg, *Human reporter genes: potential use in clinical studies.* Nucl Med Biol, 2007. **34**(7): p. 791-807.
87. Tjuvajev, J.G., et al., *Imaging the expression of transfected genes in vivo.* Cancer Res, 1995. **55**(24): p. 6126-32.
88. Tjuvajev, J.G., et al., *Noninvasive imaging of herpes virus thymidine kinase gene transfer and expression: a potential method for monitoring clinical gene therapy.* Cancer Res, 1996. **56**(18): p. 4087-95.
89. Li, H., et al., *HSV-NIS, an oncolytic herpes simplex virus type 1 encoding human sodium iodide symporter for preclinical prostate cancer radiovirotherapy.* Cancer Gene Ther, 2013. **20**(8): p. 478-85.
90. Goel, A., et al., *Radioiodide imaging and radiovirotherapy of multiple myeloma using VSV(Delta51)-NIS, an attenuated vesicular stomatitis virus encoding the sodium iodide symporter gene.* Blood, 2007. **110**(7): p. 2342-50.
91. Dai, G., O. Levy, and N. Carrasco, *Cloning and characterization of the thyroid iodide transporter.* Nature, 1996. **379**(6564): p. 458-60.
92. Smanik, P.A., et al., *Cloning of the human sodium lodide symporter.* Biochem Biophys Res Commun, 1996. **226**(2): p. 339-45.
93. Hu, S., et al., *Comparison of rNIS and hNIS as reporter genes for noninvasive imaging of bone mesenchymal stem cells transplanted into infarcted rat myocardium.* Mol Imaging, 2011. **10**(4): p. 227-37.

94. Gambhir, S.S., et al., *A mutant herpes simplex virus type 1 thymidine kinase reporter gene shows improved sensitivity for imaging reporter gene expression with positron emission tomography.* Proc Natl Acad Sci U S A, 2000. **97**(6): p. 2785-90.
95. Yaghoubi, S., et al., *Human pharmacokinetic and dosimetry studies of [(18)F]FHBG: a reporter probe for imaging herpes simplex virus type-1 thymidine kinase reporter gene expression.* J Nucl Med, 2001. **42**(8): p. 1225-34.
96. Yaghoubi, S.S., et al., *Preclinical safety evaluation of 18F-FHBG: a PET reporter probe for imaging herpes simplex virus type 1 thymidine kinase (HSV1-tk) or mutant HSV1-sr39tk's expression.* J Nucl Med, 2006. **47**(4): p. 706-15.
97. Penuelas, I., et al., *Positron emission tomography imaging of adenoviral-mediated transgene expression in liver cancer patients.* Gastroenterology, 2005. **128**(7): p. 1787-95.
98. Paneda, A., et al., *Adeno-associated virus liver transduction efficiency measured by in vivo [18F]FHBG positron emission tomography imaging in rodents and nonhuman primates.* Hum Gene Ther, 2011. **22**(8): p. 999-1009.
99. Chierichetti, F. and G. Pizzolato, *18f-Fdg-Pet/Ct.* Q J Nucl Med Mol Imaging, 2012.
100. Sublette, M.E., et al., *Regional brain glucose uptake distinguishes suicide attempters from non-attempters in major depression.* Arch Suicide Res, 2013. **17**(4): p. 434-47.
101. Schwaiger, M., S. Ziegler, and S.G. Nekolla, *PET/CT: challenge for nuclear cardiology.* J Nucl Med, 2005. **46**(10): p. 1664-78.
102. Wieder, H.A., et al., *Comparison of changes in tumor metabolic activity and tumor size during chemotherapy of adenocarcinomas of the esophagogastric junction.* J Nucl Med, 2005. **46**(12): p. 2029-34.
103. Cintolo, J.A., J. Tchou, and D.A. Pryma, *Diagnostic and prognostic application of positron emission tomography in breast imaging: emerging uses and the role of PET in monitoring treatment response.* Breast Cancer Res Treat, 2013. **138**(2): p. 331-46.
104. Krause, B.J., S. Schwarzenbock, and M. Souvatzoglou, *FDG PET and PET/CT.* Recent Results Cancer Res, 2013. **187**: p. 351-69.
105. Caroli, P., et al., *Non-FDG PET in the practice of oncology.* Indian J Cancer, 2010. **47**(2): p. 120-5.
106. Bakheet, S.M. and J. Powe, *Benign causes of 18-FDG uptake on whole body imaging.* Semin Nucl Med, 1998. **28**(4): p. 352-8.
107. Yamada, S., et al., *High accumulation of fluorine-18-fluorodeoxyglucose in turpentine-induced inflammatory tissue.* J Nucl Med, 1995. **36**(7): p. 1301-6.
108. Kubota, R., et al., *Intratumoral distribution of fluorine-18-fluorodeoxyglucose in vivo: high accumulation in macrophages and granulation tissues studied by microautoradiography.* J Nucl Med, 1992. **33**(11): p. 1972-80.
109. Tan, G.J., et al., *FDG PET/CT in the liver: lesions mimicking malignancies.* Abdom Imaging, 2013.
110. Puranik, A.D., et al., *Hepatic metastasis disguised as fat spared area in the background of fatty liver: Detection on FDG PET/CT.* Indian J Nucl Med, 2013. **28**(2): p. 99-101.
111. Gulyas, B. and C. Halldin, *New PET radiopharmaceuticals beyond FDG*

for brain tumor imaging. Q J Nucl Med Mol Imaging, 2012. **56**(2): p. 173-90.
112. Dunet, V., et al., *Performance of 18F-fluoro-ethyl-tyrosine (18F-FET) PET for the differential diagnosis of primary brain tumor: a systematic review and Metaanalysis.* J Nucl Med, 2012. **53**(2): p. 207-14.
113. Rau, F.C., et al., *O-(2-[(18)F]Fluoroethyl)- L-tyrosine (FET): a tracer for differentiation of tumour from inflammation in murine lymph nodes.* Eur J Nucl Med Mol Imaging, 2002. **29**(8): p. 1039-46.
114. Heiss, P., et al., *Investigation of transport mechanism and uptake kinetics of O-(2-[18F]fluoroethyl)-L-tyrosine in vitro and in vivo.* J Nucl Med, 1999. **40**(8): p. 1367-73.
115. Chang, C.H., et al., *Comparative evaluation of FET and FDG for differentiating lung carcinoma from inflammation in mice.* Anticancer Res, 2006. **26**(2A): p. 917-25.
116. Barthel, H., et al., *The uptake of 3'-deoxy-3'-[18F]fluorothymidine into L5178Y tumours in vivo is dependent on thymidine kinase 1 protein levels.* Eur J Nucl Med Mol Imaging, 2005. **32**(3): p. 257-63.
117. Rasey, J.S., et al., *Validation of FLT uptake as a measure of thymidine kinase-1 activity in A549 carcinoma cells.* J Nucl Med, 2002. **43**(9): p. 1210-7.
118. Shields, A.F., et al., *Imaging proliferation in vivo with [F-18]FLT and positron emission tomography.* Nat Med, 1998. **4**(11): p. 1334-6.
119. Buck, A.K., et al., *Imaging proliferation in lung tumors with PET: 18F-FLT versus 18F-FDG.* J Nucl Med, 2003. **44**(9): p. 1426-31.
120. Shen, C., et al., *Triplex-forming oligodeoxynucleotides targeting survivin inhibit proliferation and induce apoptosis of human lung carcinoma cells.* Cancer Gene Ther, 2003. **10**(5): p. 403-10.
121. Kenny, L.M., et al., *Quantification of cellular proliferation in tumor and normal tissues of patients with breast cancer by [18F]fluorothymidine-positron emission tomography imaging: evaluation of analytical methods.* Cancer Res, 2005. **65**(21): p. 10104-12.
122. Pio, B.S., et al., *Usefulness of 3'-[F-18]fluoro-3'-deoxythymidine with positron emission tomography in predicting breast cancer response to therapy.* Mol Imaging Biol, 2006. **8**(1): p. 36-42.
123. Buck, A.K., et al., *Molecular imaging of proliferation in malignant lymphoma.* Cancer Res, 2006. **66**(22): p. 11055-61.
124. Cobben, D.C., et al., *Detection and grading of soft tissue sarcomas of the extremities with (18)F-3'-fluoro-3'-deoxy-L-thymidine.* Clin Cancer Res, 2004. **10**(5): p. 1685-90.
125. Choi, S.J., et al., *[18F]3'-deoxy-3'-fluorothymidine PET for the diagnosis and grading of brain tumors.* Eur J Nucl Med Mol Imaging, 2005. **32**(6): p. 653-9.
126. Eckel, F., et al., *Imaging of proliferation in hepatocellular carcinoma with the in vivo marker 18F-fluorothymidine.* J Nucl Med, 2009. **50**(9): p. 1441-7.
127. Kiessling, F., B.J. Pichler, and SpringerLink (Online service), *Small Animal Imaging Basics and Practical Guide*. 2011, Springer-Verlag Berlin Heidelberg,: Berlin, Heidelberg. p. 1 online resource.
128. Lawson, N.D., et al., *Recombinant vesicular stomatitis viruses from DNA.* Proc Natl Acad Sci U S A, 1995. **92**(10): p. 4477-81.
129. Whelan, S.P., et al., *Efficient recovery of infectious vesicular stomatitis virus entirely from cDNA clones.* Proc Natl Acad Sci U S A, 1995. **92**(18):

p. 8388-92.
130. Schnell, M.J., et al., *Foreign glycoproteins expressed from recombinant vesicular stomatitis viruses are incorporated efficiently into virus particles.* Proc Natl Acad Sci U S A, 1996. **93**(21): p. 11359-65.
131. Schnell, M.J., et al., *The minimal conserved transcription stop-start signal promotes stable expression of a foreign gene in vesicular stomatitis virus.* J Virol, 1996. **70**(4): p. 2318-23.
132. Gonzalez-Hernandez, M.B., J. Bragazzi Cunha, and C.E. Wobus, *Plaque assay for murine norovirus.* J Vis Exp, 2012(66): p. e4297.
133. Boll, H., et al., *Micro-CT based experimental liver imaging using a nanoparticulate contrast agent: a longitudinal study in mice.* PLoS One, 2011. **6**(9): p. e25692.
134. Hamacher, K., H.H. Coenen, and G. Stocklin, *Efficient stereospecific synthesis of no-carrier-added 2-[18F]-fluoro-2-deoxy-D-glucose using aminopolyether supported nucleophilic substitution.* J Nucl Med, 1986. **27**(2): p. 235-8.
135. Wester, H.J., et al., *Synthesis and radiopharmacology of O-(2-[18F]fluoroethyl)-L-tyrosine for tumor imaging.* J Nucl Med, 1999. **40**(1): p. 205-12.
136. Alauddin, M.M. and P.S. Conti, *Synthesis and preliminary evaluation of 9-(4-[18F]-fluoro-3-hydroxymethylbutyl)guanine ([18F]FHBG): a new potential imaging agent for viral infection and gene therapy using PET.* Nucl Med Biol, 1998. **25**(3): p. 175-80.
137. Brader, P., I. Serganova, and R.G. Blasberg, *Noninvasive molecular imaging using reporter genes.* J Nucl Med, 2013. **54**(2): p. 167-72.
138. Ntziachristos, V. and D. Razansky, *Optical and opto-acoustic imaging.* Recent Results Cancer Res, 2013. **187**: p. 133-50.
139. Taruttis, A. and V. Ntziachristos, *Translational optical imaging.* AJR Am J Roentgenol, 2012. **199**(2): p. 263-71.
140. Ma, R., et al., *Fast scanning coaxial optoacoustic microscopy.* Biomed Opt Express, 2012. **3**(7): p. 1724-31.
141. Liu, B., et al., *Sodium iodide symporter is expressed at the preneoplastic stages of liver carcinogenesis and in human cholangiocarcinoma.* Gastroenterology, 2007. **132**(4): p. 1495-503.
142. Klutz, K., et al., *Image-guided tumor-selective radioiodine therapy of liver cancer after systemic nonviral delivery of the sodium iodide symporter gene.* Hum Gene Ther, 2011. **22**(12): p. 1563-74.
143. Klutz, K., et al., *Sodium iodide symporter (NIS)-mediated radionuclide ((131)I, (188)Re) therapy of liver cancer after transcriptionally targeted intratumoral in vivo NIS gene delivery.* Hum Gene Ther, 2011. **22**(11): p. 1403-12.
144. Haddad, D., et al., *A vaccinia virus encoding the human sodium iodide symporter facilitates long-term image monitoring of virotherapy and targeted radiotherapy of pancreatic cancer.* J Nucl Med, 2012. **53**(12): p. 1933-42.
145. Grunwald, G.K., et al., *Systemic image-guided liver cancer radiovirotherapy using dendrimer-coated adenovirus encoding the sodium iodide symporter as theranostic gene.* J Nucl Med, 2013. **54**(8): p. 1450-7.
146. Reddi, H.V., et al., *Preclinical efficacy of the oncolytic measles virus expressing the sodium iodide symporter in iodine non-avid anaplastic thyroid cancer: a novel therapeutic agent allowing noninvasive imaging*

and radioiodine therapy. Cancer Gene Ther, 2012. **19**(9): p. 659-65.
147. Grunwald, G.K., et al., *Sodium iodide symporter (NIS)-mediated radiovirotherapy of hepatocellular cancer using a conditionally replicating adenovirus.* Gene Ther, 2013. **20**(6): p. 625-33.
148. Spitzweg, C. and J.C. Morris, *The sodium iodide symporter: its pathophysiological and therapeutic implications.* Clin Endocrinol (Oxf), 2002. **57**(5): p. 559-74.
149. Suksanpaisan, L., et al., *Oral contrast enhances the resolution of in-life NIS reporter gene imaging.* Cancer Gene Ther, 2013. **20**(11): p. 638-41.
150. Gerolami, R., et al., *Evaluation of HSV-tk gene therapy in a rat model of chemically induced hepatocellular carcinoma by intratumoral and intrahepatic artery routes.* Cancer Res, 2000. **60**(4): p. 993-1001.
151. Sangro, B., et al., *A phase I clinical trial of thymidine kinase-based gene therapy in advanced hepatocellular carcinoma.* Cancer Gene Ther, 2010. **17**(12): p. 837-43.
152. Beger, R.D., *A review of applications of metabolomics in cancer.* Metabolites, 2013. **3**(3): p. 552-74.
153. Jolepalem, P., J.N. Rydberg, and C.O. Wong, *Improvement of hepatic lesion characterization by 18F-FDG PET/CT with the use of the lesion to background liver activity ratio.* Clin Nucl Med, 2013. **38**(11): p. 869-73.
154. Ahn, S.J., et al., *(1)(8)F-FDG PET metabolic parameters and MRI perfusion and diffusion parameters in hepatocellular carcinoma: a preliminary study.* PLoS One, 2013. **8**(8): p. e71571.
155. Huang, W.Y., et al., *18F-FDG PET and combined 18F-FDG-contrast CT parameters as predictors of tumor control for hepatocellular carcinoma after stereotactic ablative radiotherapy.* J Nucl Med, 2013. **54**(10): p. 1710-6.
156. Beiderwellen, K., et al., *Depiction and characterization of liver lesions in whole body [(1)(8)F]-FDG PET/MRI.* Eur J Radiol, 2013. **82**(11): p. e669-75.
157. Glaudemans, A.W., et al., *The use of (18)F-FDG-PET/CT for diagnosis and treatment monitoring of inflammatory and infectious diseases.* Clin Dev Immunol, 2013. **2013**: p. 623036.
158. Lee, T.S., et al., *Comparison of 18F-FDG, 18F-FET and 18F-FLT for differentiation between tumor and inflammation in rats.* Nucl Med Biol, 2009. **36**(6): p. 681-6.
159. Tang, G., et al., *Synthesis and evaluation of O-(3-[18F]fluoropropyl)-L-tyrosine as an oncologic PET tracer.* Nucl Med Biol, 2003. **30**(7): p. 733-9.
160. Cullinane, C., et al., *Differential (18)F-FDG and 3'-deoxy-3'-(18)F-fluorothymidine PET responses to pharmacologic inhibition of the c-MET receptor in preclinical tumor models.* J Nucl Med, 2011. **52**(8): p. 1261-7.
161. Paproski, R.J., et al., *Biodistribution and uptake of 3'-deoxy-3'-fluorothymidine in ENT1-knockout mice and in an ENT1-knockdown tumor model.* J Nucl Med, 2010. **51**(9): p. 1447-55.
162. Cawthorne, C., et al., *[18F]-FLT positron emission tomography can be used to image the response of sensitive tumors to PI3-kinase inhibition with the novel agent GDC-0941.* Mol Cancer Ther, 2013. **12**(5): p. 819-28.
163. Wu, C.Y., et al., *Monitoring tumor response with radiolabeled nucleoside analogs in a hepatoma-bearing mouse model early after doxisome((R)) treatment.* Mol Imaging Biol, 2013. **15**(3): p. 326-35.

164. Bieze, M., et al., *Diagnostic accuracy of 18F-methyl-choline PET/CT for intra- and extrahepatic hepatocellular carcinoma.* Hepatology, 2013.
165. Martinez-Moller, A., et al., *Workflow and scan protocol considerations for integrated whole-body PET/MRI in oncology.* J Nucl Med, 2012. **53**(9): p. 1415-26.
166. Weibel, S., et al., *Imaging of intratumoral inflammation during oncolytic virotherapy of tumors by 19F-magnetic resonance imaging (MRI).* PLoS One, 2013. **8**(2): p. e56317.

8 APPENDIX

8.1 Equipment

Table 10. ***Equipment***

Product	Company
Agarose Gel Mini-Sub Cell GT	Bio-Rad, Germany
Agarose Gel Wide Mini-Sub Cell GT	Bio-Rad, Germany
Automatic Gamma Counter, 1480 Wizard	Wallac, Finland
Autostainer	Dako, Germany
Bacterial Incubator, Heraeus Function Line	Heraeus, Germany
Bacterial Incubator/ShakerKS-15, TH-15	Edmund Bühler GmbH, Germany
Balance	KERN AGB, Germany
Balance	KERN FTB, Germany
Cauter, Deluxe High Temperature Cauter	Bovie, USA
Centrifuge	Kendro, Germany
Centrifuge 5415 R	Eppendorf, Germany
Centrifuge 5702 R	Eppendorf, Germany
Centriuge 5415 D	Eppendorf, Germany
Electrophoresis system Mini PROTEAN	Bio-Rad, Germany
Electrophoresis system Mini PROTEAN Tetra System	Bio-Rad, Germany
Film processor Hyperprocessor	Amersham GE Healthcare, Germany
Freezer -20 °C	Siemens, Germany
Freezer -80 °C, Hera freeze	Heraeus, Germany
Gel Doc XR+	Bio-Rad, Germany

Hamilton Syringe 705 LT 50µL	Hamilton Company, USA
Hypercassette cassette (Western Blot)	Amersham Bioscience, UK
Ice machine	Ziegra, Germany
Image Plate Reader CR35 BIO	Dürr Medical, Germany
Incubator Hera Cell 240	Heraeus, Germany
Laminar flow Hera Safe	Kendro, Germany
Magnet stirrer/hot plate IKA RCT basic	IKA, Germany
Magnetic stirrer	Heidolph, Germany
MicroPET/CT scanner	INVEON Siemens Medical Solutions, USA
Micropipettes	Eppendorf, Germany
Microscope (fluorescence) Zeiss Axiovert HBO 100	Zeiss, Germany
Microscope Optech	Exacta Optech, Germany
Microtiterplate-Photometer Multiskan + Ascent Software	Thermo Scientific, USA
Microwave	Siemens, Germany
Multichannel pipette 300	Eppendorf, Germany
Multipipette plus	Eppendorf, Germany
Neubauer counting chamber	Roth, Germany
Orbital shaker DUOMAX 1030	Heidolph, Germany
PCR cycler peqSTAR	Eppendorf, Germany
pH-meter	WTW, Germany
Phosphoimaging Plate VMIP2430210 24x30	Dürr Medical, Germany
Pipetboy	Eppendorf, Germany
Power Supply Power Pack Basic	Bio-Rad, Germany
Rotator Drive STR4	Stuart, USA
Rotor for Ultracentrifugation, 70Ti	Beckman Coulter, Germany

Spectrophotometer SmartSpec Plus	Bio-Rad, Germany
Thermomixer compact	Eppendorf, Germany
Ultracentrifuge Optima XL-100K	Beckman, USA
Waterbath	GFL, Germany
X-ray cassette 24x30	Rego, Germany

8.2 Consumables

Table 11. *Consumables*

Product	**Company**
Aspirating pipette Bio-One	Greiner, Germany
Cell culture flask with vented screw (75 cm^2)	TPP, Switzerland
Cell culture plates (6-, 12-, 24-, 48- and 96-well)	TPP, Switzerland
CL-XPosure Film	Thermo Fisher Scientific, USA
Combitips advanced (1 mL, 5 mL, 10 mL)	Eppendorf, Germany
Conical Tubes (15 ml and 50 ml)	BD Falcon, USA
Cryotubes 1 ml	Corning, USA
Culture Slides, 8 chamber polystyrene	BD Falcon, USA
Filter tips, TipOne	StarLab, Germany
Mini-Trans Blot Filter	Bio-Rad, Germany
Needles (20 G, 27 G and 30G)	Braun, Germany
Nitrocellulose membrane, 0.45 µm	Bio-Rad, Germany
Parafilm	Roth, Germany
Petri dish (100 mm x15 mm)	BD Falcon, USA
Safe lock microcentrifuge tubes (1.5 mL)	Eppendorf, Germany
Safe lock microcentrifuge tubes (2 mL)	Sarstedt, Germany
Serological pipettes (5 mL, 10 mL, 25 mL and 50 mL)	BD Falcon, USA

Suture Ethicon Coated Vicryl 4-0	Johnson & Johnson, Belgium
Suture Ethicon Prolene 7-0	Johnson & Johnson, Belgium
Syringe filter (0.22 µm)	TPP, Switzerland
Syringe Luer-Lok sterile (5 m L, 10 mL)	BD Falcon, USA
Syringe sterile (1 mL, 20 mL)	BD Falcon, USA

8.3 Chemicals, solutions, buffers

Table 12. ***Chemicals, solutions, buffers***

Product	**Company**
30% Acrylamide/Bis Solution 37.5:1	Bio-Rad, Germany
50x TAE	Bio-Rad, Germany
Agarose	Biozym, Germany
Ammonium persulphate (APS)	Bio-Rad, Germany
Ampicillin	Roth, Germany
β-Mercaptoethanol	Bio-Rad, Germany
Blotting Grade Blocker	Bio-Rad, Germany
Bromophenol blue	Sigma-Aldrich, Germany
Complete Protease Inhibitor Mix	Roche, Germany
Crystal violet	Sigma Aldrich, Germany
D-MEM	ATCC, USA
Dimethyl sulfoxide (DMSO)	Sigma Aldrich, Germany
Disodium phosphate	Fluka (Seelze, Germany)
DNA Ladder (100 bp and 1 Kb)	NEB, Germany
Ethanol absolute (EtOH)	Roth, Germany
Ethidiumbromide (500 µg/mL)	Sigma-Aldrich, Germany
Fetal Calf Serum (FCS)	Biochrom, Germany

Formaldehyde (37 %)	Roth, Germany
G-MEM	Invitrogen, Germany
Geneticin G418 solution, steril	Calbiochem, USA
Hoechst 3342	Thermo Fisher Scientific, USA
Isofluran (Forene 100 % (v/v))	Abbott, Germany
L-Glutamine (200 mM)	PAA, Austria
L-T4 Henning	Sanofi-Aventis, Germany
Laemmli sample buffer, 2x	Bio-Rad, Germany
LB Agar	Sigma Aldrich, Germany
LB Broth	Sigma Aldrich, Germany
Lipofectamine2000	Invitrogen, Germany
Methanol	Roth, Germany
normal horse serum (2.5%)	Vector, USA
Nucleic acid sample buffer, 5x	Bio-Rad, Germany
Opti-MEM I reduced serum medium	Invitrogen, Germany
Opti-PRO SFM	Invitrogen, Germany
Paraformaldehyde	Sigma Aldrich, Germany
PBS solution, sterile for cell culture appl. 1x (w/o Ca and Mg)	PAA, Austria
PBS solution, sterile for cell culture appl. 1x (with Ca and Mg)	PAA, Austria
Penicillin/Streptomycin (100 x)	PAA, Austria
Phosphatase inhibitor	
Phosphatase Inhibitor Cocktail 2	Sigma Aldrich, Germany
Precision Plus Protein Dual Color Standards	Bio-Rad, Germany
Resolving Gel Buffer pH 8.8	Bio-Rad, Germany
Restore PLUS Western Blot Stripping buffer	Thermo Scientific, USA

Roti-Mount FluorCare	Roth, Germany
SDS 10% (w/v)	Bio-Rad, Germany
Sodium chloride	Roth, Germany
Stacking Gel Buffer pH 6.8	Bio-Rad, Germany
Sucrose	Sigma Aldrich, Germany
TEMED	Bio-Rad, Germany
Trypan Blue Solution	Sigma Aldrich, Germany
Trypsin/EDTA solution (1 x)	PAA, Austria
Tryptose phosphate broth solution	Invitrogen, Germany
Tween-20	Applichem, Germany
Western Blot running buffer, 10x TGS	Bio-Rad, Germany
Western Blot transfer buffer, 10x TG	Bio-Rad, Germany

8.4 Kits and enzymes

Table 13. ***Kits and enzymes***

Product	**Company**
CellTiter96 AQ_{ueous} One Solution Cell Proliferation Assay	Promega, USA
QIAprep Spin Miniprep Kit	Qiagen, Germany
QIAGEN Plasmid Midi Kit	Qiagen, Germany
QIAquick PCR purification Kit	Qiagen, Germany
QIAquick Gel Extraction Kit	Qiagen, Germany
PrimeSTAR GXL DNA Polymerase	Takara, Clontech, USA
Quick Ligation Kit	NEB, Germany
ECL Prime Western Blotting Reagent	GE Amersham
Pierce BCA Protein Assay Kit	Thermo Fisher Scientific, USA
XhoI	NEB, Germany
NheI	NEB, Germany
HindIII	NEB, Germany

8.5 Radiotracers

Table 14. ***Radiotracers***

^{124}I sodium iodide solution	Eckert und Ziegler Radiopharma GmbH, Germany
^{125}I in 40 mM NaOH	Hartman Analytica GmbH, Germany
^{18}F-FDG	kindly provided by Nuklearmedizinische Klinik, Klinikum rechts der Isar TU München, Germany
^{18}F-FET	kindly provided by Nuklearmedizinische Klinik, Klinikum rechts der Isar TU München, Germany
^{18}F-FHBG	kindly provided by Nuklearmedizinische Klinik, Klinikum rechts der Isar TU München, Germany
^{18}F-FLT	kindly provided by Nuklearmedizinische Klinik, Klinikum rechts der Isar TU München, Germany

8.6 Software

Table 15. ***Software***

Software	**Company**
Adobe Illustrator CS5	Adobe Systems Inc.
Adobe Photoshop CS5	Adobe Systems Inc.
AIDA image analyser	Raytest, Germany
Endnote X5	Thomson Reuters
INVEON Reasearch Workplace	Inveon Siemens, USA
MacVector 12.6	MacVector Inc., USA
Microsoft Office 2011	Microsoft, USA
Prism 5	GraphPad Software, USA

ACKNOWLEDGEMENT

First of all I would like to thank Dr. Oliver Ebert for giving me the opportunity to carry out my PhD thesis in his laboratory. I am thankful for his trust in me and for giving me a lot of freedom. I appreciate a lot, that I was welcomed even under all the crazy circumstance in the beginning. Thank you!

I want to thank Prof. Dr. Sibylle Ziegler and Dr. Per Sonne Holm for being on my thesis committee and for their support and input throughout the entire project.

Many thanks go to Dr. Katrin Offe and her team of the PhD program for great support, organization and constant accessibility for any kind of question.

Sabzarab for her great support and her connection to the moon. Babs for introducing me to the lab secrets, when I was new and scared to death. Life-time-lasting thankfulness goes to Iron Doc for her easy-PhD-support with the layout and formatting.

Thank you to Dr. Iina Laitinen for the help and inspiration with small animal imaging and its analysis and interpretation.

I want to thank Sybille Reder, Markus Mittelhäuser, Marco Lehmann for performing the PET/CT scans, Michael Herz for the tracer production, Katja Steiger and Irene Esposito for the help with the histology.

Muchas gracias a mi alma gemela por su gran apoyo incondicional incluso por le gran distancia que nos separa- pero que no lo hizo en realidad.

A very big thank you goes to all my family and friends. Especially those special ones, who make the top three of both groups: Palemsi, Marv & Tinsi.

Last I want to thank Jennifer. Without your constant support, your knowledge, your wisdom lectures, whenever I suffered a nervous breakdown, your jokes, your sarcasm and your almost VSV-like-infective enthusiasm, this wouldn't have happened. Thank you soooooooo much. And more. ….anyhow, I'd still be in with the bus idea!

ömbröforlife

Griesgram soll der Teufel holen. Mag

es biegen, mag es krachen- immer

lächeln, immer lachen